To the Graduate Council:

I am submitting herewith a thesis written by Seong-Soo Park entitled "Characterization of Zirconia - Alumina Composites Sintered Using 2.45 GHz Radiation." I have examined the final copy of this thesis for form and content and recommend that it be accepted in partial fulfillment of the requirements for the degree of Master of Science, with a major in Metallurgical Engineering.

Thomas T. Meek

T. T. Meek, Major Professor

We have read this thesis
and recommend its acceptance:

R. A. Buchanan

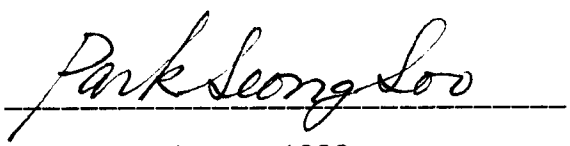
Accepted for the Council:

Vice Provost
and Dean of The Graduate School

STATEMENT OF PERMISSION TO USE

In presenting this thesis in partial fulfillment of the requirements for a Master's degree at The University of Tennessee, Knoxville, I agree that the Library shall make it available to borrowers under rules of the Library. Brief quotations from this thesis are allowable without special permission, provided that accurate acknowledgement of the source is made.

Permission for extensive quotation from or reproduction of this thesis may be granted by my major professor, or in his absence, by the Head of Interlibrary Services when, in the opinion of either, the proposed use of the material is for scholarly purposes. Any copying or use of the material in this thesis for financial gain shall not be allowed without my written permission.

Signature 

Date August 1989

CHARACTERIZATION OF ZIRCONIA - ALUMINA COMPOSITES SINTERED USING 2.45 GHz RADIATION

A Thesis

Presented for the

Master of Science

Degree

The University of Tennessee, Knoxville

Seong Soo Park

August 1989

DEDICATION

This thesis is dedicated to my wife and son, and especially my parents.

ACKNOWLEDGEMENTS

The author would like to express his deep gratitude to his major professor, Dr. Thomas T. Meek, who guided him with patience and wisdom. Appreciation is also expressed to Dr. R. A. Buchanan and Dr. A. J. Pedraza for their advice and guidance.

The author is grateful to the departmental mechanical and electronic shops for maintaining the microwave processing lab equipment, to Mr. B. L. McGill for his help in scanning electron microscopy and to Mr. A. W. J. Carter and Mrs. A. Cagle for procuring and distributing many of the materials essential to this research.

The author would like to thank his fellow graduate students for their help and support.

The author is deeply indebted to the Du Pont Corporation for providing financial assistance through the Du Pont Graduate Study Fellowship Program.

Finally, the author would like to thank his wife, Bong-Eun Kim, and his son, Min-Shik Park, without whose patience, sacrifices and support this research would not have become a reality.

ABSTRACT

The composite material 80 wt% ZrO_2 (+3 mol% Y_2O_3) 20 wt% Al_2O_3 was sintered in a Cober S6F microwave oven. Power was supplied to the multi-mode resonant cavity through a WR-284 waveguide by a 6 KW variable power microwave generator operating at 2.45 GHz microwave radiation.

The microwave heating process has shown potential for uniform material heating on a macroscopic scale, and internal and volumetric heating, and selective heating on the both a macroscopic and microscopic scale with rapid heating rates possible. This work showed how a zirconia-alumina composite interacts with microwave radiation and how the loss characteristics of this material vary as a function of temperature.

The microwave heating of the zirconia-alumina composite samples was done in two groups; one was heated with no susceptor and the other was heated with a susceptor to allow enhanced coupling. The relative occurrence in time of various power levels and the sample surface temperature were used to control the sample sintering. For all work the system was operated in the manual mode. The microwave heating was described as a three-step process, namely 1) preheating, 2) transition, and 3) stable sintering. Experimental results on optimum heating conditions, temperature profile, and transient heating characteristics of materials were presented and explained.

Microwave processed materials were densified much more

rapidly and at much shorter time and at higher heating rates than the conventionally processed materials. A comparison between microwave processed and conventionally processed materials revealed no difference in measured thermal-shock resistance. This was probably due to how the samples were prepared and further work will need to be done in this area before a final opinion can be given. However, a comparison in phase analysis of zirconia and microstructure revealed a significant difference.

Unusual microstructure of microwave processed materials was explained by microwave heating theory in an earlier paper by Meek. Also, smaller grain size of the microwave processed materials was explained by Brook's theory.

TABLE OF CONTENTS

CHAPTER PAGE

I. INTRODUCTION 1

II. LITERATURE REVIEW 11

II-1. Microwave-Material Interactions and Loss Mechanism 11
- II-1-a. Microwave-material interactions
- II-1-b. Loss mechanism

II-2. Microwave Heating Theory 24
- II-2-a. Electric field intensity
- II-2-b. Power density
- II-2-c. Half-power penetration depth
- II-2-d. Heating rate

II-3. Parameters Affecting the Dielectric Constant 29

II-4. Characteristics of Applicators 32
- II-4-a. Multi-mode applicator
- II-4-b. Single-mode applicator
- II-4-c. Resonant applicator

II-5. The Equivalent Exciting Field and Heat Generated . . 33

II-6. Thermal Stability and Temperature Control 35
- II-6-a. Thermal instability
- II-6-b. Stable temperature
- II-6-c. Temperature profile control

II-7. Thermal Stresses in Ceramics 41
- II-7-a. Fundamental considerations and theory
- II-7-b. Initiation of thermal-shock failure
- II-7-c. Crack propagation in thermal-shock failure
- II-7-d. Two general approaches to the thermal -shock resistance of ceramics

II-8. Study for Zirconia-Alumina Composite 52
- II-8-a. The crystal structure of zirconia
- II-8-b. Phase transformation of zirconia
- II-8-c. Transformation toughening of zirconia

CHAPTER **PAGE**

II-8-d. Improvement of the properties of a zirconia-alumina composite

III. EXPERIMENTAL METHODS 69

III-1. Material 69

III-2. Conventional and Microwave Sintering 69

III-3. Components of the Experimental System 72
III-3-a. Microwave generator
III-3-b. Circulator
III-3-c. Waveguide
III-3-d. Applicator
III-3-e. Pyrometer

III-4. Measurement of Density and Porosity 80

III-5. Thermal-Shock Test 80

III-6. Microstructure Analysis 81

III-7. XRD Techniques 82

III-8. Compression Test 85

IV. RESULTS AND DISCUSSION 86

IV-1. The Effect of Microwave Power 86

IV-2. Microwave Sintering 91

IV-3. Densification Behavior in Microwave Field 115

IV-4. Phase Analysis 123

IV-5. Thermal-Shock Property 128

IV-6. Microstructure Analysis 135

V. CONCLUSIONS 163

LIST OF REFERENCES 167

VITA 181

LIST OF TABLES

TABLE		PAGE
1.	Chemical composition and characteristics of Super Z (3Y20A)	70
2.	The desired conditions for an X-ray scan	84
3.	Effect of microwave input power on the heating rates of material	87
4.	Data on microwave sintering of zirconia-alumina composites derived from 30 runs	94
5.	Density of microwave sintered samples	116
6.	Density of conventionally sintered samples	117
7.	Physical characterization of microwave sintered and conventionally sintered samples	120
8.	Thermal-shock strength of the conventionally and microwave sintered samples	129

LIST OF FIGURES

FIGURE		PAGE
1.	Heating patterns in conventional and microwave processes	13
2.	Interaction of microwaves with materials	14
3.	Relative dielectric constant (8 to 10 GHz) versus temperature	18
4.	Loss tangent (8 to 10 GHz) versus temperature	19
5.	Mechanisms of polarization	22
6.	The refraction of **D** at a dielectric interface. For the case shown, $k_1>k_2$. $\mathbf{E}_1$ and $\mathbf{E}_2$ are directed along $\mathbf{D}_1$ and $\mathbf{D}_2$. $\mathbf{D}_1>\mathbf{D}_2$, and $\mathbf{E}_1<\mathbf{E}_2$	26
7.	Temperature and stress distributions for plate that is (a) cooled from the surface and (b) heated from the surface	43
8.	Minimum thermal strain required to initiate crack propagation as a function of crack length and crack density N. (Poisson's ratio = 0.25)	47
9.	Crack length and strength as a function of thermal history	49
10.	Zirconia particle contained within ceramic matrix, before (t) and after (m) the tetragonal-monoclinic phase transformation and associated thermal expansion behavior of the composite	55
11.	(1) Representation of a process zone around a crack tip in a material containing metastable tetragonal zirconia. (2) Representation of crack particle interactions (a), (b), (C), together with (d) the development of compressive surface layer by transformation of the metastable t-zirconia particles to monoclinic via a martensitic shear process	57
12.	Densification during hot pressing (1350 °C; 20 MPa) of the individual powders	61
13.	Densification behavior of mixtures of the two powders during hot pressing (1350 °C; 20 MPa)	62

FIGURE PAGE

14. Scanning electron micrographs of the individual (a) ZrO_2 and (b) Al_2O_3 materials following hot pressing 63

15. Scanning electron micrographs of polished and thermally etched $ZYXXAl_2O_3$ - 1500 °C composite (a) $ZY5Al_2O_3$, (b) $ZY10Al_2O_3$, (c) $ZY20Al_2O_3$, (d) $ZY30Al_2O_3$. In (c) and (d), a crack emanating from a Vickers intent can be seen . . . 66

16. Changing in fractured surface monoclinic percentage with alumina content in the materials; (a) sintered and (b) HIPed 67

17. Photographs of fracture surface of (Y) TZP- binary ceramics: (A) 20 wt% , (B) 40 wt% , (C) 60 wt% ; white grains are zirconia and gray ones alumina 68

18. The experimental system 74

19. Schematic diagram of cavity configuration required for microwave heating of low-loss loads to very high-temp., e.g., zirconia-alumina composite to 1400 °C or 1800 °C . . 77

20. Temperature profile of microwave sintered samples on the susceptor at various applied power with no adjustment of the single-stub tuner 88

21. Temperature profile of microwave sintered samples on the susceptor at various applied power with adjustment of the single-stub tuner 89

22. Net power profile at various constant applied power with adjustment of the single-stub tuner. (net power = applied power - reflected power) 92

23. Net power profile at various constant applied power with no adjustment of the single-stub tuner. (net power = applied power - reflected power) 93

24. Temperature profile of microwave sintered sample without susceptor 99

25. Power distribution in run 12 microwave sintering without susceptor 100

FIGURE PAGE

26. Power distribution in run 16 microwave sintering without susceptor 101

27. Power distribution in run 18 microwave sintering without susceptor 102

28. Power distribution in run 20 microwave sintering without susceptor 103

29. Temperature profile of microwave sintered sample with susceptor 105

30. Power distribution in run 24 microwave sintering with susceptor 106

31. Power distribution in run 25 microwave sintering with susceptor 107

32. Power distribution in run 26 microwave sintering with susceptor 108

33. Power distribution in run 27 microwave sintering with susceptor 109

34. The measured temperature profile of the sample by using IR meter and thermocouple 114

35. Densification rates for microwave sintered samples and conventionally sintered samples at a comparable temperature 118

36. The expected activation entalphy for microwave sintering . 122

37. X-ray diffraction patterns of the conventionally sintered zirconia-alumina composte 124

38. X-ray diffraction patterns of the microwave sintered zirconia-alumina composite 125

39. The comparison of the X-ray diffraction patterns in the microwave sintered and the conventionally sintered sample 126

FIGURE PAGE

40. The compressive strength of microwave and conventionally sintered samples after thermal shock at various temperature 130

41. Optical micrographs of the conventionally sintered composite after (a) thermal shock 1 time at 900 °C and (b) thermal shock 5 times at 800 °C 132

42. Optical micrographs of the microwave sintered composite after (a) thermal shock 1 time at 900 °C and (b) thermal shock 5 times at 800 °C 133

43. Polished surface of a zirconia-alumina composite; (a) conventionally sintered to 1350 °C in 108 hours and (b) microwave sintered to 1400 °C in 30 minutes 136

44. Scanning electron micrographs of polished and thermally etched surface of a zirconia-alumina composite at 1050 °C for 5 hours; (a) conventionally sintered to 1350 °C in 108 hours and (b) microwave sintered to 1400 °C in 30 minutes 137

45. Scanning electron micrographs of polished and thermally etched surface of conventionally sintered samples at 1050 °C for 8 hours; (a) densification is 81.42% (x2,000), (b) densification is 84.44% (x2,000), (c) densification is 81.87% (x5,000), and (d) densification is 81.87% (x10,000) 138

46. Scanning electron micrographs of polished and thermally etched surface of microwave sintered samples at 1050 °C for 8 hours; (a) densification is 99% (x2,000), (b) densification is 99% (x5,000), and (c) densification is 99% (x10,000) 140

47. EDXA shows (a) large grains are zirconia and (b) small grains are zirconia and alumina 142

48. Scanning electron micrograph of polished and thermally etched surface of microwave sintered sample at 1050 °C for 5 hours 143

FIGURE PAGE

49. Scanning electron micrographs of fracture surface of microwave sintered sample; (a) x5,000 and (b) x10,000 144

50. Scanning electron micrographs of fracture surface of conventionally sintered sample at 1350 °C for 108 hours; (a) x2,000 and (b) x10,000 147

51. Scanning electron micrograph of fracture surface of microwave sintered sasmple at 1400 °C for 30 minutes . 148

52. Scanning electron micrographs of fracture surface of microwave sintered sample at area 1; (a) x5,000 and (b) x5,000 149

53. Scanning electron micrographs of fracture surface of microwave sintered sample at area 2; (a) x2,000 and (b) x5,000 150

54. Scanning electron micrographs of fracture surface of microwave sintered sample at area 3; (a) x2,000 and (b) x5,000 151

55. Scanning electron micrographs of fracture surface of microwave sintered sample at area 4; x10,000 152

56. Scanning electron micrographs of fracture surface of microwave sintered sample at area 5; (a) x1,000, (b) x5,000, (c) x5,000, and (d) x1,000 153

57. Scanning electron micrographs of fracture surface of microwave sintered sample; (a) at 1800 °C for 45 minutes and (b) at 1400 °C for 30 minutes 157

58. Scanning electron micrographs of fracture surface of microwave sintered sample; (a) x2,000 and (b) x5,000 . 159

59. Scanning electron micrographs of fracture surface of microwave sintered sample; (a) x2,000 and (b) x8,500 . 160

60. EDXA shows (a) grains are zirconia and (b) wetted regions are alumina 162

CHAPTER I

INTRODUCTION

Thermal processing using microwave radiation has shown the potential for uniform sample heating on a macroscopic scale, and internal and volumetric heating, and selective heating on both a macroscopic and microscopic scale with rapid heating rates possible. The economics of microwave heating appear to be favorable in many cases when compared to conventional thermal processing. This is because the photon flux is instantaneously uniform on a macroscopic level throughout the sample being exposed to the electromagnetic field. For conventional thermal processing, higher energy photons must be converted to phonons at the sample surface and then diffused through the bulk.

Microwave processing of ceramic materials has been investigated over the last 30 years by various researchers. In the late 1940's, Von Hippel (1) began investigating how oxide materials interact with microwave radiation and how the loss characteristics of these materials vary as a function of microwave frequency. Much of his theory and some data on microwave material interactions provided a valuable background for microwave heating.

Feiker's research (2) showed that dielectric materials could not be heated well at the lower frequency because of arcing, but were heated easily at 915 MHz.

Ford (3) reported the heating of metallic oxide and sulfide powders by 2.45 GHz radiation. In his experiment, a different

heating rate for different oxide materials was observed and a number of oxides demonstrated a cut-off temperature which remained constant even after a further increase of microwave power. Wong (4) observed that the temperature "cut-off" effect of metal oxides at 2.45 GHz radiation was thought to be caused by an increase of electrical conductivity of the sample causing most of the microwave energy impinging on the material to be reflected.

Maguire (5) showed that the magnetic and dielectric loss parameters determined the heating characteristics of ferrites at 2.45 GHz radiation. A property of ferrites which make them attractive as a potential temperature control element in microwave heating applications is that at their Curie temperature, they lose their magnetic moment. If its dielectric loss is low, the ferrite no longer absorbs microwaves and stops heating. Therefore, a material containing a low dielectric loss ferrite heats to some limiting temperature determined by the Curie temperature of the ferrite and the rate of heat loss to the surroundings. Krage (6) indicated that in addition to dielectric losses, magnetic losses were also operative at temperatures below the Curie temperature in barium titanate ferrite magnets.

In the mid 1960's, Tinga (7-10) and co-workers (11) studied the thermal processing of oxide and composite materials using 915 MHz and 2.45 GHz electromagnetic radiation. They investigated how certain oxides heat in a microwave field and developed reaction cavities that caused materials to be uniformly heated in such an environment. Although considerable interest was directed toward

ceramics (drying, calcining, sintering, etc.) through the 1970's, several other applications, such as accelerated slip casting and acid digestion of ceramics and minerals, were developed.

Schurbring (12) demonstrated that an alumina spark plug could be made by thermally processing at 2.45 GHz radiation. He showed that a sintering temperature of 1600 °C could be achieved in a multimode cavity, and by controlling the power input, thermal runaway was prevented. The microwave energy required per spark plug for the complete firing cycle was about 50% of the energy required in the standard manufacturing process.

Haas (13) demonstrated that uranium oxide coupled very well with microwave radiation so that uranium oxide could be heated to their melting points in a conventional 600 W table-top microwave oven. Roy (14) found that silica gels could also be melted in the same type oven. Komarneni (15) noted that zeolites absorbed microwave energy quite efficiently, which was believed due to a loss mechanism caused by ionic rattling in a rigid molecular cage.

Holcombe (16,17) screened several different materials for coupling with microwave energy using a 1.6 KW, 2.45 GHz system. Those which showed minimal or no heating with the microwave radiation included yttria, alumina, silica, boron nitrite, graphite, and unstabilized zirconia. Thus, he illustrated the significant microwave coupling ability or heat-ability of boron carbide, and then used boron carbide as a new microwave coupler.

During the past six years, Meek (18-26) and co-workers (27) showed significant differences between conventional thermal

processing and microwave processing of ceramics, glasses, and composite materials. They were the first to propose going to frequencies higher than 2.45 GHz (28) and demonstrated the 60 GHz sintering of alumina. They have observed what appears to be enhanced material transport, rapid sintering, and different microstructures for various multi-component oxide, composite, and glassy materials heated at 2.45 GHz, and 60 GHz. To sinter the low loss ceramics at 2.45 GHz, they suggested the use of various materials to act as both a microwave susceptor material and a second or primary phase material which would act as a crack inhibitor upon sintering. These coupling materials included silicon carbide, silicon nitride, zirconia, glass, glycerol, sodium nitrate, and zirconium nitrate. These materials and other like them initially absorb the 2.45 GHz photons converting them to heat through a photon-phonon conversion process and then after the ceramic or composite reaches a temperature high enough that its electrical loss causes it to continue heating, the susceptor material becomes a second phase that improves the material's overall mechanical properties. Meek (22) has proposed a heating model for a dielectric heated in an electromagnetic field. It describes how the electromagnetic field behaves at an interface between two dielectric media. A cold pressed green ceramic body will begin to heat uniformly if the initial porosity is distributed uniformly throughout, since it appears that the electric fields and power density are greatly intensified in the porous regions between the grains. When dense regions begin to form, the microwave field will begin to decouple from these regions

and then couple more strongly to the regions of low density and low dielectric loss. The net effect is a uniformly densified material.

Kimrey (29-30) and Swain (31) used a 28 GHz, 200 KW CW gyrotron for sintering and annealing of structural and electronic ceramics. They realized that because the microwave absorption coefficient in many ceramics increased exponentially with temperature, rapid heating could result in local thermal runaway, melting, or cracking. They sintered successfully ceramics in a uniform microwave field without dead spots by raising the frequency in the large volume oven from the 2.45 GHz to 28 GHz and changing the ratio of wavelength of the microwaves to the size of a 0.56 m^3 cavity from 1:3 to 1:100. Therefore, Janney and Kimrey (32,33) sintered compacts of alumina doped with 0.1% MgO under vacuum using 28 GHz radiation. Alumina, which is difficult to heat at 2.45 GHz, could be easily heated at 28 GHz. They suggested that approximately 10 times more power could be dissipated in high purity alumina by processing at 28 GHz instead of 2.45 GHz. They also calculated the apparent activation energy for sintering alumina by the two processes. They showed that the activation energy for microwave sintering was about one-third that of conventional sintering. This is dependent on their ability to measure the intergranular temperature in an electromagnetic field. Since their temperature measurements are based on the use of a thermocouple, it remains to be seen whether such a change in activation energy has taken place or not. Many researchers believe that a thermocouple will not give accurate enough temperatures in an electromagnetic

field. One also must be concerned with the way in which the thermocouple perturbs the electromagnetic field.

Following the work of Meek et al (24), Katz (34,35) sintered composites of alumina-10 vol% silicon carbide whiskers by using 2.45 and 60 GHz and boron carbide by using 2.45 GHz microwave radiation. He showed that both 2.45 and 60 GHz microwave processing yielded similar densities at similar sintering temperatures for alumina-10 vol% silicon carbide. He also showed that boron carbide could be sintered without the benefit of sintering aids to a theoretical density of 95% in less than 12 minutes by 2.45 GHz radiation to 2000 °C.

Tian (36,37) investigated the sintering of Al_2O_3-30 wt% TiC composite under high nitrogen pressure in a microwave field. A final density of 95% TD has been achieved at 1950 °C. High gas pressure could suppress the breakdown of gas and thus raise the sintering temperature. He also investigated that the ultra-fine microstructures of alumina with grain size less than 1 μm and densities greater than 99% have been produced by sintering alumina powder in a single-mode cavity. He concluded that high density and ultra-fine grain size alumina could be achieved by the early activation of grain boundary and lattice diffusion before surface diffusion could significantly coarsen the microstructure and reduce the driving force for sintering.

Sutton (38) investigated the potential for the microwave processing of high alumina castables on the removal of the physical water from cast shapes. The result of his investigation showed that

both the high alumina castable material and water interact with 2.45 GHz microwave energy so that both the drying and firing operations could be performed in one microwave processor.

Ahmad (39) applied microwave energy to calcine, sinter, and anneal $YBa_2Cu_3O_{7-x}$ superconducting ceramic. He showed that the microwave processed material exhibited a more refined microstructure, lower porosity, improved oxygen content, and higher superconductivity transition temperature (93 K versus 90 K) over conventionally processed material.

Harrison (40) demonstrated the feasibility of using microwave energy for all of the thermal treatment steps (drying, calcining, binder burn-off, and sintering) necessary to prerare high density PZT and PLZT. He estimated that microwave sintering would use only 5% of the energy used by conventional processes.

Several researchers (41,42) following the work of Meek and Blake (19) have demonstrated that high quality joints can be produced in alumina, mullite, and silicon nitride by microwave heating the ends of two rods butted together. A specially designed single-mode cavity was used to maximize the electric field and maximize heating in the area to be jointed.

Tinga (43) and Varadan (44) have recently reviewed the fundamentals of the microwave sintering process. Tinga proposed some simplified models that could give the process designer insight into the response of materials to microwave energy during sintering. Varadan discussed how a rigorous application of the multiple scattering theory could lead to a better understanding of the

microwave sintering process.

Microwave processing is generally characterized by uniform heating on a macroscopic scale and rapid heating rates, as compared to conventional thermal processing. Brook and co-workers (45-47) proposed that fine grain size at high density could be achieved by raising the ratio of the densification rate to the grain growth rate. Fast firing was demonstrated in experiments to be an effective way for achieving this in Al_2O_3 and $BaTiO_3$ by fast zone sintering at 1850 °C for several minutes. They showed that rapid sintering led to improved ceramic microstructures and high density with the development of finer and more uniform grain structures. The applicability of high heating rates in conventional sintering is limited because of heat transfer and thermal shock limitations. However, it is quite possible that microwave processed ceramics will exhibit similar improved microstructures due to rapid heating rates since the heat is generated within the material. Also, since the sintering time can be lowered in microwave processing, the possibility for exaggerated grain growth may be reduced.

Microwave processing has demonstrated the ability to sinter large and complex shaped ceramic components because heating occurs within the material volume by the microwave energy causing the molecules throughout the volume to vibrate. As a result of this internal and volumetric heating, thermal stresses may be significantly reduced due to a reduced intergranular temperature gradient from the one seen in materials processed by conventional heating. Thus, microwave processing makes it possible to efficiently

remove volatile constituents from thick sections and to reduce cracking during the processing of large and irregular shaped ceramics, which would normally occur in conventional processing.

Microwave processing has the potential for selective heating of microstructural constituents and phases. This occurs due to different microwave absorption characteristics in the different phases. This has important implications for the microwave processing of ceramic composites with improved properties.

Finally, microwave processing has great potential for saving energy when compared with conventional heating (48-50). Since the energy couples directly to the ceramics to be heated, the ceramics may be brought to high temperature in relatively cool surroundings. Due to its selectivity, microwave processing may require significantly lower power consumption.

The following is a outline of present work which demonstrates that ceramic materials may be fabricated using 2.45 GHz microwave radiation. They may be produced in less time utilizing less energy due to the rapid and uniform heating of the materials by the microwave energy.

The material system disscussed in this study is 80 wt% ZrO_2 (+3 mol% Y_2O_3) 20 wt% Al_2O_3 composite. Experimental data are obtained from sintering samples of simple geometry at 2.45 GHz in a 6KW Cober S6F microwave facility. This paper discusses the effect of microwave power level on the heating rates of this material, and the feasibility of using microwave energy to process this material. Also it discusses microstructure, phase analysis, mechanical and thermal

properties, and other data such as sintering data which has been obtained on samples of this material heated using 2.45 GHz electromagnetic radiation.

CHAPTER II

LITERATURE REVIEW

II-1. Microwave-Material Interactions and Loss Mechanism

Microwave processing has been shown to be suitable technique to heat ceramic materials. The electromagnetic radiation used can vary in frequency from 1-140 GHz at least. In order for the absorption of microwave energy which makes microwave heating possible, the ceramic material of interest must exhibit dielectric loss mechanisms at the microwave frequency. The commercial microwave frequency of 2.45 GHz is of interest for dielectric heating studies because of the ready availability and low cost of facilities which operates at this frequency.

Direct production of thermal energy inside the material can be achieved either by electrical current induction at high frequencies for conducting materials or via dielectric or magnetic energy absorption for non-conducting materials. In electrical current heating, it is assumed that the material being heated is placed between the parallel plates to which an alternating field of high frequency is applied. At microwave frequencies, the material being heated in placed inside a microwave cavity which creates the same effect as parallel plates with the electric field between them.

In order to better understand the heating of any specific material by microwave energy, it is necessary to discuss some general concepts of materials and their interaction with microwave

energy. Also, knowledge of loss mechanisms is useful to understanding interaction between the electric field and dielectric ceramics for microwave heating. However, loss mechanisms in ceramics at microwave frequency are presently poorly understood near room temperature and elevated temperature. Work by Ho (51) is probably the best done in the area of understanding loss mechanisms at 28 GHz and above.

II-1-a. Microwave-Material Interactions

The microwave process is fundamentally different from the conventional heating process. In microwave heating, heat is generated internally within the material instead of originating from external heating sources as shown in Figure 1.

The microwaves are reasonably coherent and polarized. They also obey the laws of optics and can be transmitted, absorbed, or reflected, depending on the material types as shown in Figure 2. Metals are opaque to microwaves and thus are good reflectors. Water in its liquid form (low dielectric constant) absorbs microwaves quite well, but when water is in the form of ice (high dielectric constant), microwave energy quite readily is trasmitted through with little absorption.

Many ceramics (e.g., Al_2O_3, MgO, SiO_2, and most glasses) are transparent to 2.45 GHz microwaves at ambient temperature. Other ceramic materials (e.g., Co_2O_3, MnO_2, NiO, and CuO) absorb 2.45 GHz microwave energy efficiently at ambient temperature. Although many of ceramics are considered to be microwave transparent at

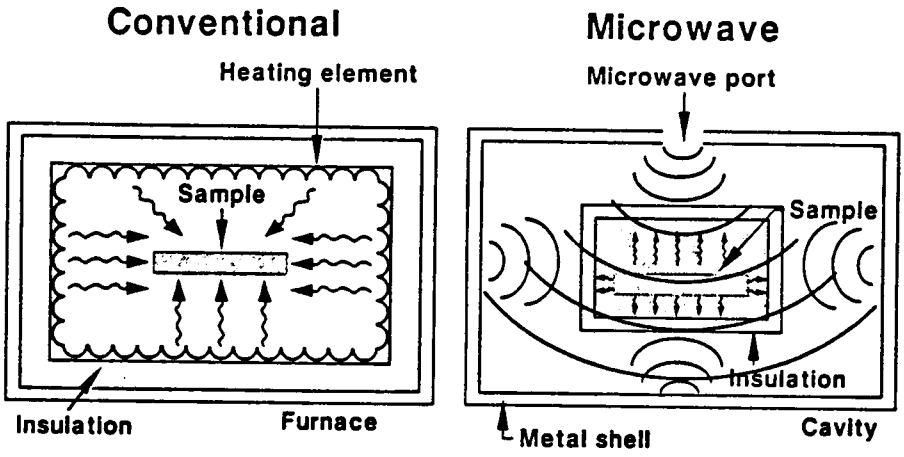


Figure 1. Heating patterns in conventional and microwave processes.

Source: W. H. Sutton, "Microwave Processing of Ceramic Materials," Ceramic Bulletin, Vol. 68 (2), p. 376-86, (1989).

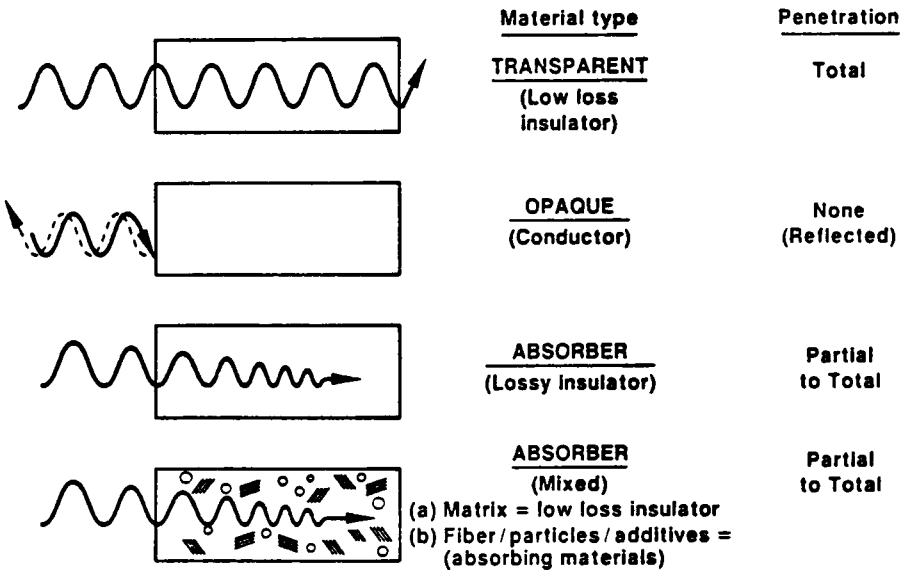


Figure 2. Interaction of Microwaves with materials.

Source: W. H. Sutton, "Microwave Processing of Ceramic Materials," Ceramic Bulletin, Vol. 68 (2), p. 376-86. (1989).

room temperature, the degree of microwave transparency depends on the temperature of the material if it has been heated. When heated to above a critical temperature, these materials begin to absorb and couple more efficiently with microwave energy.

For this reason, Feiker (2) used 915 MHz microwave radiation with a 3.5 KW commercial preheater to heat dielectric materials. Couderc (52) reported that materials such as iron chloride, niobium oxide, etc. at frequencies near 3 GHz showed a sharp increase in dielectric loss after reaching a temperature of from 250 °C to 300 °C. Schubring (12) suggested that a hybrid system of gas and microwaves would be advisable in overcoming the difficulty of getting microwave absorption at low temperature; namely, inexpensive gas energy for low temperature heating but microwave at medium and high temperature for speed and calorimetric control.

Also, the absorption of microwaves by these ceramics can be greatly enhanced by adding impurities (e.g., conductive or magnetic materials). In these materials, the conductive or magnetic phases will absorb microwave energy far more rapidly than the matrix and then will be heated selectively and rapidly. For example, conduction losses for Al_2O_3 are the most important loss mechanism at microwave frequencies for temperature above 400 °C. Pure Al_2O_3, like most ceramic dielectrics, is transparent to 2.45 GHz microwaves at room temperature and cannot be effectively heated unless the conduction losses are enhanced. This can be accomplished by adding impurities to the materials. Ceramics in the green state usually contain binders that are polar and as such will absorb microwave

energy at low temperature. As the temperature of the body increases, the loss tangent of that body will also increase and start absorbing microwave energy.

The degree of absorption of microwaves by a dielectric material is related to the material's complex permittivity. When microwaves penetrate and propagate through a dielectric material, the internal electric fields generated within the affected volume induce translational motions of free or bound charges and rotate charge complexes such as dipoles. These phenomena will be discussed in the following section.

The value of the relative dielectric constant is a measure of the polarizability of a material in an electric field. The loss tangent can be commonly written to describe losses as below;

$$\tan \delta = \frac{\sigma}{2 \pi f \kappa' \varepsilon_o} \qquad \text{(II-1)}$$

where f is the frequency, κ' is the relative dielectric constant, σ is the electrical conductivity and ε_o is the permittivity of free space. The value of the loss tangent is a measure of the loss of the microwave energy within the material.

The relative dielectric constant and the loss tangent are widely used and measured parameters that describe the behavior of a dielectric material under the influence of an electromagnetic field. During the heating κ' and tan δ change with temperature, and a knowledge of these changes is important for process control.

The most extensive experimental studies have been done by Von Hippel and his co-workers (1) at the MIT Laboratory for Insulation Research. These measurements were preliminary carried out with pure organic and inorganic solids and liquids at ambient temperature, although some temperature studied up to a few hundred degrees centigrade were also included. Subsequent work was continued at the same institution by Westphal (53) for the Air Force Materials Laboratory. These publications listed close to a thousand different types of materials. The frequency was increased to 25 GHz and the temperature was extended into the 500 to 1000 °C range.

Figure 3 (54) shows that κ' of fused SiO_2, Si_3N_4, hot-pressed BN, and a glass-ceramic increase slowly from ambient temperature to 1400 °C and that κ' of alumina increases at a great rate. Ho (51) reported that the observed increase in dielectric constants with temperature was caused by an increase in polarizability due to volume expansion. In addition, the composition and the density have a major influence on the κ' as shown in Figure 3.

In the other hand, tan δ is far more affected by temperature as shown in Figure 4. In general, tan δ initially rises slowly with increasing temperature until critical temperature is reached, beyond which tan δ rises rapidly. Ho (51) explained why the tan δ of the 99% pure Al_2O_3 sample was less affected by temperature than that for the less pure material. The reason was that the rapid increase in loss tangent at high temperatures commonly observed in polycrystalline ceramics was associated with softening of

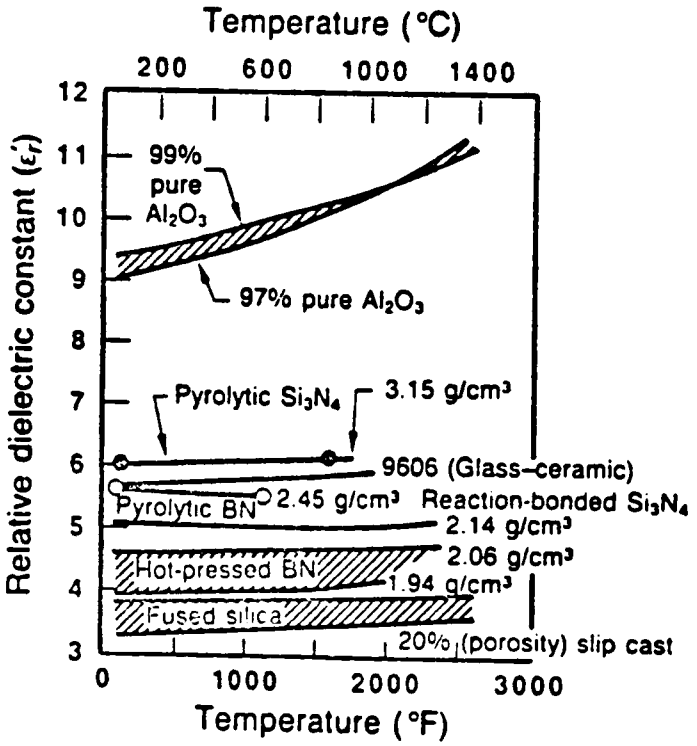


Figure 3. Relative dielectric constant (8 to 10 GHz) versus temperature.

Source: W. H. Sutton, "Microwave Processing of Ceramic Materials," Ceramic Bulletin, Vol. 68 (2), p. 376-86, (1989).

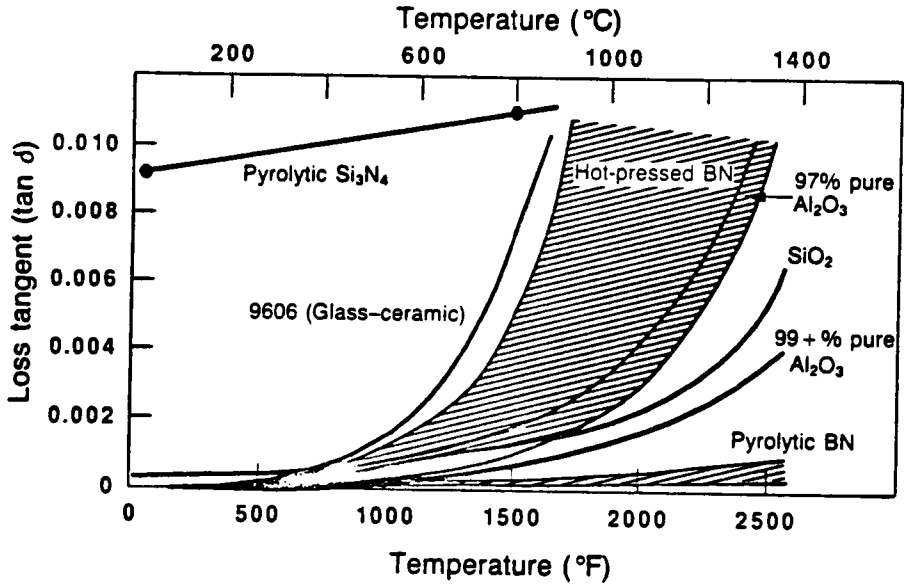


Figure 4. Loss tangent (8 to 10 GHz) versus temperature.

Source: W. H. Sutton, "Microwave Processing of Ceramic Materials," Ceramic Bulletin, Vol. 68 (2), p. 376-86, (1989).

intergranular amorphous phases resulting in an increase in localized electrical conductivity.

II-1-b. Loss Mechanism

The dielectric losses relate the value of the electric field within the material to the value of the electric field externally applied to the material. Many dielectric ceramics have the ability to be polarized by an applied electric field. As a result, the average internal field is reduced. The amount by which the internal field is reduced is proportional to the dielectric constant of the material. As a material is polarized by an external field, it reorders the molecules in the material and does this by adding potential energy to the state of each molecule. If now the external field is suddenly removed, the molecules will try to return to their random orientation. To achieve this the stored potential energy converts into random energy which causes molecules to collide and give up their extra energy in the form heat. This loss of externally applied energy within a material is commonly referred to as relaxation. This time lag between the applied field and the resultant polarization implies an irreversible degradation of energy to heat.

There are two things taking place within a dielectric material when an electric field is applied to it. There is a reduction of the average internal field within the dielectric material which gives rise to a real part of the complex dielectric constant, normally just called dielectric constant, ε' and the associated relaxation phenomena which are described by the imaginary part of the dielectric complex

constant, denoted by ε'', often called loss factor. Then the total complex dielectric constant is written as $\varepsilon = \varepsilon' - j\,\varepsilon''$. The -j indicates a 90 degree phase shift between the real and imaginary part of the complex dielectric constant. The loss tangent is defined as the ratio of the dielectric loss to the dielectric constant.

The frequency at which a dielectric is used has a critical effect on the importance of different relaxation phenomena. As for mechanical-energy losses, the maximum dielectric loss occurs when the period of the relaxation process is the same as the period of the applied field. When the relaxation time is large compared with the period of the applied field, losses are small. Similarly, when the relaxation process is rapid compared with the frequency of the applied field, losses are small. Therefore, certain loss mechanisms will result in substantial energy absorption for 2.45 GHz radiation.

Dielectric losses in ceramic materials are due to loss mechanisms some of which are discussed below. Figure 5 shows dielectric losses due to four polarization mechanisms (1,55). In general, four loss mechanisms can occur, the mix of which depends on the frequency and the temperature. The total electromagnetic losses are the sum of individual contributions.

Near room temperature, energy losses in dielectric ceramics result from three primary mechanisms: (1) ion migration losses: a. conductivity losses, b. ion jump and dipole relaxation losses, (2) ionic vibration losses, and (3) electronic polarization losses (56). These mechanisms are due to charges that are locally bounded in atoms, in molecules, or in the structures of solids and liquids.

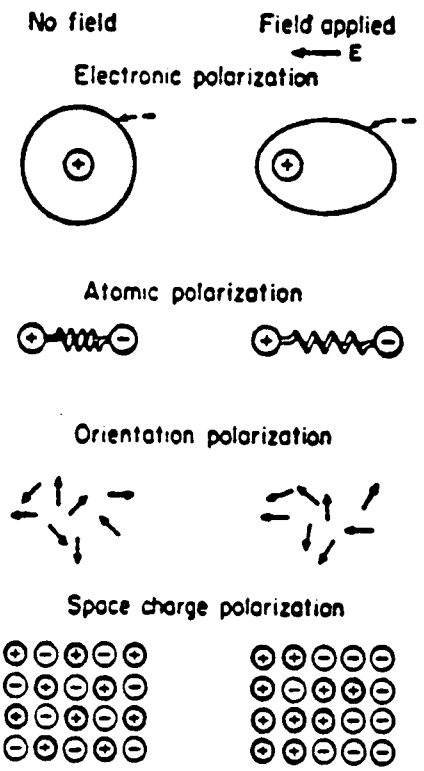


Figure 5. Mechanisms of polarization.

Source: A. R. Von Hipple, Dielectric Materials and Applications, John Wiley and Sons, Inc., New York, (1954).

Electronic polarization losses occur at sufficiently high frequencies in the optical range of frequencies. This phenomena is caused by the shift of the center of gravity of the negative electron cloud in relation to the positive atom nucleus upon the application of an external electric field. In this optical frequency range, the relative dielectric constant is equal to the square of the index of refraction from Lorentz's and Mosotti's equation (55). **Ionic vibration losses** are important at room temperature only at frequencies in the infrared corresponding to 10^{12} to 10^{14} Hz. These can be more significant for these frequency ranges at high temperature because of an increasing contribution resulting from ion mobility and crystal imperfection mobility. These arise from the displacement of ions of opposite sign from their regular lattice sites under the influence of an applied electric field and also from the deformation of the electronic cells from the relative displacement of the ions. The ion displacement is given by;

$$d_i = \frac{z\,e\,E}{u_o^2}\left(\frac{1}{m} - \frac{1}{M}\right) \qquad \text{(II-2)}$$

where d_i is the ion displacement of ion, ze is the ionic charge, u_o is the lattice infrared vibration absorption frequency, and m and M are the mass of the ions. From equation II-2 and II-6 to II-8, an ionic dielectric constant can be calculated. The main contribution to the dielectric constant results from ion displacement in most silicates and aluminates. The dielectric constant of these materials is in the range

of 5 to 15.

Ionic migration losses occur at low frequencies well below microwave frequencies and are due to the of tendency electric dipoles to line up in the direction of the applied field. **Ion jump losses** are of decisive important in liquids such as water and in molecular solids and gases, but these are not of major concern for the dielectric ceramics. The major factor affecting the use of ceramic materials is the **conduction migration losses** which tend to increase at low frequencies and as the temperature raised.

As a rule, the total electromagnetic losses for a ceramic increase with temperature. While each loss mechanism contributes separately to the overall increase, conduction losses have typically been found to predominate at high temperature (5,11,52,53).

Although such conduction losses are small relative to other losses at room temperature, the exponential increase in conductivity with elevated temperature for dielectric ceramics results in an increase in the loss tangent. Although ceramics are considered to be microwave transparent, and at ambient temperature are so, the degree of microwave transparency depends on the temperature of the ceramic and if it has been heated.

II-2. Microwave Heating Theory

The purpose of this section is to present a model for the heating of dielectric materials in an electromagnetic field. Microwave heating theory is found in many places in the literature (22,43,57). The heating model proposed by Meek (22) in an electromagnetic

field describes how the electromagnetic field behaves at an interface between two dielectric media. Modeling of microwave heating can be used to predict and improve temperature profiles in the material being heated. This work considers a porous zirconia-alumina composite with one phase being air; one dielectric media is a zirconia-alumina composite and the other is air. Figure 6 shows a boundary between two perfect dielectric media.

It is important to introduce the following definitions;

$$\mathbf{E} = \nabla V \qquad \text{(II-3)}$$

$$\mathbf{D} = \varepsilon_o \mathbf{E} + \mathbf{P} = \varepsilon' \mathbf{E} \qquad \text{(II-4)}$$

where ∇V (volt/m) = V/t, V is the applied electric potential, t (m) is the distance across which the voltage V is dropped or dissipated, **E** (volt/m) is the vector electric field intensity, **P** (coul/m^2) is the vector electric polarization, ε_o (farad/m) is the dielectric constant in vacuum, ε' (farad/m) is the dielectric constant of a dielectric material, **D** (coul/m^2) is the vector electric flux density. The polarization is the surface charge density of the bound charge, which equals to the dipole moment per unit volume of the material;

$$\mathbf{P} = \varepsilon' \mathbf{E} - \varepsilon_o \mathbf{E} = \varepsilon_o(\kappa'-1) \mathbf{E} \qquad \text{(II-5)}$$

$$\mathbf{P} = N m \qquad \text{(II-6)}$$

$$m = Q d \qquad \text{(II-7)}$$

where N is the number of dipoles per unit volume, m (coul/m) is the electric dipole moment, Q (coul) is the electric charge, d is the

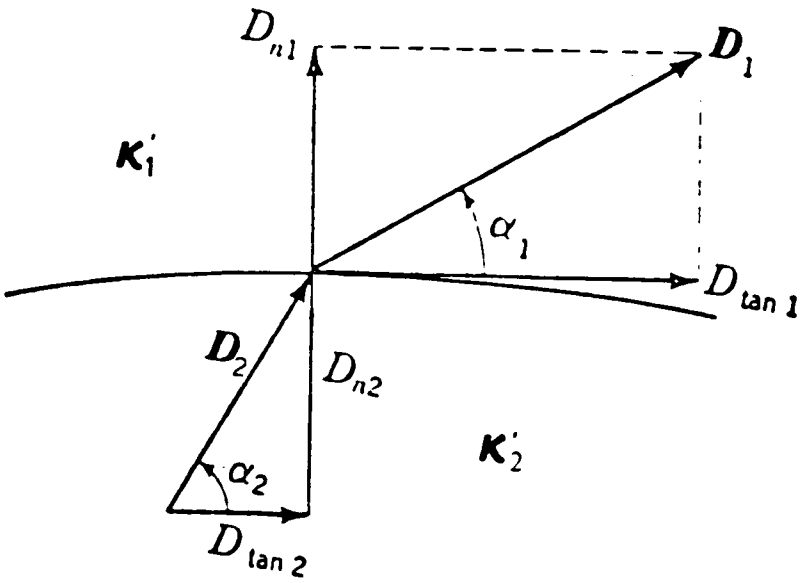


Figure 6. The refraction of **D** at a dielectric interface. For the case shown, $k_1>k_2$. $\mathbf{E}_1$ and $\mathbf{E}_2$ are directed along $\mathbf{D}_1$ and $\mathbf{D}_2$. $D_1>D_2$, and $E_1>E_2$.

Source: W. H. Hayt Jr., Engineering Electromagnetics, McGraw-Hill Book Co., p. 123-28, (1958).

distance between two electric charges of opposite sign, and κ' (= $\varepsilon'/\varepsilon_o$) is the relative dielectric constant. The susceptibility (χ) is the ratio of the bound-charge density to the free-charge density;

$$\chi = \kappa' - 1 = \mathbf{P} / \varepsilon_o \mathbf{E} \qquad \text{(II-8)}$$

II-2-a. Electric Field Intensity

The heating model is introduced by using an expression provided by Hayt (57). Let the relative dielectric constant κ_1 of region 1 be greater than the relative dielectric constant κ_2 of region 2, then the electric field intensity (Volts/cm) is described by;

$$\mathbf{E}_2 = \mathbf{E}_1 \left[\cos^2\alpha_1 + (\kappa_1 / \kappa_2)^2 \sin^2 \alpha_1 \right]^{1/2} \qquad \text{(II-9)}$$

For the case where $\alpha_1 = 90°$, equation II-9 may be reduced to $\mathbf{E}_2 = \mathbf{E}_1 (\kappa_1 / \kappa_2)$. This expression shows that the magnitude of the electric field intensity is greater in the lower dielectric constant region and less in the higher dielectric constant region. It also indicates where an electromagnetic field will deposite its energy in a porous green body and how the location of this energy will vary as the ceramic body is heated.

II-1-b. Power Density

Power density (watts/cm^3) is described by;

$$P = K f \mathbf{E}^2 \kappa' \tan \delta \qquad \text{(II-10)}$$

where P is the absorbed power per unit volume, K is a constant, f is the frequency of the incident electromagnetic radiation, **E** is the

vector electric field intensity, κ' is the relative dielectric constant, and tan δ is the loss tangent. This expression indicates that power absorbed in the material is directly proportional to frequency, the square of the electric field, the dielectric constant, and the loss tangent. Therefore, the dielectric constant and loss tangent of a material is a measure of its efficiency in absorbing microwave energy. In addition, f, κ', tan δ, and **E** are all interdependent. **E** is dependent on the size, geometry, and location of the material within a microwave cavity and on the design and volume of the cavity.

Moreover, this expression shows that more power is deposited into the lower dielectric constant region (lower density region) than into the higher dielectric constant region (fully dense region). It is beneficial to characterize how a ceramic will heat in an electromagnetic field. The above means that the electromagnetic field deposites its energy at just the correct location within the material to do the most good.

II-2-c. Half-Power Penetration Depth

Half-power penetration depth (cm) is described by;

$$H = 3 \lambda_o / [\ 8.686 \pi (\kappa')^{1/2} \tan \delta\ ] \qquad \text{(II-11)}$$

where H is the half-power depth, and λ_o is the characteristic wavelength of the incident radiation. The half-power depth is defined as that distance into a material, in a specified configuration, where the power is reduced to one half that at the surface. For water, the half-power depth (H) is about 3 inch for 915 MHz and

about 0.5 inch for 2.45 GHz radiation. Although low frequencies result in greater penetration depths, the heating does not necessarily increase, since the internal field **E** could be low.

This expression shows that the half-power penetration depth into the lower dielectric constant region is larger than into the fully dense region. The penetrating action of microwave energy into the material results in the internal heating of large cross sections uniformly in a relatively short period of time. However, conventional heating depends upon conducting heat from the surface into the center and is completely dependent on the heat transfer characteristics of the material.

II-2-d. Heating Rate

Heating rate is described by;

$$dT/dt \approx 8 \times 10^{-12} f E^2 \kappa' \tan \delta / (g C_p) \qquad \text{(II-12)}$$

where dT/dt is the heating rate (°C min^{-1}), g is the density of material, and C_p is the heat capacity of material. This is only an approximate increase in temperature resulting from the absorption of microwave energy becasuse it does not include heat loss due to conduction, convection, radiation, or change of state. Also, it is only an average heating rate since the lower density regions will heat faster in an electromagnetic field than the already sintered regions.

II-3. Parameters Affecting the Dielectric Constant

A materials' dielectric constant depends on many parameters

such as the moisture content, the density, the conductivity, and the physical geometry of materials, temperature, and frequency.

The amount of moisture in dielectric ceramics affects their dielectric constant. The reason is that water has a very high dielectric constant, approximately 80, whereas the dielectric ceramics have much lower dielectric constants. Thus, as the moisture content increases in the material, its dielectric constant increases. However, its effect is neglected because dielectric ceramics are assumed to have almost no moisture in experiments.

The density of a material can greatly affect the value of the dielectric constant. The dielectric constant of air is 1.006 and air is considered completely transparent to microwaves at 2.45 GHz. All other nongaseous materials have dielectric constants larger than one. Therefore, air inclusions will always reduce a materials' dielectric constant below the value of the theoretically dense material. Hence, as the density of a material increases, its dielectric constant increases.

The physical structure of the material to be treated in a microwave system will influence the interaction phenomena. It is often difficult to determine accurately the dielectric properties because of density and size variations in the material and these variations may well occur as a natural result of the process itself.

Electrical conductivity is a term which electrical charge through a material, and the resistance of the material will determine how rapidly it will heat transfer describes the ablity of a substance to conduct heat throughout material's volume. The conductivity at

microwave frequencies can be neglected for many materials but in particular cases (e.g., Al_2O_3) it may be a major factor. Electrical conduction in a material at microwave frequencies often cause difficulties in coupling microwave energy into the material and usually is not a desirable property. The electrical conductivity, which is proportional to mobility, is strongly dependent on temperature. It is apparent that imputities significantly affect the electrical conductivity and the dielectric loss factor. Impurities often enhance the conduction mechanism by reducing the energy gap between the valence and conduction bands. As a matter of fact, the introduction of impurities can be used to increase the electrical conductivity and loss factor to the desired level in some cases.

Temperature and frequency dependence of the dielectric constant are related, and for a relaxation type of absorption mechanism can be shown to be inverse functions. Therefore, if frequency dependence of a material's dielectric constant is known, then the temperature variation trend for that material can be estimated. If the frequency of microwaves is varied, the dielectric constant will change as will its temperature. However, only a few choices of frequency are available because of the Federal Communication Commission Regulations. At 2.45 GHz microwave frequency, the loss factor increases with increasing temperature for many ceramics.

The temperature dependence of dielectric constants can be quite complex. Dielectric loss of materials may increase or decrease with temperature at a specified frequency. For water, below 3,000 MHz

the dielectric constant as a function of frequency decreases as the temperature rises, while above 10,000 MHz, the value increases as shown in the tabulated values presented by Von Hippel (1).

II-4. Characteristics of Applicators

The applicator is a device that provides for applying the microwave energy from the generator to the load. The selection of applicators for specific uses is a broad subject. However, it is an important aspect of microwave processing.

II-4-a. Muti-Mode Applicator

The most common type of applicator is the multi-mode cavity which is a closed metal box and can accept a wide range of loads. Its chief drawback is that the non-uniform electric field distribution can cause inhomogeneous heating and hot spots.

The volume and location of the load within the cavity can be critical, since the heating efficiency and uniformity will vary, depending on the location of the field gradients. The reason is that when microwaves are transmitted into a muti-mode cavity, they are reflected on and off of the cavity walls to form a complex pattern of standing waves, which produce regions of high and low field intensity. To produce more uniform heating, mode stirrers, a turn-table, or other devices are used. The filling factor, which is the ratio of the loads volume to that of the cavity, also affects the heating efficiency of the cavity.

II-4-b. Single-Mode Applicator

The single-mode applicator is used for precise and predictable control over the microwave fields within the load. By allowing only one mode to exist within the cavity, amplification of the electric and magnetic fields takes place due to superposition and the locations of the field strength maxima and minima are fixed. Such an applicator can maximize the electric field strength at the load location so that rapid and uniform heating can be achieved.

The design of the applicator can also be changed to provide localized heating in specific regions of the load, which is desired in the case of joining materials together, drawing glass fibers, or creating plasmas to rapidly sinter various ceramic materials.

II-4-c. Resonant Applicator

A common resonant applicator is very simple in construction. It is advantageous that the resonant cavity can be well matched to the microwave generator and thus little power is lost. The high Q factor of the circuit amplifies the field inside the applicator, so that the effective microwave field, to which the load is exposed, is greater than that of the propagating wave which generator would supply in a standard waveguide.

II-5. The Equivalent Exciting Field and Heat Generated

The total electric field intensity in the load may be calculated using the Galerkin method; this requires knowing the Green's function of the specific applicator geometry used. The Green's function of a resonant cavity excited by a rectangular waveguide is

not known. Nevertheless, the total electric field intensity in the load may still be calculated using the Galerkin method, by transforming the cavity problem into an equivalent infinite waveguide problem.

The sum of all the fundamental wave components propagating towards the load is the equivalent exciting field. The equivalent exciting field, which is the total electric field intensity, may be calculated by replacing the applicator and the load by their equivalent circuits and summing the multiple partial reflections between the waveguide and the load and between the load and the cavity, respectively.

Utilizing the variational model of the load and the consequent equivalent circuit approach makes it possible to determine the magnitudes and phases of all the partial multi-mole reflections inside the cavity without exactly knowing the total electric field intensity in advance.

The total amount of heat generated in the cavity normalized to the available microwave power from the microwave generator, P_n, may be expressed by

$$P_n = 1 - P_{nr} = 1 - |\xi|^2 \qquad \text{(II-13)}$$

where ξ is the reflection coefficient of the cavity; and ξ may be expressed by,

$$\xi = (1-Y_L) / (1+Y_L) \qquad \text{(II-14)}$$

where Y_L is the normalized admittance of the equivalent circuit of

the cavity evaluated at the plane of the iris. The available microwave power is the amount of power absorbed by a perfectly matched load, i.e., a load with $\xi = 0$. The expression for Y_L depends upon the T-equivalent circuit impedances of the load, the size and shape of the iris. Ideally, no heat is generated in the waveguide and the cavity walls when they are lossless.

In actuality, when very low-loss materials are in the cavity, the losses of the waveguide and the cavity walls occur. In this case, a significant fraction of the total heat generated in the cavity is actually generated in the cavity wall. When very high-loss materials are in the cavity, practically all of the heat generated is generated in the materials. The former case is manifested in experiments where the external portions of the cavity are warm to the touch while the load is unable to achieve a high enough temperature to be incandescent. In the latter case, the cavity wall is relatively cooler to the touch than in the former case even when the surface temperature of the load is already up to 1800 °C.

II-6. Thermal Stability and Temperature Control

While heat is generated at each point inside the load, heat is lost by radiation and convection at the surface of the load. When conductivity varies with temperature, in general it becomes non-uniform as the temperature reaches a steady-state temperature profile.

Initially the heat losses at the surface tend to make the surface temperature lower than the axial temperature since the heat

generated near the surface is dissipated first. The resulting temperature gradient makes it possible for the internally generated heat to be conducted to the surface for dissipation by radiation and convection.

If the thermal conductivity of the load is high, the required temperature gradient to conduct the same amount of heat is less. A practically uniform temperature profile is therefore possible, when the load is thin, if both electrical and thermal conductivities increase to large values at high temperatures. This is because the inverted electric field intensity profile tends to make the heating rate smaller inside than at the surface while the high thermal conductivity tends to make the temperature gradients small.

On the other hand, a combination of a rapidly increasing electrical conductivity with temperature and a small thermal conductivity will lead to a very steep temperature gradient between the very hot axial region and the relatively cooler surface. It is possible that due to the rapid rise in electrical conductivity inside the sample, the amount of heat generated internally is more than can be conducted to the surface even by the increasing temperature gradient. The internal temperature will then rise rapidly to the point of melting the core of the load. When this happens, thermal instability corresponds to an indefinite rise in temperature to an infinite value.

II-6-a. Thermal-Instability

The transient temperature profile in the load may be calculated

by using the heat equation (58) subjected to certain boundary conditions;

$$mC_p \, \partial T/\partial t(\mathbf{r},t) = \nabla \cdot [\, k \nabla T(\mathbf{r},t) + g(\mathbf{r},t)] \qquad \text{(II-15)}$$

where m is the mass density of the material, C_p is the heat capacity of the material, $\nabla T(\mathbf{r},t)$ is the temperature profile, and $g(\mathbf{r},t)$ is the generated heat per unit volume profile. In general, m, C_p, and k vary with temperature.

The boundary condition at the surface of the load is expressed by;

$$- k(\mathbf{r},T) \nabla T \, \mathbf{n} = h(\mathbf{r},t) \, (T - T_a) + e(\mathbf{r},T) \, \psi T^4 - R_i \qquad \text{(II-16)}$$

where, h is the convective heat-transfer coefficient, e is the emissivity of the surface, T_a is the ambient temperature, $\mathbf{n}$ is the outward normal unit vector and ψ is the Stefan-Boltzmann constant (5.67×10^{-8} watts/m°K^4). The first two terms on the right-hand side represent convection and radiation loss, respectively, while the lost term, R_i, represents the radiative heat transferred to the load from the walls of the cavity due to the non-zero temperature of the walls.

In general equation II-15 and II-16 will have to be solved in conjunction with other boundary conditions on temperature. When conductivity varies with temperature, the above equations will have to be solved simultaneously with the wave equation for the electric field and its associated boundary conditions. In this case, the problem becomes extremely difficult to solve.

Araneta (59) assumed that the electric field intensity is constant relative to r; conductivity is a linear variation with temperature: $g(\mathbf{r}) = g_o = AT(\mathbf{r})$ where A is a constant of proportionality and g_o is a constant: and k, m, and C_p are constant. After he solved this case, he concluded that thermal instability may be prevented by using smaller values of the available power (P_a) times the normalized power (P_{nr}) and/or smaller radius and/or increasing the thermal conductivity of the load.

Smaller values of $P_a \cdot P_{nr}$ may be achieved by reducing the output power of the microwave generator and/or detuning the cavity to reduce P_{nr}. Increased thermal conductivity may be achieved by reducing the degree of initial porosity of the load as in sintering applications. Finally, loads made of materials whose electrical conductivity decreases with temperature can never become unstable, although in practice there is an upper limit to the temperature levels, e.g., their melting point.

II-6-b. Stable Temperature

Initially, the temperature of the load increases even when electrical conductivity decreases with temperature because the total amount of heat generated inside is greater than the total amount of heat losses. Convection loss and particularly radiation loss are very low at the start because the surface temperature is near the ambient temperature. The elevated temperature levels finally stabilize when the total amount of heat loss is equal to the total amount of heat generated.

When the temperature of the load is uniform, the total amount of heat generated with a given g(T) is proportional to the volume of the load while the total amount of heat losses is proportional to the surface area of the load. Since for a given length the volume varies as the square of the radius while the surface area varies linearly with the radius, a given g(T) will result in a lower stable temperature with smaller diameter load.

When the load is thin and exhibits a practically uniform temperature profile, a first approximation to calculating the stable temperature is to treat the heat generation and heat dissipation problems as uncoupled. The amount of heat generated may then be calculated independently from the calculation for the amount of heat losses. The value of temperature, assumed uniform throughout the load, that makes the calculated generated heat equal to the calculated total loss is the calculated stable temperature.

A very good approximation to the total heat loss, especially in thin loads, is the sum of radiation and convection losses. The reason is that the load is enclosed by the insulation in the cavity. An approximation to the amount of convection loss assumes a uniform ambient temperature throughout the length of the load. When the load is vertical, the convection loss per unit surface area is emprically given by (60);

$$\text{convection loss} = 1.42\ \Delta T^{5/4} / L^{1/4} \quad \text{watts/m}^2 \qquad \text{(II-17)}$$

where, ΔT is the temperature difference between the surface and the ambient temperature and L (m) is the length of the load.

An approximation to the radiation loss assumes uniform surface temperature and that the material radiates like a gray body with a certain amount of emissivity. The radiation loss per unit surface area is then (61);

$$\text{radiation loss} = e\ \psi\ T_s^4 \qquad \text{watts/m}^2 \qquad \text{(II-18)}$$

where, e is the emissivity, ψ is the Stefan-Boltzmann's constant and T_s is the surface temperature in K.

The load also receives thermal radiation from the walls of the cavity. Using the simplest model of radiative exchange between two surfaces, the amount of radiant heat received per unit load surface area is expressed by equation II-18, where e and T_s are replaced by the emissivity and surface temperature of the applicator walls, respectively.

Therefore, the total heat loss per unit load surface area is;

$$\text{heat loss} = 1.42\ \Delta T^{5/4} / L^{1/4} + \psi\ (e_s\ T_s^4 - e_w T_w^4) \qquad \text{(II-19)}$$

where the subscript "s" refers to the surface of the load while "w" refers to the inside surface of the cavity walls. Equation II-19 may then be used to calculate the total heat losses as a function of temperature by multiplying it with the total surface area. The temperature at which the calculated generated heat equals the calculated total heat losses is the estimated stable temperature which is assumed uniform throughout the load. A more detailed calculation for the stable temperature profile was solved by Araneta (59).

II-6-c. Temperature Profile Control

Increasing available power (P_a) will generally result in increased temperature and steeper temperature gradients due to a higher heating rate. If the load is vertical and exposed to the air, the upward flow of heated air by convection makes the upper portion of the rod hotter than the lower end. Increasing the thermal emissivity of the cavity walls and thermally insulating the cavity from the outside will reduce the net radiation loss. Minimizing the amount of radiation and convection loss will result in minimum radial temperature gradients and smaller P_a requirement to maintain the same temperature. Adjusting the single-stub tuner to optimum will result in higher temperature at the same P_a.

Automatic control of temperature levels at a constant value may be implemented by sensing the surface temperature and P_{nr} and automatically changing P_a by negative feedback of the sensed variables.

II-7. Thermal Stresses in Ceramics

The susceptibility of ceramic materials to thermal stresses and thermal shock failure is one of the main factors limiting their usefulness. Because of the absence of any kind of plasticity, the non-uniform thermal expansions which result from the non-uniform temperatures, can not be accommodated by non-linear deformation. The low value of fracture toughness of brittle ceramics also contributes to extensive crack propagation following thermal stress failure.

II-7-a. Fundamental Considerations and Theory

It is clear that in order to calculate thermal stresses we need a knowledge of the relationship between the temperature and thermal stress distribution that occurs when the surface temperature is changed instantly without changing the average temperature of the body from its initial value. The temperature and stress distribution for heating and cooling the surface of an infinite slab at a constant rate is shown in Figure 7 (62). On cooling, the maximum stress is the tensile stress on the surface and the center is in compression. On heating, the maximum stress is the compressive stress on the surface, and the center is in tension.

Since ceramic materials are much weaker in tension than under compression, failure usually occurs at the surface during cooling but can also occur either from the center tensile stress or from the surface compressive stress during heating. However, the presence of flaws on the surface and their interaction with tensile stress make failure more probable during rapid cooling.

These stresses can be calculated for perfectly elastic materials, of which many ceramics are a good approximation, from the elastic modulus, the coefficient of thermal expansion, and the temperature distribution. Under these conditions the rate of heat transfer from the surface is high; the surface reaches the new temperature instantly, but the interior remains at a uniform value, the temperature difference gives the strain at any point and fixes the stress. The restraint on free strain leads to a stress for a slab infinite in the y and z directions and finite in the x direction given by;

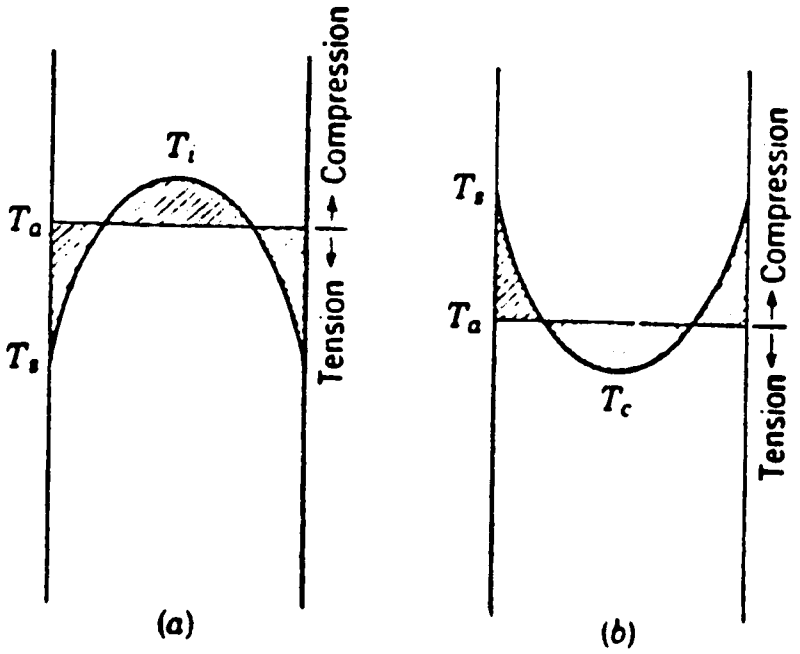


Figure 7. Temperature and stress distributions for plate that is (a) cooled from the surface and (b) heated from the surface.

Source: S. Timoshenko, Theory of Elasticity, p. 415 3rd ed., McGraw Hill Book Co., Inc., New York (1970).

$$\sigma_y = \sigma_z = \frac{E\,\alpha}{1 - \mu}\,(T_o - T') \qquad \text{(II-20)}$$

where E is the modulus of elasticity, α is the thermal expansion, μ is the Poisson's ratio, T_o is the original initial temperature, and T' is the new temperature.

II-7-b. Initiation of Thermal-Shock Failure

Resistance to weakening or fracture under a rapid temperature change (thermal shock) is called thermal endurance, thermal stress resistance, or thermal shock resistance. The effect of thermal stresses on different kinds of materials depends not only on the stress level, stress distribution in the body, and stress duration but also on material characteristics such as ductility, homogeneity, porosity, and existing flaws. Consequently, defining a single thermal stress resistance factor is impossible to satisfy for all situations.

If considering an ideally elastic material which fractures when the surface stress reaches some particular level, the temperature conditions for fracture can be simplely calculated. For rearranging equation II-20 with $\Delta T_f = T_o - T'$, and $\sigma_y = \sigma_z = \sigma_f$;

$$\Delta T_f = \frac{\sigma_f\,(1 - \mu)}{E\,\alpha} \qquad \text{(II-21)}$$

where ΔT_f is the temperature difference at fracture, and σ_f is the fracture stress. For other shapes, equation II-21 may be expressed

with other geometrical constants as below;

$$\Delta T_f = \frac{\sigma_f (1 - \mu)}{E \alpha} S = R S \qquad \text{(II-22)}$$

where S is the geometric factor, and $R = \sigma_f (1 - \mu) / E \alpha$ is a material resistance factor for thermal stresses. From the above equation, a high fracture stress, low modulus of elasticity, and low thermal expension coefficient indicates a good resistance to thermal stress failure.

In fracture-mechanical terms, the fracture stress can be expressed;

$$\sigma_f = Y K_{IC} / a_o^{1/2} \qquad \text{(II-23)}$$

where K_{IC} is the critical stress intensity factor, Y is a constant related to the geometry of the failure initiating the crack, and a_o is the crack size or depth. Substitution of equation II-22 into equation II-23 yields;

$$\Delta T_{max} = \frac{S Y K_{IC} (1 - \mu)}{\alpha E a_o^{1/2}} \qquad \text{(II-24)}$$

If in the region of the failure initiating flaw, a compressive stress (σ_c) exists, ΔT_{max} can be expressed by;

$$\Delta T_{max} = \frac{S Y K_{IC} (1 - \mu)}{\alpha E a_o^{1/2}} + \frac{S \sigma_c (1 - \mu)}{\alpha E} \qquad \text{(II-25)}$$

II-7-c. Crack Propagation in Thermal-Shock Failure

All of the before section is predicated on the assumption that failure occurs when the thermal stress reaches the fracture stress. For porous materials and non-homogeneous materials, crack propagation may be stopped by a pore or grain boundary before resulting in complete failure. These considerations lead to a second approach to the problem of thermal shock, which governs the propagation of cracks rather than their nucleation. This approach was proposed by Hasselman (63), who noted that the driving force for crack propagation is derived from the elastic energy stored in the body at the instant of fracture, and on the basis of a modified Griffith criterion, thermal stress fracture would be not catastrophic if the total elastic energy were less than total fracture energy required to propagate a crack. Hasselman expressed the critical temperature difference (ΔT_c) required for crack instability as;

$$\Delta T_c = \left[\frac{\pi\ G\ (1 - 2\mu)^2}{2E_o\ \alpha^2\ (1 - \mu^2)}\right]^{1/2} \times \left[1 + \frac{16(1 - \mu^2)\ N\ L^3}{9\ (1 - 2\mu)}\right][L]^{-1/2} \qquad \text{(II-26)}$$

where G is the fracture surface work, and L is the crack length, and N is the number of cracks per unit volume.

Figure 8 shows a plot of equation II-26. As shown in Figure 8, the region of crack instability is divided by two values of crack length.

For initially short cracks (to the left of the maxima), the term 16 $(1 - \mu^2)\ N\ L^3 / 9\ (1 - 2\mu)$ is small compared to unity. ΔT_c becomes;

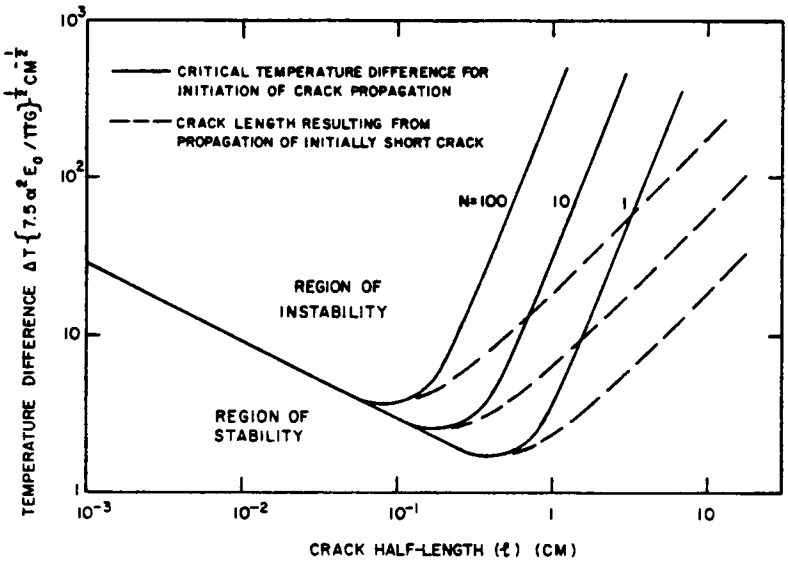


Figure 8. Minimum thermal strain required to initiate crack propagation as a function of crack length and crack density N. (Poisson's ratio = 0.25).

Source: D. P. H. Hasselman, "Unified Theory of Thermal Shock Fracture Initiation and Crack Propagation in Brittle Ceramics," J. Am. Ceram. Soc., Vol. 52, No. 11, p. 600-04, (1969).

$$\Delta T_c = [\ \pi\ G\ (1 - 2\mu)^2 /\ 2\ E_o\ \alpha^2\ (1 - \mu)^2\ L\ ]^{1/2} \qquad \text{(II-27)}$$

Equation II-27 describes the linear region of the left-hand side of the U-shaped curve in Figure 8. For this case, the rate of energy release after the initiation of crack propagation exceeds the surface energy of fracture, and the excess energy is transformed into the kinetic energy of the propagating crack. When such a crack reaches the length given by equation II-27, it still has kinetic energy and continues to propagate until the released strain energy equals the surface energy of fracture. It may be noted from Figure 8 that these final crack lengths (minima of curve) are subcritical with respect to the critical temperature difference required for their initiation, and a finite increase in this temperature difference is required before the cracks again become unstable.

For initially long cracks (to the right of the minima), the term unity is negligible compared to the term $16\ (1 - \mu^2)\ N\ L^3 / 9\ (1 - 2\ \mu)$. ΔT_c becomes;

$$\Delta T_c = [\ 128\ \pi\ G\ (1 - 2\ \mu^2)\ N^2\ L^5 / 81\ \alpha^2\ E_o\ ]^{1/2} \qquad \text{(II-28)}$$

For this case, cracks do not attain kinetic energy and propagate only in a quasi-static manner.

These conclusions are summarized in Figure 9, which shows the crack length and strength behavior following thermal shock of increasing severity. As illustrated, a critical temperature difference is required to initiate fracture, and the discontinuity of strength at ΔT_c is the result of the kinetic crack propagation. The discontinuous

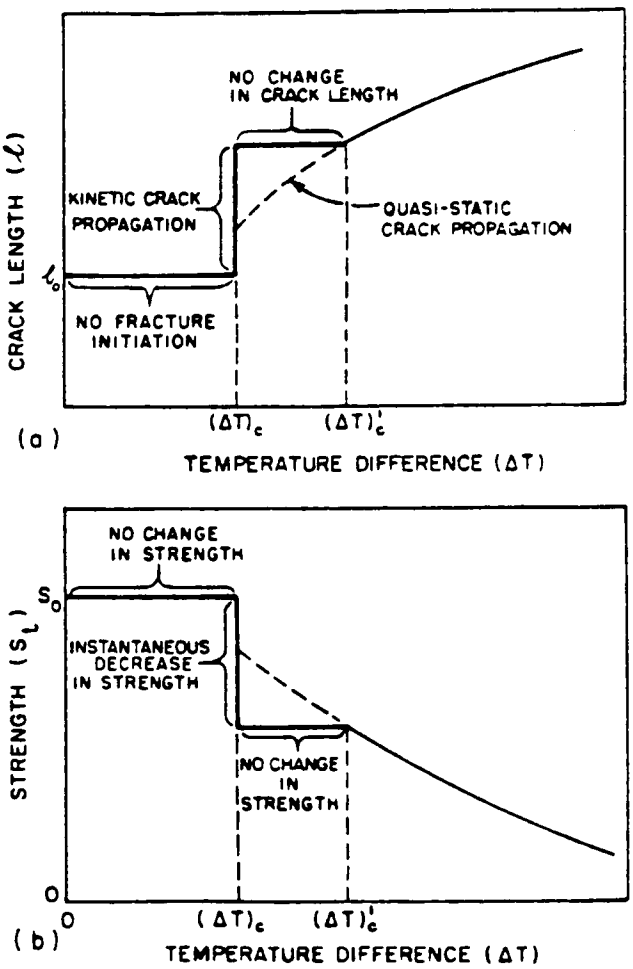


Figure 9. Crack length and strength as a function of thermal history.

Source: D. P. H. Hasselman, "Unified Theory of Thermal Shock Fracture Initiation and Crack Propagation in Brittle Ceramics," J. Am. Ceram. Soc., Vol. 52, No. 11, p. 600-04, (1969).

characteristics were reported for alumina by Ainsworth (64) and Gupta (65,66), for silicon carbide by Coppola (67), for zirconia-alumina composite by Becher (68), and for refractory brick by Nakayama (69).

As a result, over the range $0 < T < T_c$, no change in crack length or strength is expected. At $\Delta T = \Delta T_c$, cracks propagate kinetically, their length changes rapidly to a new value, and the strength also decreases discontinuously. The new crack length is now subcritical to ΔT_c, so that ΔT must be increased to a new value $\Delta T_c'$, before the cracks again continue propagating. Since the cracks are then subcritical, over the range $\Delta T_c < \Delta T < \Delta T_c'$, no further crack propagation occurs, no change in strength is expected. At $\Delta T > \Delta T_c'$, the cracks grow quasi-statically, and the strength decreases gradually with increasing ΔT. The continuous characteristics were reported for a large grain alumina by Gupta (65) and for an alumina-silicon carbide whisker composite by Tiegs (70).

III-7-d. Two general Approaches to the Thermal-Shock Resistance of Ceramics

At the present time, thermal stress resistance of brittle ceramics can be determined by two methods which aid in designing and selecting materials for good thermal shock resistance.

The first approach is based on thermoelastic theory (71). This is appropriate for glasses, porcelain, and electronic ceramics and involves the avoidence of fracture initiation by the thermal stresses. Analytical expressions for the fracture resistance parameters along

with the designations used in the literature were listed by Hasselman (72). From these conditions, a thermal-shock resistance parameter is defined as;

$$R = \sigma_f (1 - \mu) / E \alpha \qquad \text{(II-29)}$$

or

$$R = K \sigma_f (1 - \mu) / E \alpha \qquad \text{(II-30)}$$

To attain an increase in the fracture resistance, high values of strength and thermal conductivity and low values of thermal expansion coefficient and elastic modulus are desired.

The second approach is concerned with the extent of crack propagation. This is important for refractory ceramics, and involves the avoidance of catastrophic crack propagation. It is assumed that the area over which the crack will propagate is directly proportional to the elastic energy stored at the time of fracture and inversely proportional to the fracture surface energy required to propagate a crack. The thermal-shock resistance parameters, R''' and R'''' as defined by Hassleman (72), are given by;

$$R''' = E / S^2 (1 - \mu) \qquad \text{(II-31)}$$

$$R'''' = E G / S^2 (1 - \mu) \qquad \text{(II-32)}$$

In order to attain an increase in the fracture resistance, high values of elastic modulus and fracture surface energy, and low values of strength are required. These requirements of modulus and strength stand in direct contrast to those appropriate for avoiding the initiation of fracture. Thus, selection of material characteristics to

avoid fracture initiation has deleterious effects on the damage resulting from fracture.

Resistance to catastrophic crack propagation can be improved by introducing enough cracks of sufficiently large size so that crack propagation takes place quasi-statically or more generally by introducing microstructural heterogeneities of any form which act as stress concentrators or induce microcracking.

Further improvements in thermal-stress resistance can be achieved by creating a compressive stress, which opposes the tensile thermal stress, in the region of the material where the failure originates. Experimental data (68,73-76) have indicated that incorporating a zirconia dispersed phase in a brittle matrix material can lead to significant improvements in thermal-stress resistance by increasing the fracture toughness, lowering the coefficient of thermal expansion, introducing compressive stresses and by changing the failure mode to the preferred stable mode of crack propagation as will be discussed in the next section.

II-8. Study for Zirconia-Alumina Composite

II-8-a. The Crystal Structure of Zirconia

The existance of a reversible monoclinic-tetragonal transformation in pure zirconia was first reported by Ruff and Ebert in 1929. Pure zirconia is monoclinic below 1100 °C. McClullough (77) proposed the crystallographic structure of monoclinic zirconia as being derived from a cube. The zirconium ion locates in the center of the cube and is in seven-fold coordination with the oxygen ions. Five

of them are located at the corner of each cube and the remaining two ions are located at the midpoints of the cube edge which connect the unoccupied corner. The unit-cell dimensions are a = 5.169 Å, b = 5.232 Å, c = 5.341 Å, and b = 99°15'.

Pure zirconia is tetragonal above 1100 °C. Teufer (78) described the structure in terms of a body-centered tetragonal lattice with the zirconium ions occupying body-centered positions and eight-fold coordination with the oxygen ions. The unit-cell dimensions are a = 3.64 Å and c = 5.27 Å at 1250 °C.

II-8-b. Phase Transformation of Zirconia

Brittle ceramic materials can be toughened and strengthened by utilizing the tetragonal-monoclinic phase transformation of zirconia particles dispered in a ceramic matrix. The phase transformation in this system is athermal, diffusionless, and involves both a shear strain (8%) and a volume change (3% to 5%) (79).

In order to understand toughening, the nature of the tetragonal-monoclinic phase transformation in zirconia should be exaimed. Figure 10 shows the zirconia phase transformation in a matrix and thermal expansion behavior of a zirconia dispersed ceramic. On cooling from high temperature, the tetragonal phase changes to the monoclinic phase at a temperature (T_R), which involves a volume expansion. The stresses caused by this expansion can cause microcrack formation when the particle diameter exceeds a critical value, on reheating to high temperature (T_H). On the other hand, the martensitic start temperature (T_R) of single crystals and

polycrystalline bulk zirconia occurs between 950 °C and 850 °C. Zirconia dispersed matrics are usually retained to low temperatures due to the constraint of volume change by the surrounding matrix. However, when external stress is applied the constraint is relieved by matrix microcracking, the tetragonal phase starts to transform the stable monoclinic phase.

In general, $T_H > T_R$ so that the expansion behavior shows a hysteresis as shown in Figure 10. The scale of the hysteresis curve is a function of the volume fraction of zirconia. Wolten (80) suggested that this tetragonal-monoclinic phase transformation was martensitic in nature. He confirmed the existence of a large hysteresis in an athermal transformation. The phase transformation with the function of T_R and T_H depends on various parameters such as the zirconia particle size (81), the degree of constraint of the matrix (82,83), and the chemical composition, specifically the amount of cubic stabilizing oxide present (76). Large irregularly shaped zirconia particles, containing small amounts of stabilizing oxides, may transform to the stable monoclinic structure during cooling from the sintering temperature, and this can lead to microcracking. Smaller, more spherical particles, or particles containing a larger amount of stabilizer, may not transform on cooling, or when stressed. Therefore, the phase transformation can be controlled by controlling the particle size, the constraint, and the chemical composition.

II-8-c. Transformation Toughening of Zirconia

Transformation toughening has the potential to strengthen

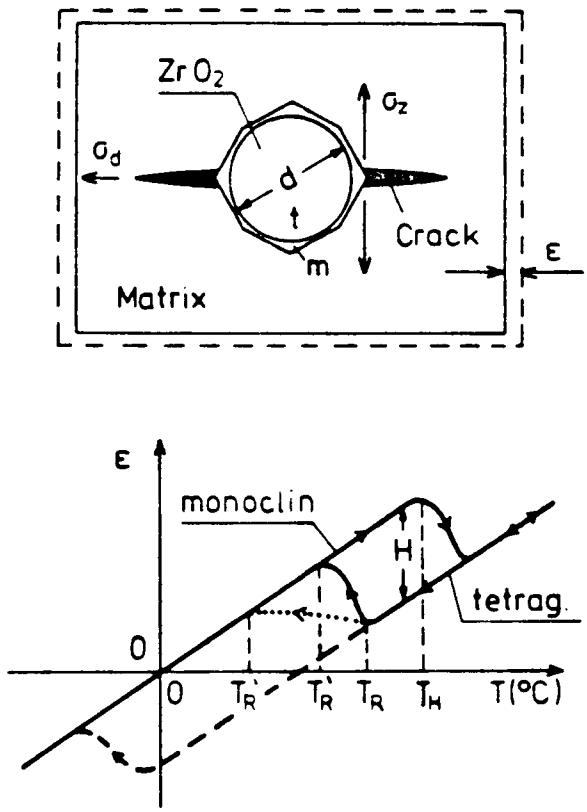


Figure 10. Zirconia particle contained within ceramic matrix, before (t) and after (m) the tetragonal-monoclinic phase transformation and associated thermal expansion behavior of the composite.

Source: N. Claussen and D. P. H. Hasselman, " Improvement of Thermal Shock Resistance of Brittle Structure Ceramics by a dispersed Phase of ZrO_2," in Thermal Stresses in Severe Environments, p. 51-86, (1980).

ceramic materials. Toughening is attained by retention of the tetragonal zirconia in a metastable state, the phase change causes a compressive stress field near an advancing crack. The compressive stress exerts a back stress on the crack (84). This introduces the concept of a process zone around a crack tip as shown in Figure 11 (85).

The toughening mechanism has been analyzed theoretically by Evans (86) and McMeeking (87). This mechanism can be classified by at least two types of toughness enhancement, stress-induced transformation toughening and nucleation-extension of microcracks toughening.

Stress-induced transformation toughening is possible for zirconia dispersions of a small size retained in the tetragonal phase at room temperature. Stress-induced transformation creates steady-state compressive stresses, which can be achieved by two methods (73,88). In one case, the temperature dependence of the phase transformation introduces a transient compressive thermal stress which opposes the tensile thermal stress. During cooling instantly, when thermal stresses reach a critical value, the tetragonal phase converts to the monoclinic phase. The volume expansion associated with this transformation creats a compressive stress in the surface, which can oppose the tensile thermal stress. During fracture, transformation near an advancing crack tip causes the matrix to dissipate elastic strain energy because of the decrease of chemical free energy of the matrix (89). In the other case, toughening by stress-induced transformation is achieved by introducing

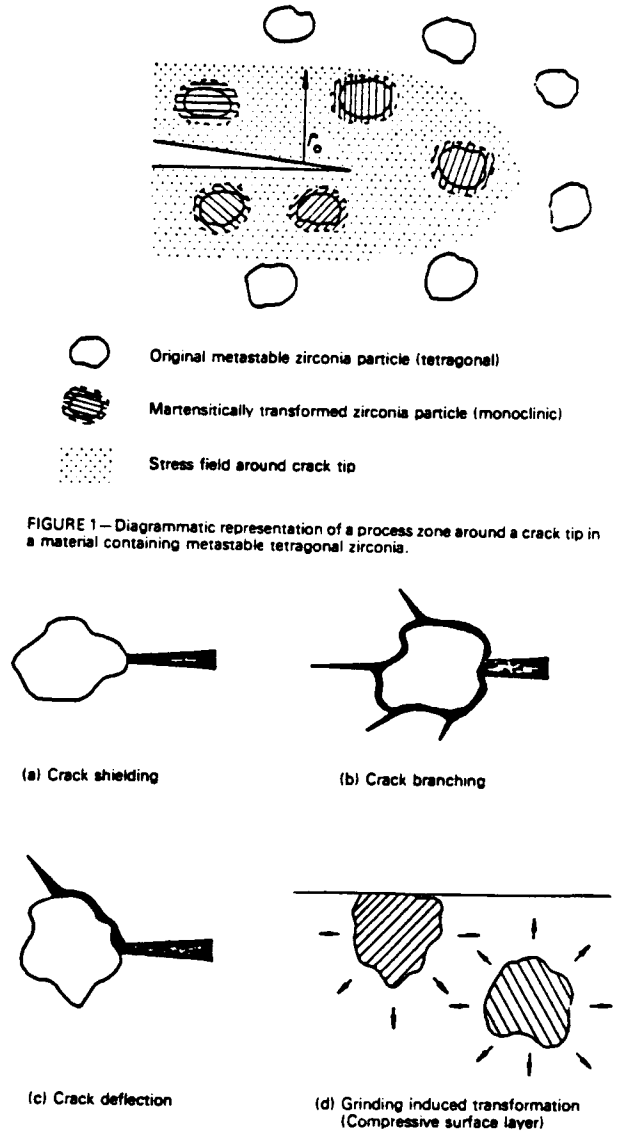


Figure 11. (1) Representation of a process zone around a crack tip in a material containing metastable tetragonal zirconia. (2) Representation of crack particle interactions (a), (b), (c), together with (d) the development of compressive surface layer by transformation of the metastable t-zirconia particles to monoclinic via a martensitic shear process.

Source: R. Stevens and P. A. Evans, "Transformation Toughening by Dispersed Polycrystalline Zirconia," Trans. J. Brit. Ceram. Soc., Vol. 83, No. 1, p. 28-31, (1984).

compressive stresses obtained by the surface grinding. Green (90) and Gupta (91) noted that surface grinding increased the amount of the monoclinic phase of zirconia at the surface and removal of the transformed layer by polishing led to a slight strength decrease. Green showed that in zirconia-alumina composites, annealing of the ground surface caused a strength degradation because of the removal of the surface compressive stresses.

Toughening by nucleation and extension of microcracks occurs at sufficiently large zirconia particle size, the hoop stresses can cause extensive microcracking in the matrix. During failure, the phase transformation provides a higher energy density of microcrack nuclei sites than the zirconia free matrix would exhibit. Thus, microcracks promote crack bifurcation and an enhanced energy absorption, thereby effectively increasing the fracture toughness (92). When a high density of microcracks of sufficient size is introduced in a matrix, crack propagation in a thermal stress field will become stable. Claussen (82) reported that controlled microcracking can be achieved by controlling the zirconia particle size. Large particles can be utilized to induce crack branching as shown in Figure 11.

II-8-d. Improvement of the Properities of a Zirconia-Alumina Composite

Claussen (93) broadly classified the transformation toughened ceramics into three groups: partially stabilized zirconia (PSZ), disperzed zirconia-containing ceramics, and complex zirconia systems

encompassing all other composites not fitting into either group.

Yttria-based tetragonal zirconia polycrystals (Y-PSZ) is a type of PSZ. PSZ has attracted considerable interest as the new structural material because of its high strength and high toughness due to extremely fine grain size and the entirely active transformable phase (94,95). However, the strength and toughness of Y-PSZ decreases markedly with increasing temperature. According to transformation toughening theory, the low values of high temperature strength are due to the decreased contribution of stress-induced transformation toughening. Some approaches were proposed to improve the high-temperature mechanical properties of zirconia toughened ceramics

Alumina toughened zirconia have received considerable attention with high strength and toughness as structural components (96). Butler (97) and Rajendran (98) reported that addition of alumina to stablized zirconia influences the grain size, grain boundary conductivity, and also improves the density of the materials. They explained this improved conductivity as a consequence of the grain boundary glassy phase accumulated at the Y-PSZ/Al_2O_3 interfaces.

Kosmac (99) investigated the relative contributions of monoclinic phase and tetragonal phase zirconia particles to the total toughness increment in the zirconia-alumina composite and the characteristic difference when compared with PSZ. His analysis showed that both microcracking and transformation toughening mechanisms are important for improving the toughness of these composites. The optimum toughening condition of the composite studied occurred

when both mechanisms were operative but the microcracking mode was dominant.

Majumdar (100) studied the rates of densification for the whole range of compositions in the zirconia-alumina composite under hot pressing conditions at 1450 °C. He showed that alumina densified less rapidly under the same conditions as shown in Figure 12. Also Figure 13 shows that the densification rates in zirconia-alumina mixtures as a function of volume fraction zirconia are plotted for relative density values of 0.7 and 0.9 and the densification is not a linear function of the end-member oxides. Figure 14 shows Scanning Electron Micrographs of the fracture surfaces of the end-member alumina and zirconia materials; the finer grain size of the latter is apparent.

Becher (101) reported that tetragonal zirconia additions to the alumina matrix resulted in dramatic improvements in both thermal-shock resistance and strength due to increasing of fracture energy and strength resulting from the zirconia transformation toughening effects.

Lange (102) indicated that considerable amounts of alumina is introduced in yittria-based tetragonal zirconia polycrystals to achieve optimum mechanical properties, and also noted that the strength of alumina-rich composite materials may be improved by hot isostatic processing. He showed that the hardness of the whole range of zirconia-alumina composites obeyed a linear rule of mixtures. He observed that the average grain size of zirconia for the composite material was dependent on the fabrication temperature:

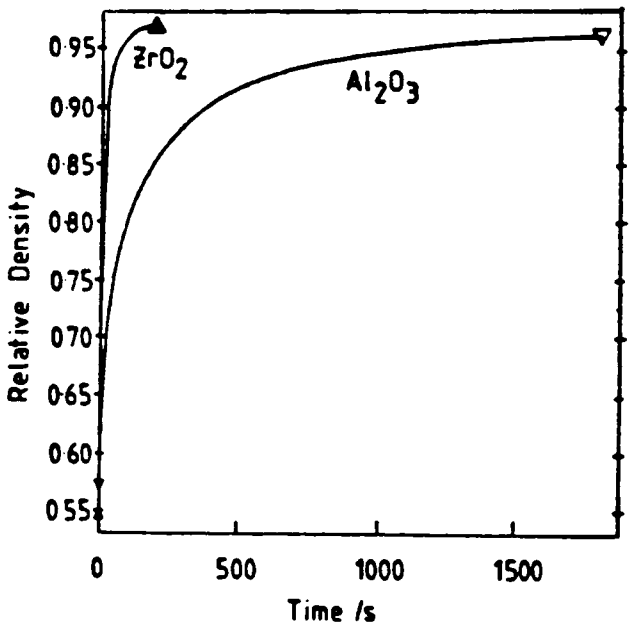


Figure 12. Densification during hot pressing (1350 °C; 20 MPa) of the individual powders.

Source: R. Majumdar, E. Gilbart, and R. J. Brook, "Kinetics of Densification of Alumina-Zirconia," Trans. J. Brit. Ceram. Soc., Vol. 85, No. 5, p. 156-60, (1986).

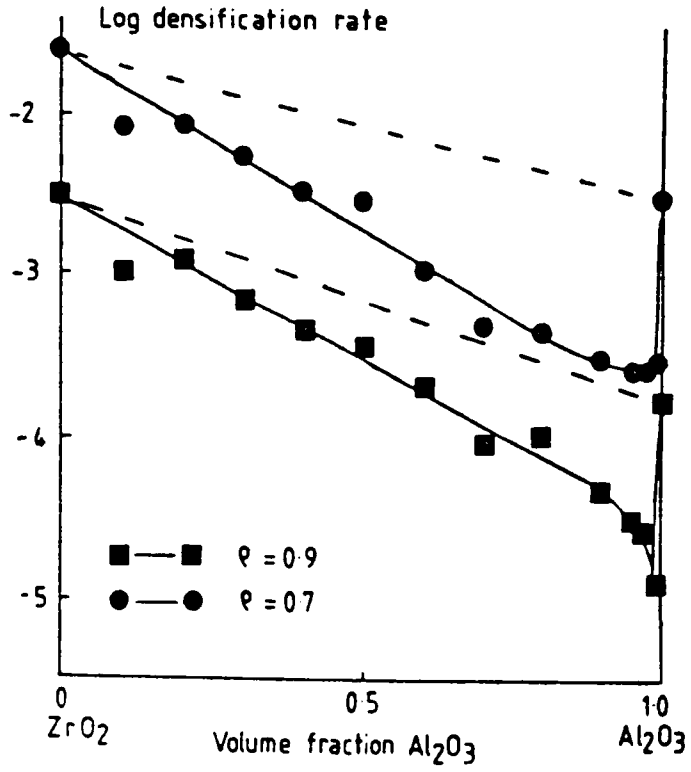
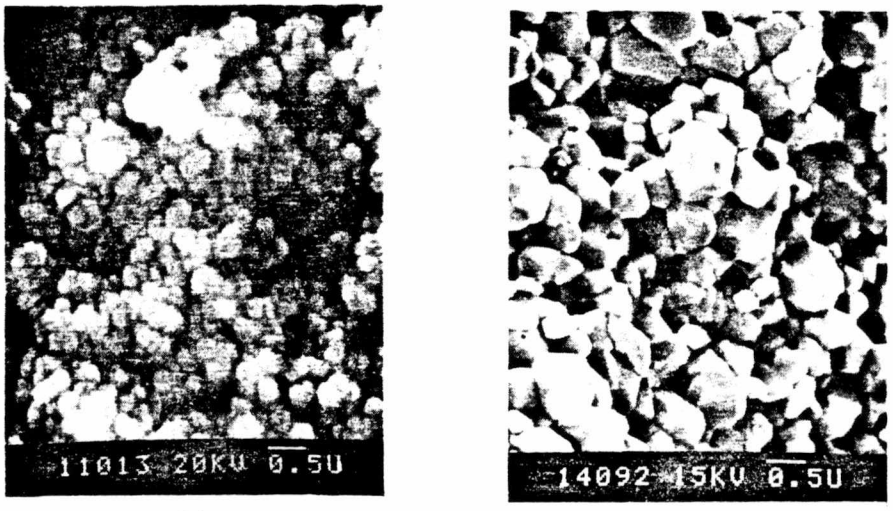


Figure 13. Densification behavior of mixtures of the two powders during hot pressing (1350 °C; 20 MPa).

Source: R. Majumdar, E. Gilbart, and R. J. Brook "Kinetics of Densification of Alumina-Zirconia," Trans. J. Brit. Ceram. Soc., Vol. 85, No. 5, p. 15-60, (1986).



(a) (b)

Figure 14. Scanning electron micrographs of the individual (a) ZrO_2 (b) Al_2O_3 materials following hot pressing.

Source: R. Majumdar, E. Gilbart, and R. J. Brook, "Kinetics of Densification of Alumina-Zirconia," Trans. J. Brit. Ceram. Soc., Vol. 85, No. 5, p. 156-60, (1986).

0.2 μm at 1400 °C, 0.5 μm at 1500 °C, and 1 μm at 1600°C and the average grain size for the single-phase end-members was approximatly 2 μm for alumina, and 0.5 μm for zirconia.

Sato (103) examined dispersing 0 to 40 wt% alumina into yittria-based tetragonal zirconia polycrystals to inhibit the tetragonal-to-monoclinic phase transformation. He concluded that the dispersion of alumina into zirconia (yittria) ceramics slowed down the rate of the tetragonal-to-monoclinic phase transformation.

Osendi (104) reported that small additions of TiO_2 could strongly affect the sintering behavior in a beneficial way, suggesting the use of TiO_2 as a sintering aid for the zirconia-alumina system. He concluded that the addition of TiO_2 increased the initial sintering rate of the composite and alumina grain size after sintering and a significant enhancing of the growth kinetics of zirconia particles with annealing treatments.

Tsukuma (105) sought to improve the high temperature mechanical properties of zirconia toughened ceramics by using a large addition of alumina and the application of isostatic hot-pressing. He reported that for ZrO_2 (2 mol% Y_2O_3) / Al_2O_3 composites, the addition of alumina up to a maximum at 20 wt% alumina resulted in enhanced strength at room temperature to 1000 °C and isostatically hot pressed composite materials exhibited extremely high strength at high temperature, but at below 400 °C, a decrease in strength, fracture toughness, and elastic modulus were found for the materials fabricated by isostatic hot-pressing.

Rajendran (106) reported that the addition of alumina to yittria-

based tetragonal zirconia polycrystals improved the attainable density of the materials after sintering at 1500 °C and reduced the degradation of their densities due to porosity formation when the materials were sintered above 1500 °C. Also he reported that a gradual decrease of grain size was observed with an increase in the alumina content and a grain-boundary pinning effect of alumina appeared to be acting in reducing the grain size and the compressive stress state within a transformed grain caused the crack to run around the grain boundary before progressing as shown in Figure 15. Thus as the alumina content in the material was increased, the stability of the tetragonal zirconia increased, the grain size decreased and the stress intensity factor decreased as shown in Figure 16.

Wakai (107) reported that the activation energy of 80 wt% ZrO_2 (3 mol% Y_2O_3) / 20 wt% Al_2O_3 composite was approximately 620 KJ/mol by plotting temperature versus stain rates and the deformation mechanism was superplasticity at above 1573 K due to grain boundary sliding between ZrO_2 and Al_2O_3.

Fukuhara (108) reported that adding TiC to the ZrO_2/Al_2O_3 composite suppressed the decrease in strength at temperatures above 1573 K because a continuous skeleton of TiC prevented grain boundary sliding between ZrO_2 and Al_2O_3. He also showed that the Al_2O_3 grain size increased as the content increased in (Y)TZP-Al_2O_3 composite as shown in Figure 17.

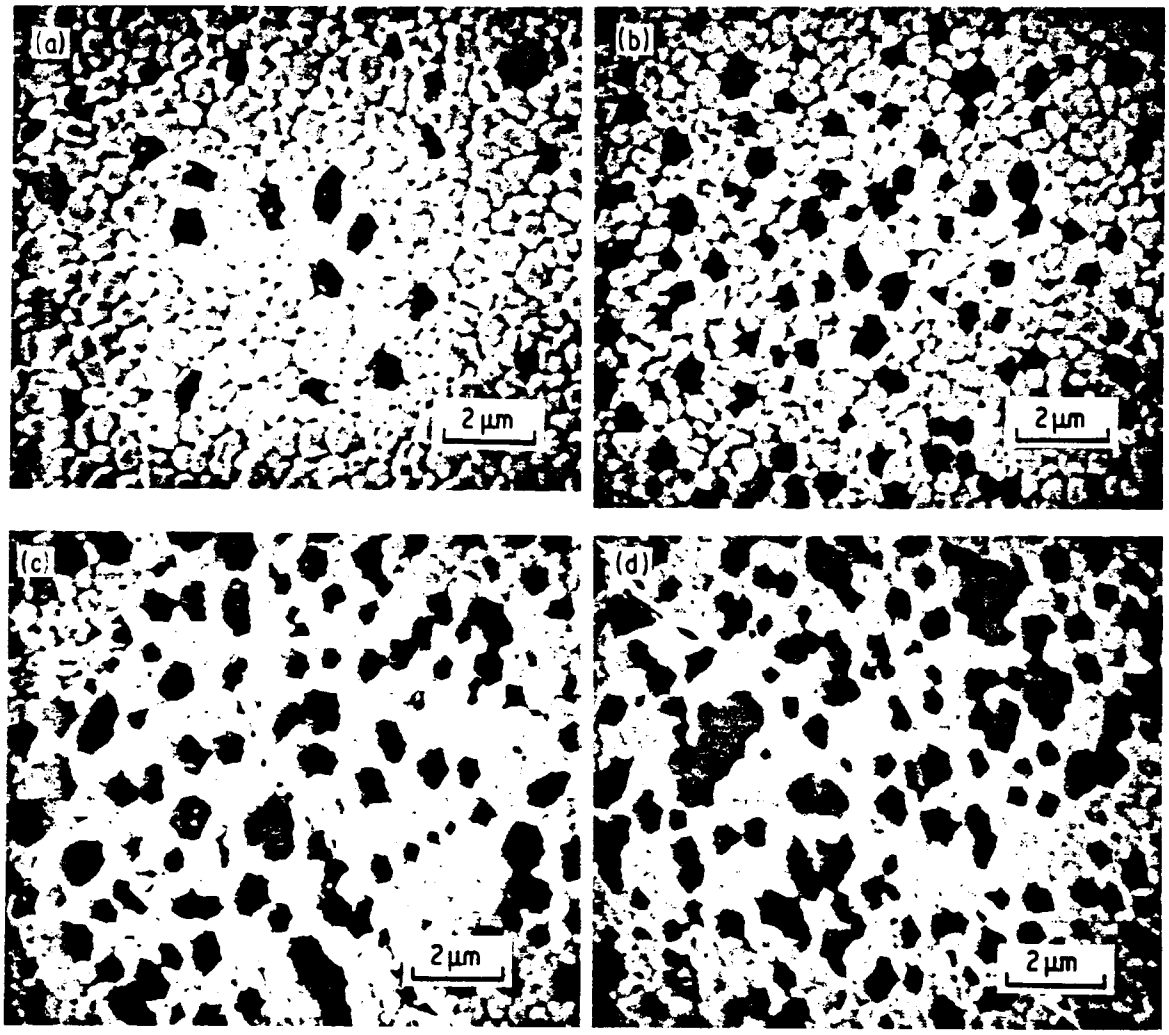


Figure 15. Scanning electron micrographs of polished and thermally etched ZYXXAl_2O_3 - 1500 °C composites, (a) ZY5Al_2O_3, (b) ZY10Al_2O_3, (c) ZY20Al_2O_3, (d) ZY 30Al_2O_3. In (c) and (d), a crack emanating from a Vickers intent can be seen.

Source: S. Rajendran, M. V. Swain, and H. J. Rossell, "Mechanical Properties and Microstructures of co-Precipitation derived Tetragonal Y_2O_3-ZrO_2-Al_2O_3 Composites," J. Mat. Sci., Vol. 23, No. 5, p. 1805-12, (1988).

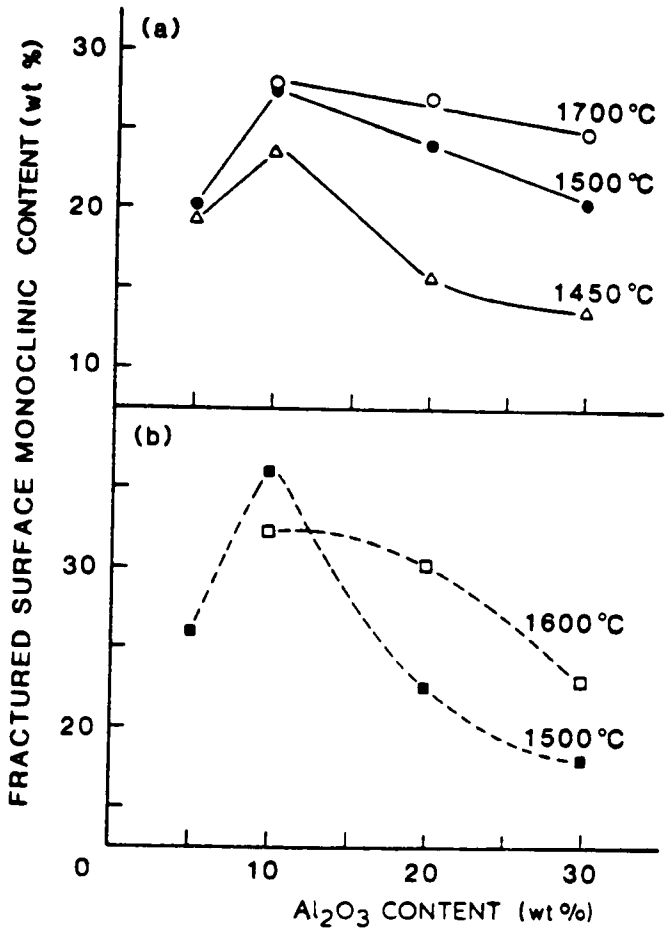


Figure 16. Changing in fractured surface monoclinic percentage with Alumina content in the materials, (a) sintered and (b) HIPed.

Source: S. Rajendran, M. V. Swain, and H. J. Rossell, "Mechanical Properties and Microstructures of co-Precipitation derived Tetragonal Y_2O_3 -ZrO_2-Al_2O_3 Composites," J. Mat. Sci., Vol. 23, No. 5, p. 1805-12, (1988).

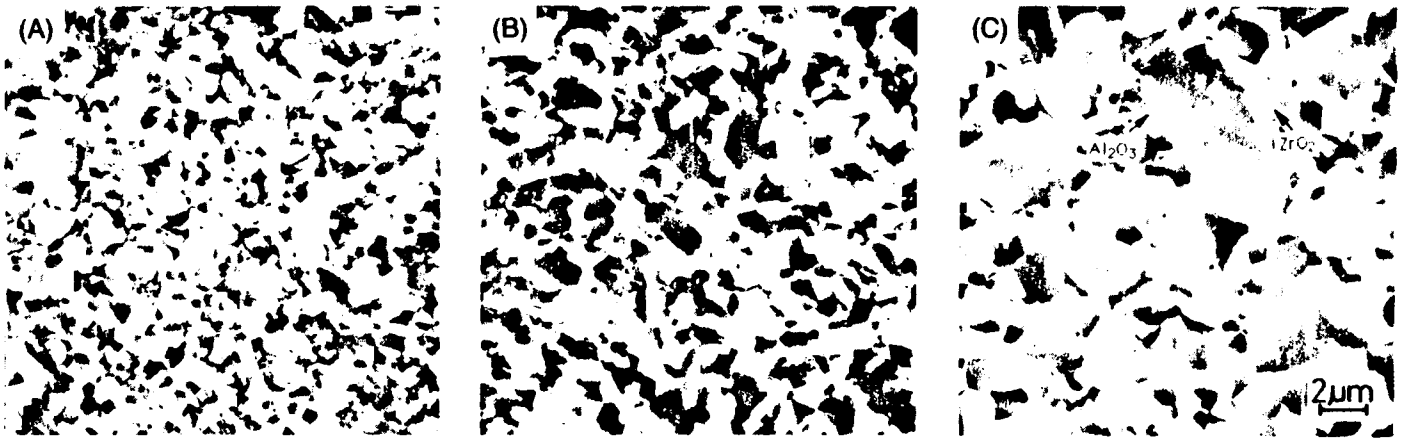


Figure 17. Photographs of fracture surface of (Y)TZP-Al_2O_3 binary ceramics: (A) 20 wt% Al_2O_3, (B) 40 wt% Al_2O_3, (C) 60 wt% Al_2O_3; white grains are zirconia and gray ones alumina.

Source: M. Fukuhara, "Properties of (Y)Y2O3-ZrO2-(Ti or Si)C Composites," J. Am. Ceram. Soc., Vol. 72, No. 2, p. 236-42, (1989).

CHAPTER III

EXPERIMENTAL METHODS

III-1. Material

The composite powder $ZrO_2(+Y_2O_3)/Al_2O_3$, Super-Z made by Toyo Soda Manufactoring Company, was used as a starting material. This composite powder was fabricated from 75.7 wt% ZrO_2 which contained 4.2 wt% Y_2O_3 in solid solution and 20 wt% Al_2O_3. The compositions and characteristics of this powder are listed in Table 1. Green samples, weighing 2.4 to 2.5 grams, of approximate diameter 1.283 cm and height 0.710 cm, were prepared by pressing uniaxially into a right circular cylinder at 230 MPa; green density was approximately 50% of theoretical. Small samples were used for experiments to reduce density variations caused by thermal gradients.

III-2. Conventional and Microwave Sintering

Conventional sintering was done on an alumina plate where small cold pressed pellets were stacked one element high. The cold pressed pellets were heated in an electric furnace for 108 hours at 1350 °C in a conventional furnace. Conventional sintering was accomplished in air at a heating rate of 50 °C/hr.

Microwave sintering was done in a Cober model S6F microwave oven. Power was supplied to the waveguide by a 6 KW variable-power microwave generator operating at 2.45 GHz. Typically, the power level was 500 W initially, which was gradually increased up to

Table 1. Chemical composition and characteristic of Super Z (3Y20A).

	TOYO SODA COMPANY	LOS ALAMOS NATIONAL LAB.
Y2O3 (mol%)	3	3
Typical Composition		
ZrO2 (wt%)	75.7	75.2
Al2O3 (wt%)	20	20
Y2O3 (wt%)	4.2	4.2
SiO2 (wt%)	-	0.01
Fe2O3 (wt%)		0.005
Na2O (wt%)		0.007
Average Particle Size (μm)	0.3	-
Specific Surface Area (m2/gr.)	15	12
Crystallite Size (Å)	200	200
Crystal Phase		
Zirconia	-	Tetragonal
Alumina	-	Alpha

3 KW at the onset of sintering, and then held constant with a little decrease during sintering to maintain temperature. Three cold pressed pellets were placed in each of seven columns. These were then located in the region of highest electric field intensity which is in the center area of the cavity which is surrounded by insulation. The green-state of a zirconia-alumina composite, although an electrically low-loss material, could be heated to sintering temperature in a current cavity. A total of 21 green samples were microwave sintered at one time. A conventional time clock with a seconds indicator was used to quantify energy transfer. No automatic controllers or recorders were readily available for this work. Consequently, all the experiments and data recordings were performed manually.

Earlier attempts to couple directly to the loosely packed powder being sintered often failed because there was too much air (low dielectric constant) for the microwave power density available. To accomplish efficient coupling of the materials to the microwaves, a fired dense zirconia plate approximately 60 mm diameter by 7 mm high (wt. = 60 grams) was used as a susceptor. The microwave susceptor (dense zirconia) initially absorbed the 2.45 GHz photons converting them to heat and enabling the samples to reach a temperature high enough that their increase in loss tangent caused them to continue heating. Hence, the zirconia-alumina composite, which was difficult to heat, could be easily heated at 2.45 GHz.

To measure the sintering temperature, a Mikron M210S Infrared-Thermometer and R-type Thermocouple were used. The

IR-Thermometer was focussed on the front edge of the specimen with a small hole in the front part of the reaction cavity. Also, the thermocouple, which was shielded by metal to prevent it from interacting with the surrounding microwave radiation, was placed near the top of the specimen with a small hole in the top part of the reaction cavity.

Two types of experiments were performed: (1) steady-state, wherein the surface temperature of the sample was maintained constant throughout the experiment; and (2) transient, wherein the available microwave power was maintained constant throughout the experiments. In the transient mode, "zero time" was marked by the instant available microwave power was switched on. The steady-state experiments were conducted based on optimum heating conditions with the zirconia-alumina composites.

The microwave generator was instrumented to indicate forward and reflected power. The difference between the two readings represented the net power into the load, and this was recorded in precise one minute intervals. In this way, a running summation of the net power data provided a cumulative energy profile with time. Additionally, since temperature was recorded every minute, this data provided the more important energy versus temperature characteristics.

III-3. Components of the Experimental System

The microwave system used was the Cober Model S6F industrial microwave system. In this system, microwave power is supplied to

the cavity through a waveguide by a 6 KW variable-power microwave generator operating at 2.45 GHz. The generator is housed in a cabinet. The complete assembly measures 163 cm high, 91 cm wide and 46 cm deep. Air, to cool the cabinet, is brought in through a heat exchanger mounted on the top of the cabinet, and a portion of the air is exhausted through the waveguide to the applicator. Two of the major components, the magnetron tube and the circulator, are directly water cooled. Included in the waveguide sections is a protective circulating water load and a single-stub tuner used to match impedance between the source and the load. The applicator is mounted to a waveguide flange such that the load is along the geometric center line of incident microwave irradiation. A multi-mode resonant cavity serves as an applicator that is coupled to the power source using WR-284 waveguide sections. The entire cavity is covered with low loss thermal insulation.

A block diagram of the microwave system used in conducting the various experiments to be described is shown in Figure 18. A detailed description of how each individual component fits into the system is presented below.

III-3-a. Microwave Generator

The microwave generator is the key element in the system. The generator is available with continuous output power ranges from 1 KW to 6 KW at 2.45 GHz.

A magnetron tube, source of the microwave power, is commonly water cooled at power levels in excess of 1 KW. The amount of

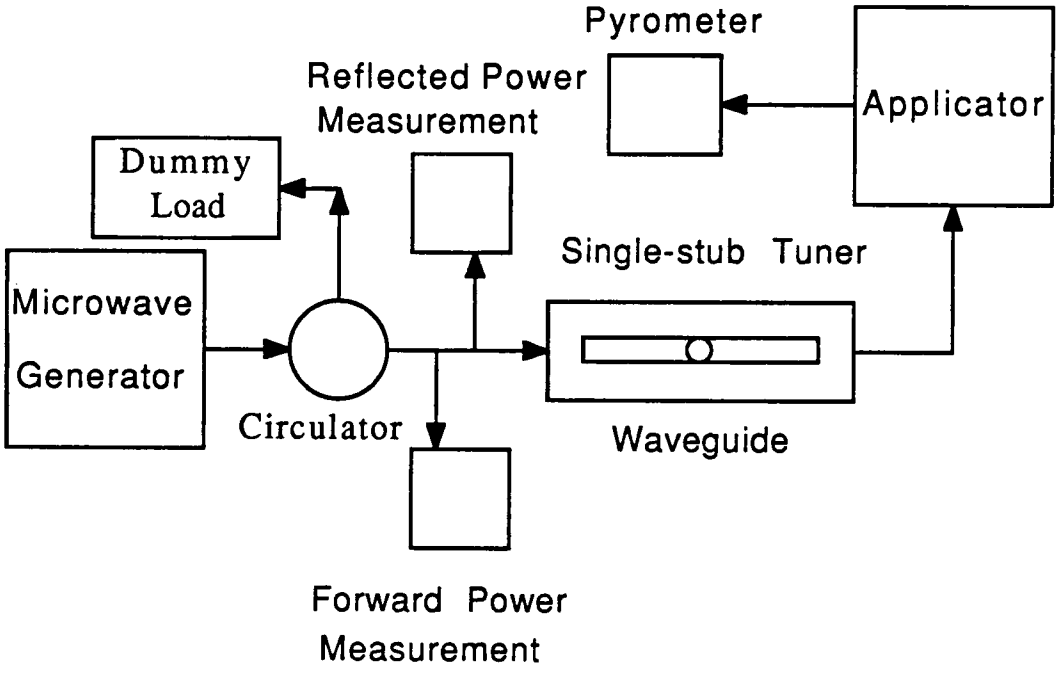


Figure 18. The experimental system.

available microwave power from the generator is varied by changing the anode current of the magnetron.

The microwave generator has a single variac power level control and a pair of meters to indicate forward and reflected power flow into and out of the waveguide. The two meters are necessary so that actual absorbed power is simply the difference between the forward power and the reflected power. Instantaneous changes in the input admittance of the applicator may be monitored by reflected power measurement. The reflected power meter is also useful in this tuning system, which is referred to as impedance matching. The optimal match is found when for any given forward power setting the reflected power is at a minimum. It also may be used for finding the position of a maximum of the reflected wave outside the applicator in the waveguide which delivers microwave power to the cavity.

III-3-b. Circulator

The generator is equipped with protective devices that will enable prolonged operation in less than optimal conditions. The circulator is left in place to take into account the small transmission losses in the circulator; thus the available microwave power is really the output power after the circulator. The common components in a microwave generator are a 3-port circulator and a dummy load. The 3-port circulator is a tube protection device that prohibits reflected microwave energy from reaching and possibly damaging the magnetron tube. The circulator diverts the reflected microwave

energy from the applicator to its third port where a dummy load is mounted. The dummy load, being connected to the third port circulator, is normally a water load in higher power configurations. As a consequence, the magnetron in the microwave generator is protected from possible damage that follows after an excessive feedback of microwave energy from the load.

III-3-c. Waveguide

The waveguide in a microwave system is simply used as a conduit for the transmission of the microwave energy from the source to the applicator. A detailed diagram of the waveguide is shown in Figure 19. This waveguide is a WR-284 brass waveguide that guides the incident microwave energy. The waveguide may be configured with any assortment of straight sections and bends.

The most important waveguide component is the tuning section. The single-stub tuner is the device that is used to impedance match the load to the source. The single-stub tuner helps to minimize the amount of net reflection of microwave power by the whole applicator structure when it is positioned properly. Therefore, the load can be placed in a high-electric field intensity region.

III-3-d. Applicator

The applicator used is a multi-mode resonant cavity which is the most common applicator in a microwave system. As shown in Figure 19, the cavity is a box made from stainless steel that has been seam welded to prevent arcing. The internal dimensions of the stainless-steel cavity are multiples of a half wavelength of the 2.45 GHz

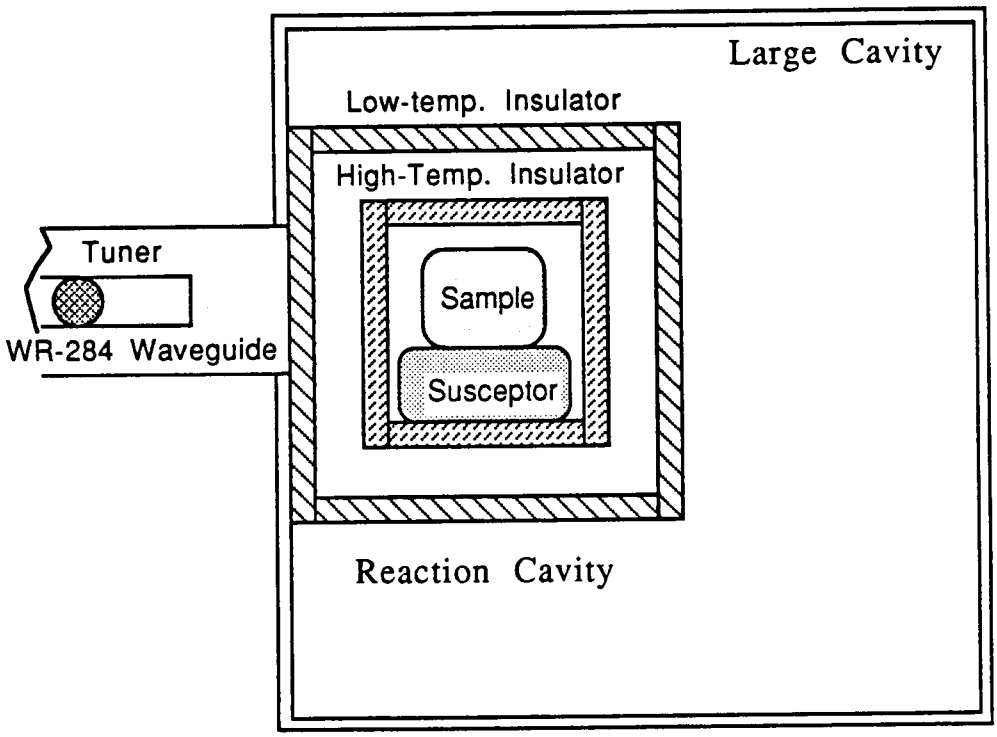


Figure 19. Schematic diagram of cavity configuration required for microwave heating of low-loss loads to very high-temp., e.g., zirconia-alumina composite to 1400 °C or 1800 °C.

microwave frequency (24" wide, 25.5" deep and 27" high) to heat large irregular samples uniformly. The power density in the cavity is made uniform by allowing the microwave energy to reflect on and off of the cavity walls many times, thus exciting a very large number of cavity modes. The reaction cavity (9.5" wide, 9.5" deep and 9.75" high) inside the metal shielded cavity has an area 54 cm^3 surrounded by Babcock-Wilcox 17C alumina insulation, which serves as a heat shield, and is located at the area of the highest electric field intensity. The interior of the reaction cavity surrounded by low-temperature insulation is constructed of a layer of 1 inch thick high-temperature insulation rated to withstand 3000 °F. Both insulations are basically high purity alumina and have superior physical strength.

The insulation, transparent to microwaves but opaque to infrared radiation, forms an infrared cavity to trap whatever heat energy the load converts from the microwave irradiation. In practice, some heat is conducted through the less than perfect insulation and is lost as radiation to the ambient environment. The door on the cavity has an absorbent material to prevent microwave leakage. The absorbent material used is "ECOSORB", which is a ferrite filled rubber composition.

III-3-e. Pyrometer

Measurement of the instantaneous surface temperature of the sample was made by an optical pyrometer that utilizes a semiconductor sensing element. Steady-state surface temperature

was also measured. Knowdge of the emissivity of the surface was required for accurate measurement.

The infrared pyrometer used was the Mikron model 210S. The manufacturer's manual states that its accuracy is within 1.0% up to 2000 °C. It has an emittance knob which should be set to the value of the emissivity of the surface for accurate readings. The silicon photovoltaic detector that senses the thermal radiation from the surface being measured has a band-pass; radiation between the wavelengths 0.6 micrometer and 1.0 micrometer are the only ones actually detected. In this case in general the emissivity varies with wavelength.

However, the usefulness of the Mikron pyrometer is in measuring instantaneous changings in temperature making it a suitable component for the surface temperature feedback control system. The setting of the emittance knob on the Mikron pyrometer is not important when the instrument is part of the control system. This is because the objective of the system is to maintain the relative surface temperature constant at a desired value. Since only the relative value and not the absolute value of temperature was important, the emittance knob was usually set to the value of 1.0.

The samples were always mounted at the center of the cavity in all the experiments. This means that the expected temperature profile is symmetrical about the axis along the X-direction, i.e., across the width of the cavity.

III-4. Measurement of Density and Porosity (55)

The bulk density of porous bodies requires a determination of the total volume of solid plus pores. Therefore, for green samples bulk density was determined by measuring the sample dimensions with a micrometer and then calculating its volume.

For sintered samples bulk density was determined by first weighing a sample in air "W_a" and then heating in boiling water for 2 hours to fill the open pores completely with water. After cooling, the weight of the saturated piece "W_w" was determined. The difference between these two values gave the sample volume and allows calculation of the bulk density as below;

$$D_b = \frac{(W_a D_w - W_w D_a)}{(W_a - W_w)} \qquad \text{(III-1)}$$

where D_b is the bulk density, D_a is the density of air, and D_w is the density of water. At 25 °C, D_a = 0.00112 and D_w = 0.99705 (109).

The total porosity F_p was also measured by determining the bulk density D_b of the sample and comparing this with the theoretical density D_t as below;

$$F_p = 1 - D_b / D_t \qquad \text{(III-2)}$$

III-5. Thermal-Shock Test

The thermal-shock resistance of the sample was obtained by measuring the fracture toughness or compressive strength of the thermally shocked specimens. This test was performed to ascertain the performance of the various specimens during a severe

temperature change of from 300 °C to 900 °C. The apparatus used for thermal shock consisted of a cylindrical tube furnace mounted in a vertical position above a large container of boiling water. The specimens were slowly lowered into the hot zone of the furnace in a wire hanger so as to avoid thermal shock. The samples were given 15 minutes to equilibriate to the furnace temperature and then were allowed to fall freely into the boiling water by cutting the wire hanger. The furnace temperature was controlled through a thermocouple placed at a position near the sample. The severity of the thermal shock was changed by adjusting the temperature of the furnace. The compressive strength of the specimens was measured after they had been air dried for at least one day.

A boiling water quench bath was used because of several attractive features such as temperature maintenance, turbulent heat-transfer conditions, and less variable surface heat-transfer coefficients compared to quenching into room-temperature water (110).

III-6. Microstructure Analysis

Microstructure analysis was done by the direct examination of the samples with the AMR 900 Scanning Electron Microscope (SEM) (111). The surfaces of samples were prepared by polishing on successively finer emery SiC paper starting with 120 grit and ending with 600 grit. Coarse polishing was accomplished using 3 and 6 micron diamond pastes. Final polishing was done with 1 micron diamond paste on 1 micron cloth. The polished samples were

thermally etched for 5 and 8 hours at 1050 °C to reveal the grain boundaries. To prevent charging during examination and to improve resolution at high magnifications, the thermally etched specimens were coated with gold to produce a surface layer approximately 200 Å thick.

The average grain size of the polished and thermally etched surface was determined by the linear intercept method; measuring an average linear intercept distance on the scanning electron micrograph of the polished and thermally etched surface, and then multiplying this by 1.558 (112). The fracture surface of the specimen was only coated with gold, and then examined on the scanning electron microscope. Experience revealed that the best micrographs were obtained when the polished surface of the specimen was given a relatively heavy thermal etch and viewed with the specimen tilted about 30 degrees towards the detector.

The composition of the specimen contents was determined by Energy Dispersive X-ray Analyzer (EDXA). Although the specimens for analysis were coated with carbon to eliminate the difficulties arising from the use of X-ray absorbing coating, gold coated specimens were used.

III-7. XRD Techniques

A Rigaku X-ray diffractometer in reflection mode was used for analyzing the phases present. This diffractometer system is interfaced with a PDP 11/34 computer, which has its own microprocessor. The microprocessor can be programmed to give the

desired conditions for an X-ray scan. These conditions include a step scan or continuous scan, axis of rotation, number of cycles, starting and stopping angle, scan speed, time constant and chart speed. The peak information can be stored in the computer or recorded on chart paper. The X-ray source was copper Kα, and was operated at 35 kV and 20 mA. A typical user program is shown in Table 2.

Bulk samples were used although these had peak broadening effects which caused overlap between adjacent monoclinic and tetragonal diffraction peaks. The reason was that pulverizing bulk samples was very difficult and caused phase transformation by stressing the particles. Phase analysis was determined with Cu Kα radiation using the method of Garive (113). His method is used with the help of the following assumptions; 1) the linear absorption coefficient is the same for the monoclinic and cubic/tetragonal phases, 2) the diffracted intensity per unit volume is the same for the monoclinic (111 and 111 reflections combined) and the cubic/tetragonal (111) reflections, 3) Sin θ is the same for all reflections, and 4) the only monoclinic material found is within the transformed zone and is formed by the crack from precipitates which were originally tetragonal.

According to these assumptions, the fraction of the monoclinic zirconia phase was determined by measuring the intensities of the monoclinic and tetragonal diffraction peaks as below;

$$X = \frac{I_m(111) + I_m(11\bar{1})}{I_m(111) + I_m(11\bar{1}) + I_t(111)} \qquad \text{(III-3)}$$

Table 2. The desired conditions for an X-ray scan.

Item	Condition 1	Condition 2
Mode	Constant Scan	Constant Scan
Cycle	1 cycle	1 cycle
Drive Axis	2Θ/Θ	2Θ/Θ
Start Angle (Degree)	10	26
Stop Angle (Degree)	110	34
Scan Speed (Degree/Min.)	1	0.5
Count Rate x 10 (CPS)	1x1K	1x1K
Time Constant (Sec.)	0.2	0.2
Chart Speed (mm/Min.)	20	20

where $I_m(hkl)$ and $I_t(hkl)$ are the integral intensities of the (hkl) peaks of the monoclinic and the tetragonal phase. Integration of the area under these peaks was achieved by outlining the peaks in tracing paper, cutting them out and weighing them on a microbalance.

III-8. Compression Test

Compression testing was carried out uniaxially in air by using an Instron Universal Testing Instrument Model 1125. This instrument incorporates a highly sensitive electronic load weighing system with load cells that use strain gauges for detecting compressive loads.

A specimen was physically table-mounted for compression testing. Compressive forces were applied by a moving crosshead operated by two vertical lead screws. The crosshead speed was 0.02 inch/min. Compressive testing results were presented on a strip chart recorder.

CHAPTER IV

RESULTS AND DISCUSSION

IV-1. The Effect of Microwave Power

This experiment was an investigation of the effect of microwave power on the heating rates of the material. The relative occurrence in time of various power levels and the surface temperature of the sample was investigated by operating the control system in the manual mode. The output of the IR meter was recorded to monitor the instaneous surface temperature. Zero time was marked by the instant the microwave generator was turn on. Before any tests were started, the single-stub tuner with forward and reflected power measurements was controlled to match the impedance between the source and the load to maximize heating. Samples were tested at 0.5 KW increments ranging from 0.5 KW to 2.0 KW. However, the tests were stopped when the insulation coupled and began to heat or arcing occurred or when the surface temperature stabilized or decreased. Sample heating data for a given power input from the microwave generator were collected with incremental increases in power and no incremental increases in power between experiments.

The effect of microwave input power on the heating rates of the samples is shown in Table 3. The surface temperatures indicated are the maximum obtained and the time is the interval to attain maximum temperature from ambient temperature. Figures 20 and 21 are plots of the corresponding surface temperatures versus time at 0.5, 1.0, 1.5, and 2.0 KW. These compare two cases with additional

Table 3. Effect of microwave input power on the heating rates of materials

Input Power	No Adjustment of the Tuner		Adjustment of the Tuner	
(KW)	Surface Temp. (°C)	Time (Sec.)	Surface Temp. (°C)	Time (Sec.)
0.5	848	240	962	120
1	986	200	1032	240
1.5	1019	120	1090	210
2	1113	80	1208	120

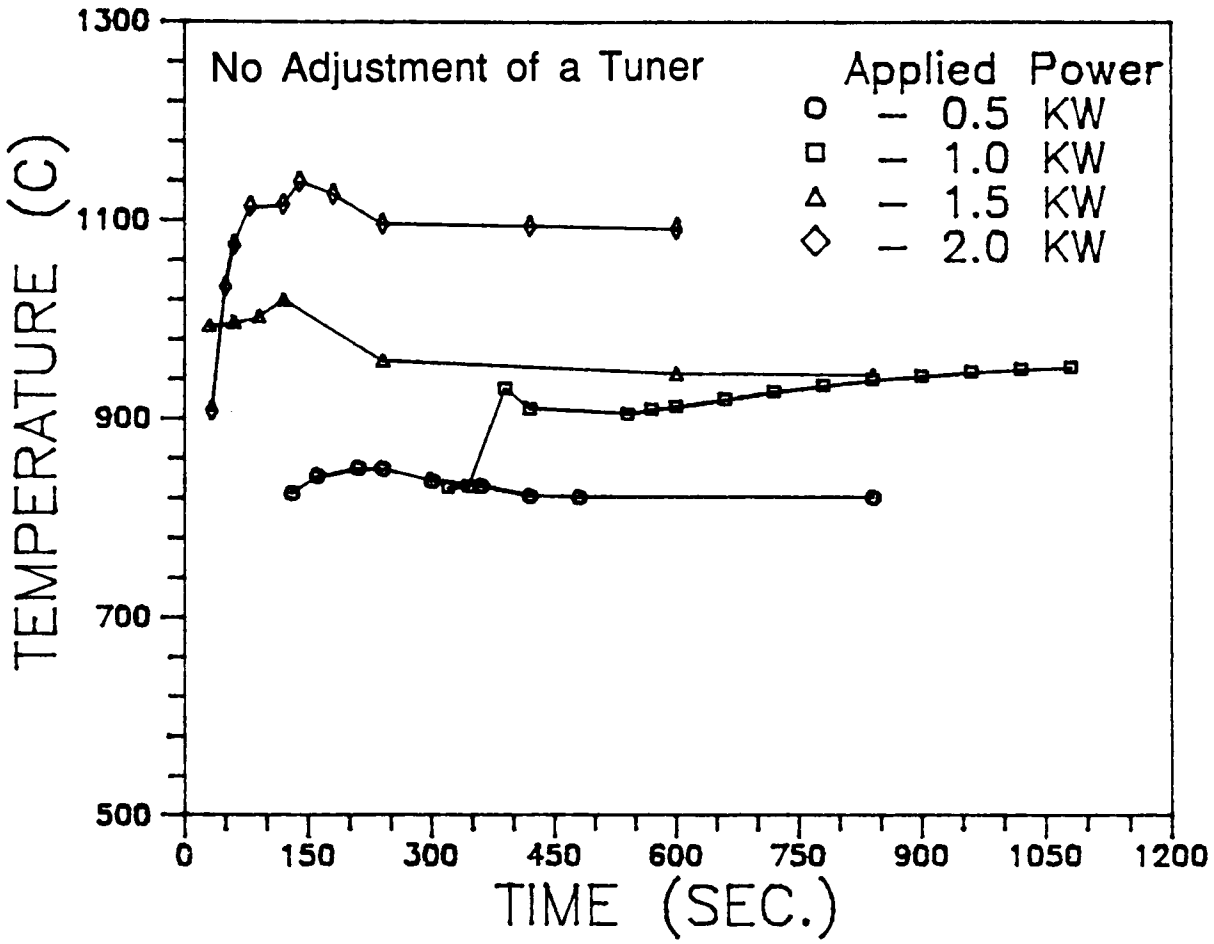


Figure 20. Temperature profile of microwave sintered samples on the susceptor at various applied power with no adjustment of the single-stub tuner.

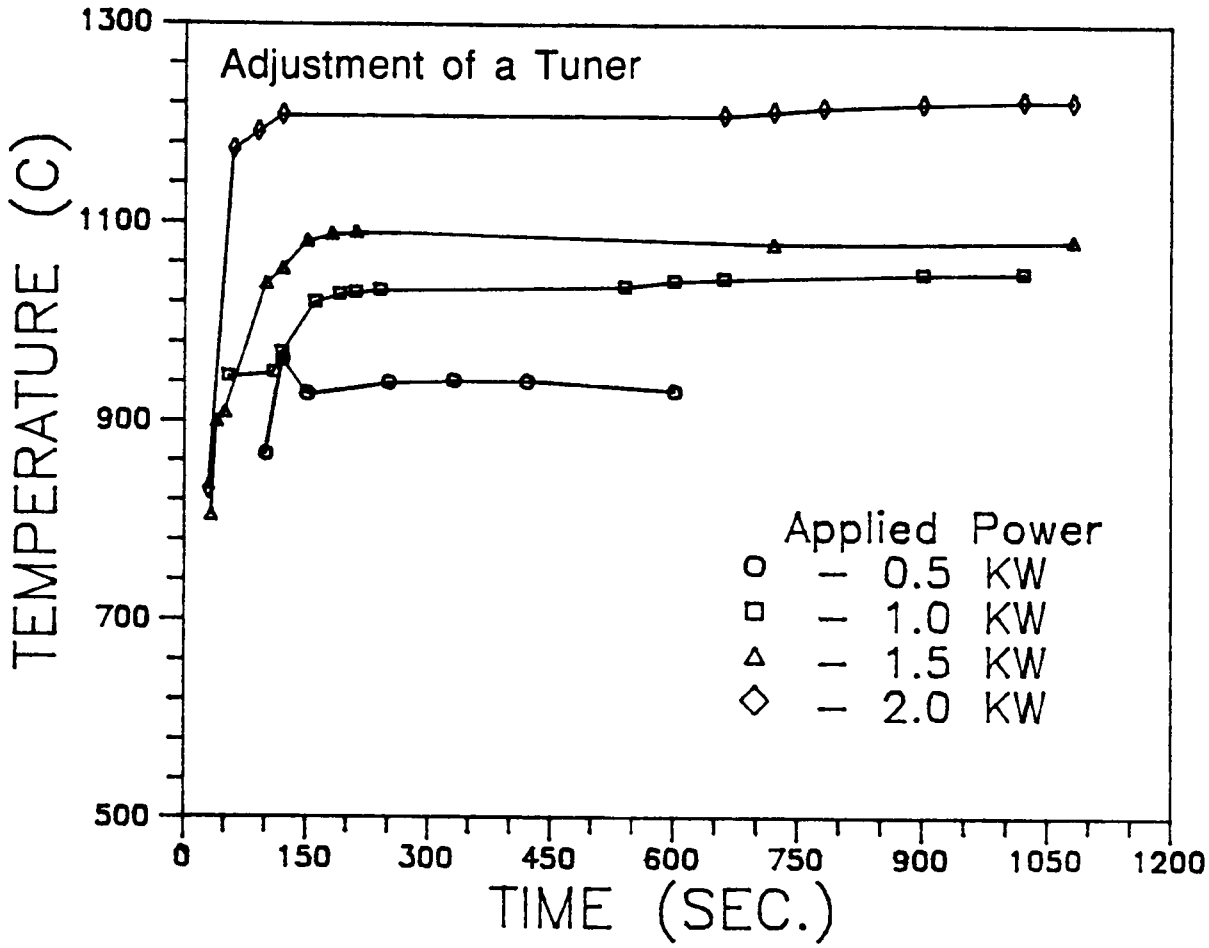


Figure 21. Temperature profile of microwave sintered samples on the susceptor at various applied power with adjustment of the single-stub tuner.

tuning and no additional tuning during experiments. The adjustment of the single-stub tuner causes the load to be matched better to the source (in this case the magnetron) which results in optimum sample heating.

All of samples tested showed an increase in heating rates as input power increased. This means that the surface temperature increase is due to the increase in the sample power density and the dielectric loss of the zirconia-alumina composite. Each of these samples in both cases attained a different maximum temperature dependent on the input power. Both cases demonstrated good coupling to the microwave radiation and reached temperatures in excess of 800 °C in a few minutes. The reason was that the zirconia-alumina composite and dense zirconia presented a load impedance which best matched the output impedance of the 2.45 GHz magnetron.

These data show that microwave input power does have an effect on the heating rates of materials. In equation II-10, the power absorbed is proportional to the square of the electric field intensity in the material. McGill (114) reported that generally heating rates increased as input power increased. Exceptions to this were some very high-loss and very low-loss materials that showed negligible changes with increased power.

A decrease of sample temperature in Figure 20 was indicative of some other material becoming a microwave absorber resulting in melted insulation as an impedance mismatch occurred between the sample and the IR insulation.

The microwave net power at various input powers are increased in Figure 22 and decreased in Figure 23. This means that the reflected power is increased with temperature for the condition of no additional tuning during the test. Once samples are microwave heated, the dielectric constant and the loss factor increase. Then the resonant frequency becomes lower and the degree of coupling decreases. Therefore, it is necessary to move the single-stub tuner so that the cavity comes into resonance and the degree of coupling approaches the critical coupling. This tuner gives rise to the resonant frequency shift, and therefore the interactive control of the tuner is necessary. This type of heating information may be used to select the proper input power for microwave heating.

IV-2. Microwave Sintering

The heating of all of the zirconia-alumina composite samples listed in Table 4 is divided into two groups: One is heated with no susceptor and the other is heated with a susceptor. The heating of both may be described as a three-step process, namely 1) preheating, 2) transition, and 3) stable sintering.

In the preheating step, initially 2.45 GHz microwave radiation couples with the insulation material (zirconia fiber insulation) until the samples reach a temperature between 700 and 1100 °C because of the low-dielectric loss in these temperature ranges. However, in the case of the heating of the sample with a susceptor, the difference is initially coupling with the susceptor (dense zirconia) instead of the insulation material.

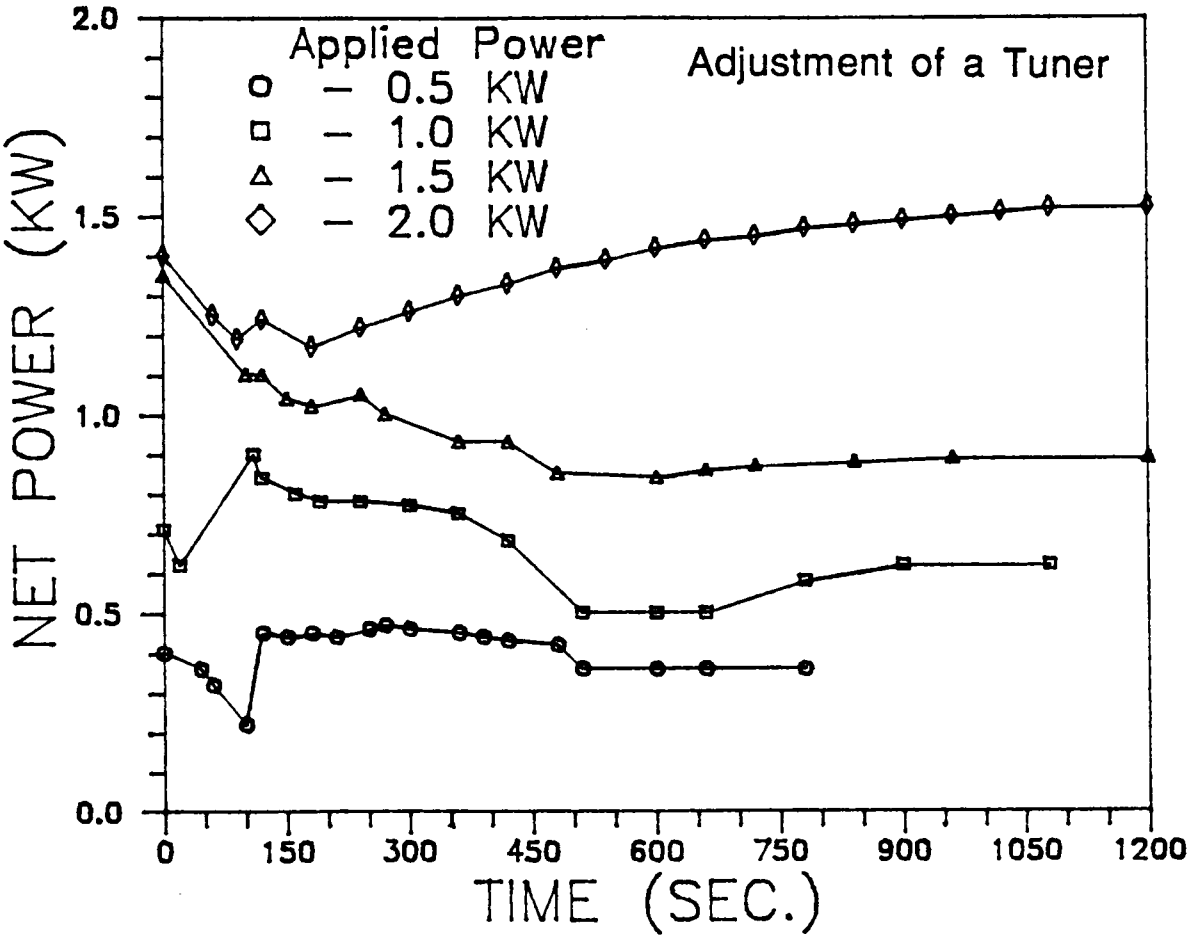


Figure 22. Net power profile at various constant applied power with adjustment of the single-stub tuner. (net power = applied power - reflected power).

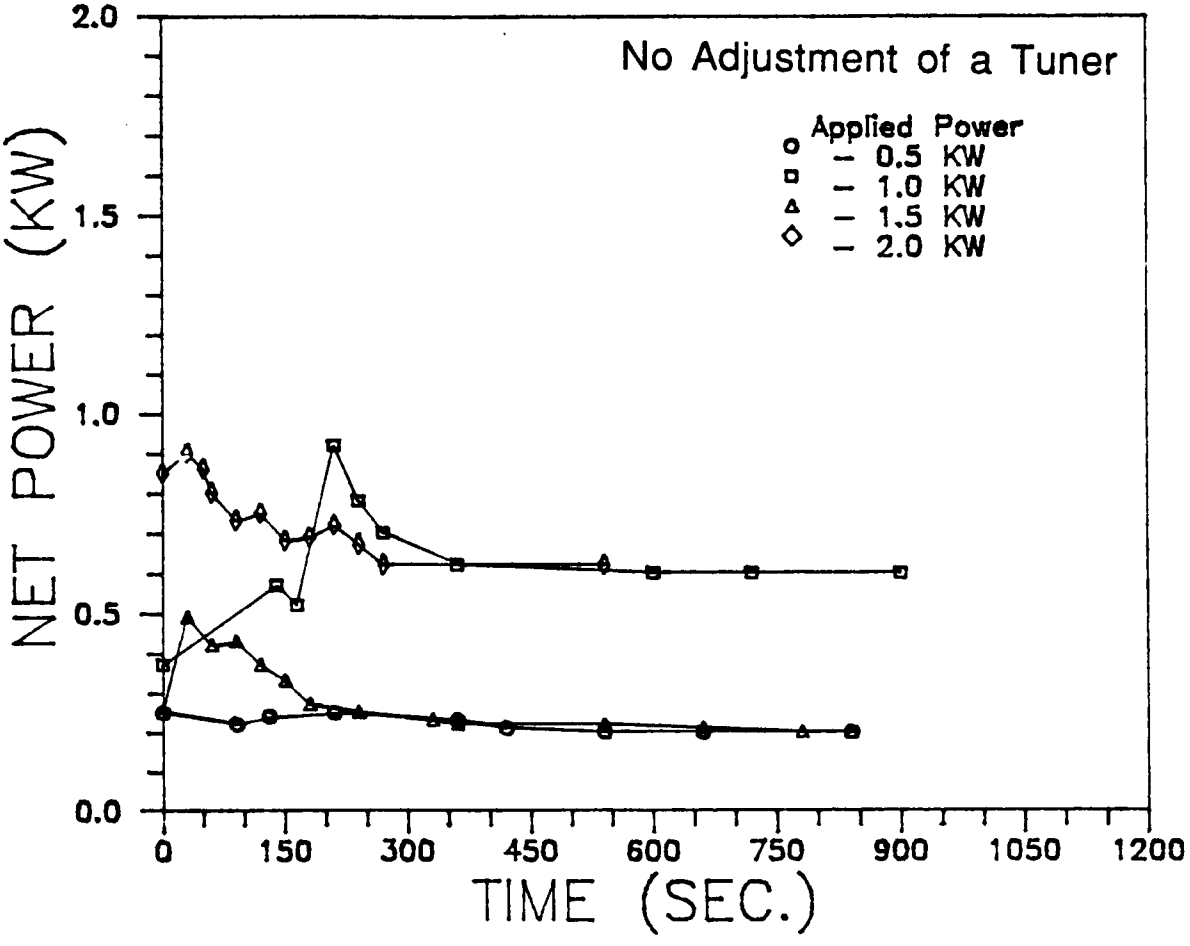


Figure 23. Net power profile at various constant applied power with no adjustment of the single-stub tuner. (net power = applied power - reflected power).

Table 4. Data on microwave sintering of zirconia-alumina composites derived from 30 runs.

Run number	Quantity of Sample	Susceptor	Max. Temp. Reached (°C)	Coupling Time (min.)	Sintering Temp. (°C)	Sintering Time (Min.)	Max. Applied Power (KW)	Heating Rate (°C/Min.)	Cooling Rate (°C/Min.)	Densification (%)	Remark
1	3	w/o	1800	83	1800	45	3	30	161	99	
2	5	w/o	1374	105	-	-	4	-	-	97	
3	3	w/o	1800	21	-	-	3.5	52	-	99	new insulator
4	4	w/o	1800	89	1800	45	4	114	194	(severe crack)	
5	6	w/o	1746	36	-	-	4.2	237	-	(severe crack)	
6	3	w/o	1306	92	-	-	4.5	-	-	97 (crack)	
7	3	w/o	1800	17	1800	45	2	107	119	97	new insulator
8	3	w/o	1454	20	-	-	3	-	-	-	
9	3	w/o	1800	95	1800	45	3	121	146	96 (crack)	
10	3	w/o	1800	17	1800	45	3	42	186	97 (crack)	new insulator
11	3	w/o	1800	109	1800	45	4	37	164	96 (crack)	
12	3	w/o	1800	41	1800	45	3.5	50	164	97 (crack)	
13	3	w/o	1800	33	1800	45	3.5	80	178	97	
14	3	w/o	1800	20	1800	45	3.5	49	178	97	
15	3	w/o	1800	20	1800	45	3	81	164	97 (crack)	

Run number	Quantity of Sample	Susceptor	Max. Temp. Reached (°C)	Coupling Time (min.)	Sintering Temp. (°C)	Sintering Time (Min.)	Max. Applied Power (KW)	Heating Rate (°C/Min.)	Cooling Rate (°C/Min.)	Densification (%)	Remark
16	3	w/o	1800	20	1800	45	3	74	164	97	new insulator
17	5	w/o	1800	41	1800	45	3.2	48	163	99	
18	3	w/o	1800	28	1800	45	3	109	160	98	
19	4	w/o	1800	27	1800	45	3.8	30	177	100	
20	6	w/o	1800	19	1800	45	3	62	160	100	new insulator
21	3	w/o	1800	40	1800	45	3.8	75	157	98 (crack)	
22	3	w/o	1800	32	1800	45	3.5	151	164	98 (crack)	
23	3	w	1400	4.5	1400	30	2	23	161	99	
24	12	w	1400	4.8	1400	30	3	19	98	100	
25	21	w	1400	3.3	1400	30	2.2	24	83	100	new insulator
26	21	w	1400	2.7	1400	30	2.4	19	73	100	
27	21	w	1400	2.8	1400	30	1.6	22	91	100	
28	8	w	1400	15	1400	30	3.4	28	89	99 (crack)	
29	6	w	1400	13.7	1400	45	1.8	62	-	(severe crack)	
30	6	w	1400	18.9	1400	45	1.3	44	84	(severe crack)	

In the transition step, after the samples heat to between 700 and 1100 °C, the samples begin to couple efficiently. Most ceramic materials couple readily to 2.45 GHz radiation above 1000 °C and in these temperature ranges samples are heated to the sintering temperature and the zirconia insulation couples much less and efficiently insulates the samples as shown by Meek (23,26). At these temperatures the samples will begin to exhibit high-frequency relaxation mechanisms which will contribute to its loss mechanisms, such as ion migration losses, molecular vibration losses, and electronic polarization losses. The major factor affecting the heating of ceramic materials is the ion migration losses which tend to increase at 2.45 GHz frequency as the temperature is raised. Conduction losses have typically been found to predominate at high temperature due to the exponential increase in electrical conductivity with elevated temperature (5,11,52,53). At this point the temperature of the samples will begin to increase rapidly.

Above 1000 °C the heating rate is markedly accelerated at constant power, and thermal runaway will occur unless careful control of input power is exercised. This is accomplished by manually decreasing the power level. Also, the input power may be adjusted to keep the heating rate at a desired value.

Decreasing the power gradually prevents thermal runaway in the zirconia-alumina composite materials. This approach is based on work done by Roussy (115). He showed that thermal runaway in a granular material was directly related to temperature dependence of the material's dielectric loss. Most materials, including the zirconia-

alumina composite studied, have dielectric loss factors which increase with temperature. The increase in losses proceeds gradually until a critical temperature is reached where the loss factor increases rapidly with temperature. It was postulated that this critical temperature in the zirconia-alumina composite was about 700 to 1100 °C.

In the stable sintering step, in a few minutes uniformly heated samples are formed, and thermal runaway becomes much easier to control. Stable sintering temperatures up to 1800 °C can be maintained by applying constant power at from 2.0 to 2.5 KW. Above 1800 °C thermal runaway will again occur, initiated by melting of the interior of the material.

As shown in Table 4, 22 runs were made with no susceptor. The first eight runs were conservative attempts and half of the runs failed to reach the sintering temperature for reasons such as equipment failure, inadequate matching, insulation red-heated, arcing, and fear of thermal damage to the equipment. Nontheless, sintering was already evident in these runs by from 97 to 99 % of the theoretical density. Although samples were considered to be microwave transparent at room temperature, the degree of microwave coupling was dependent on the temperature of the samples if these had been heated.

From run 9 to run 22, sample heating was done by carefully controlling the input power until the sintering temperature was achieved. A constant power input of 0.5 KW was applied for the first five minutes and 0.5 KW increaments of the input power was

additionally applied for every 5 minutes up to 3.5 KW input power until the samples were coupled. After coupling, the input power was instantaneously decreased approximately 2.0 to 2.5 KW to control the desired heating rate and to prevent thermal runaway. After maintaining the stable temperature, the input power was gradually increased to reach the sintering temperature. After reaching the sintering temperature, the input power was gradually decreased to maintain the sintering temperature. Optimal coupling were achieved by adjustment of a single-stub tuner to provide minimum reflection, as indicated on the reflected power meter. Surface temperature was measured by the IR-meter focussed through the hole in the cavity wall onto the sample surface and controlled by varing input power.

Figure 24 shows a plot of sintering time versus sample surface temperature. Figures 25-28 are plots of sintering time versus power (input power, reflected power, and net power). In these runs, it was observed that some samples were cracked by the ultra-high heating rate as a result of control difficulty and the bottom of some samples were partially melted by localized high temperature due to thermal runaway. A noticeable phenomenon was the change of absorption properties with increasing temperature. In the beginning of the heating stage, the percent power reflected was high and the sample power absorption unstable because of mismatching of the load.

Eight runs were made with a zirconia susceptor. A constant power input of 0.5 KW was applied for the first several minutes until the samples were coupled. After coupling, the input power was gradually increased to reach the sintering temperature. Just below

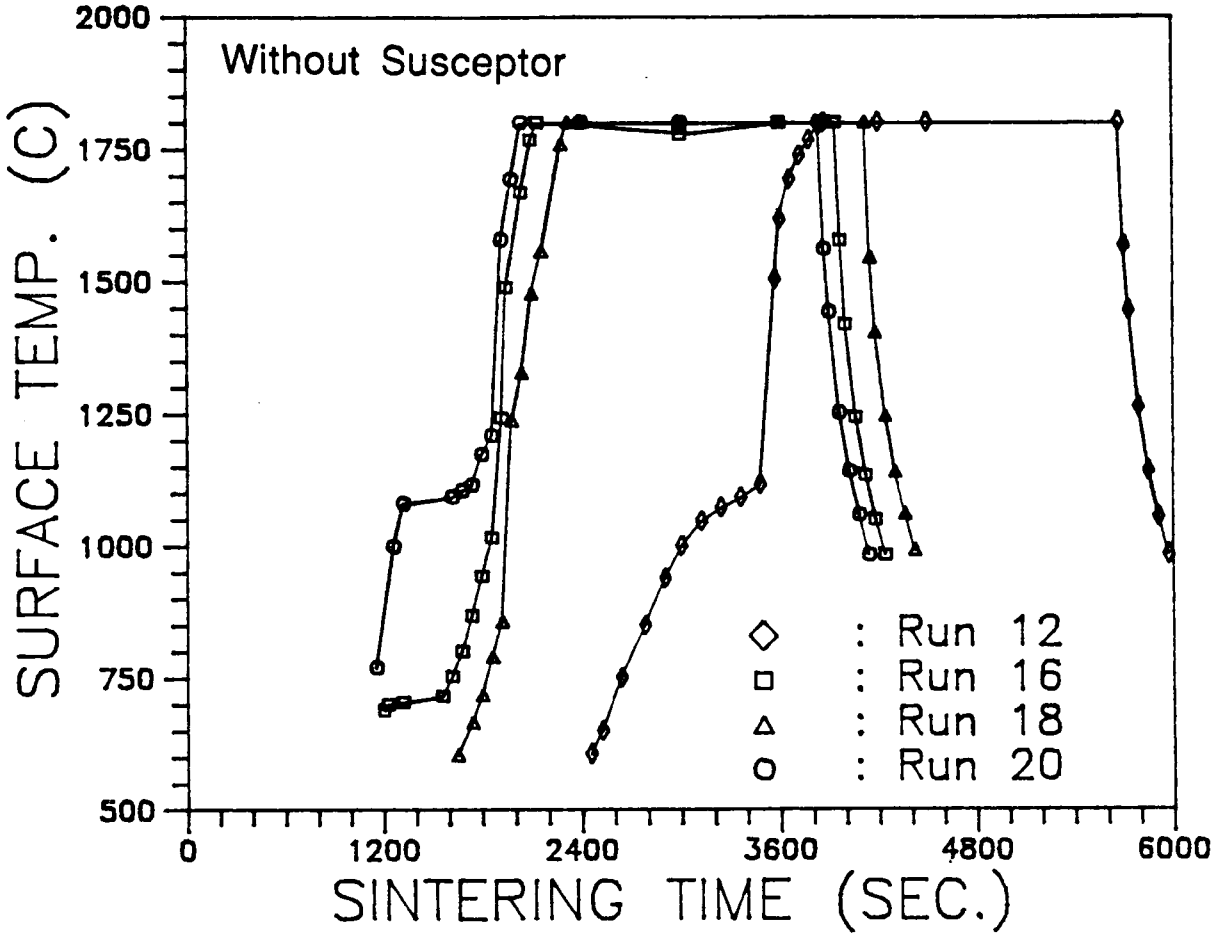


Figure 24. Temperature profile of microwave sintered sample without susceptor.

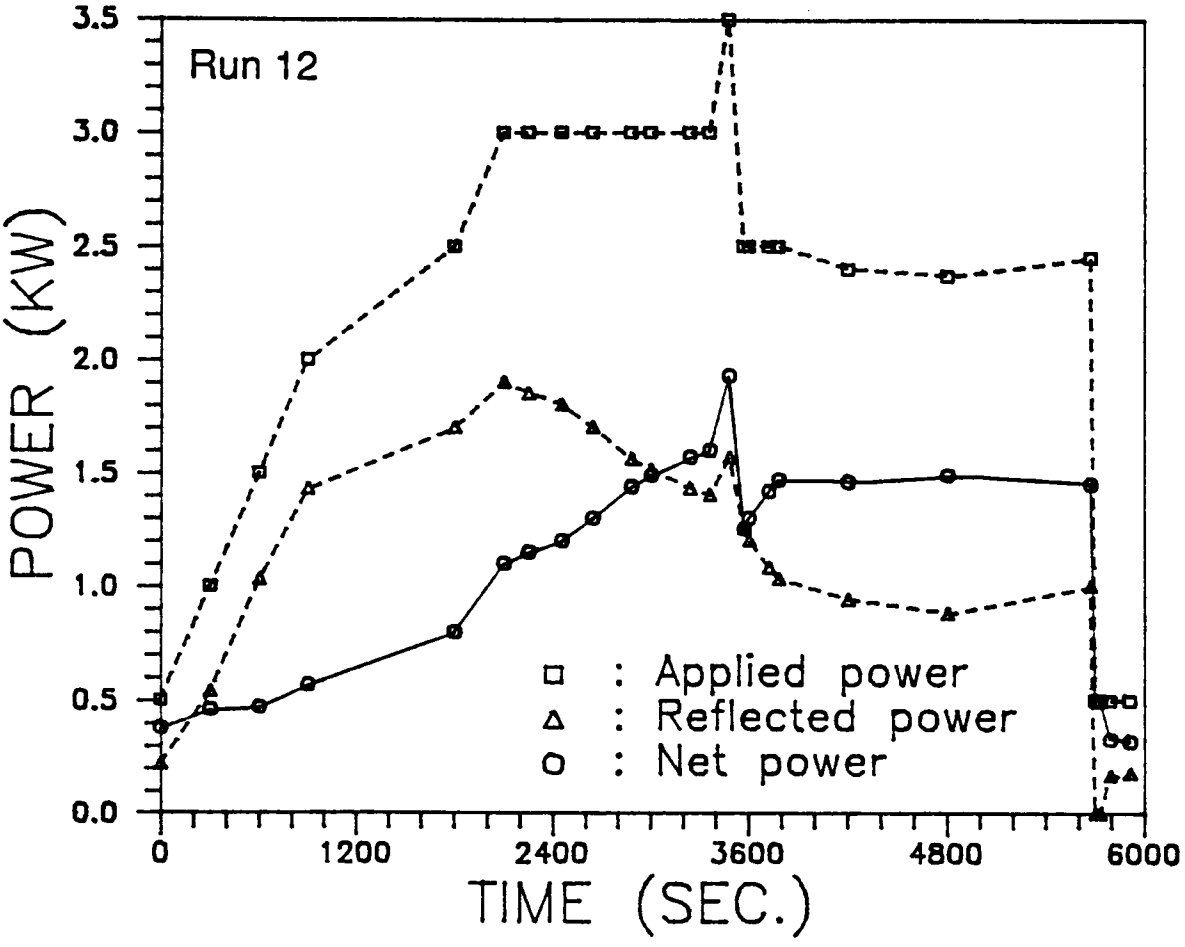


Figure 25. Power distribution in run 12 microwave sintering without susceptor.

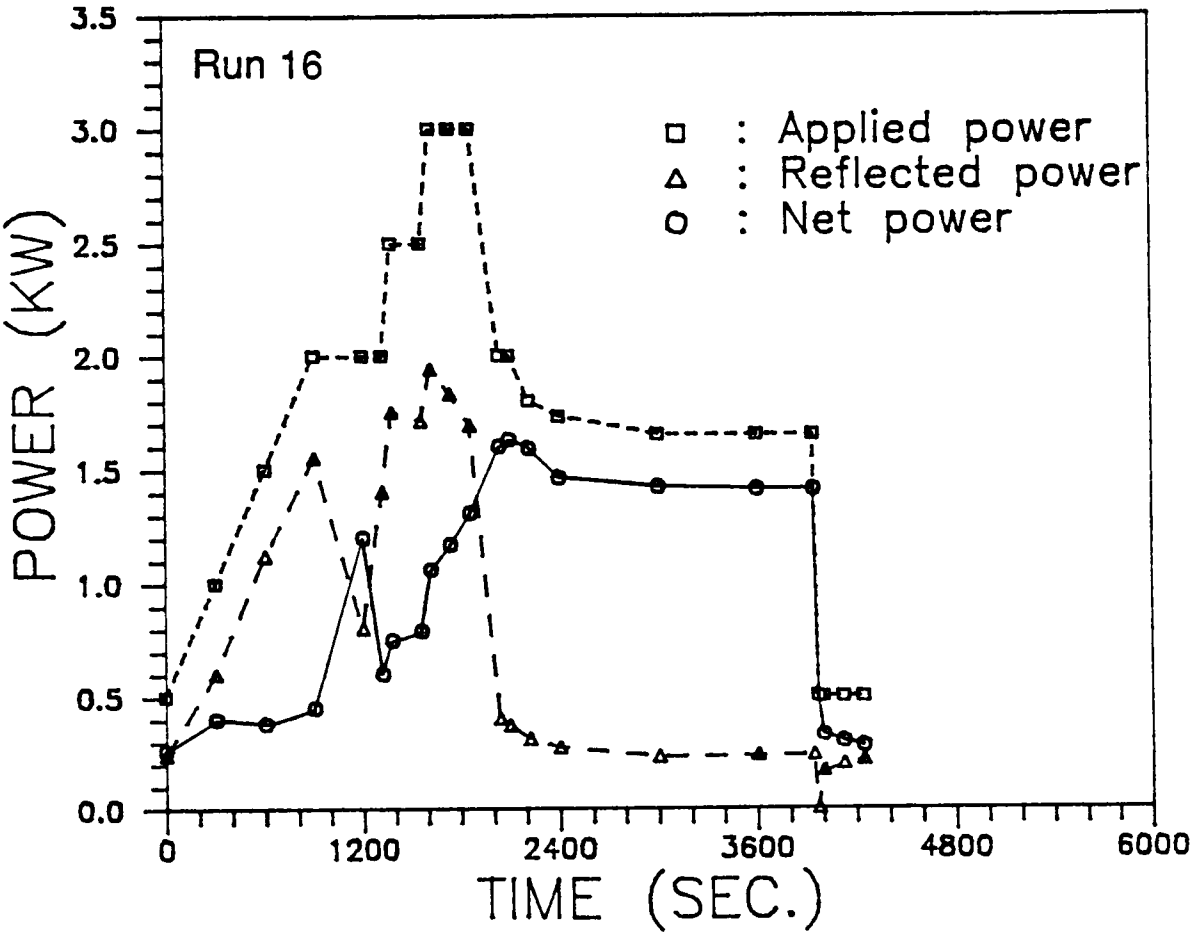


Figure 26. Power distribution in run 16 microwave sintering without susceptor.

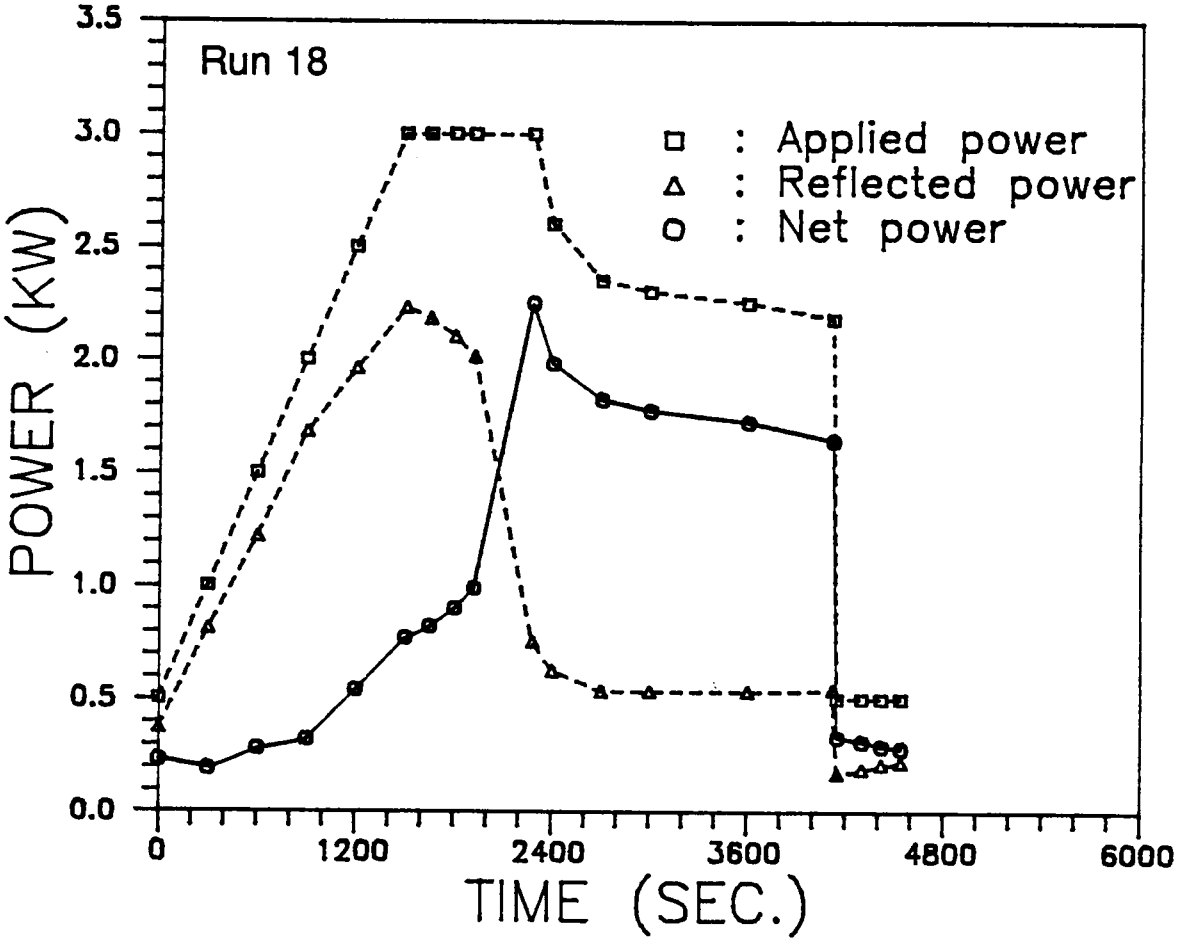


Figure 27. Power distribution in run 18 microwave sintering without susceptor.

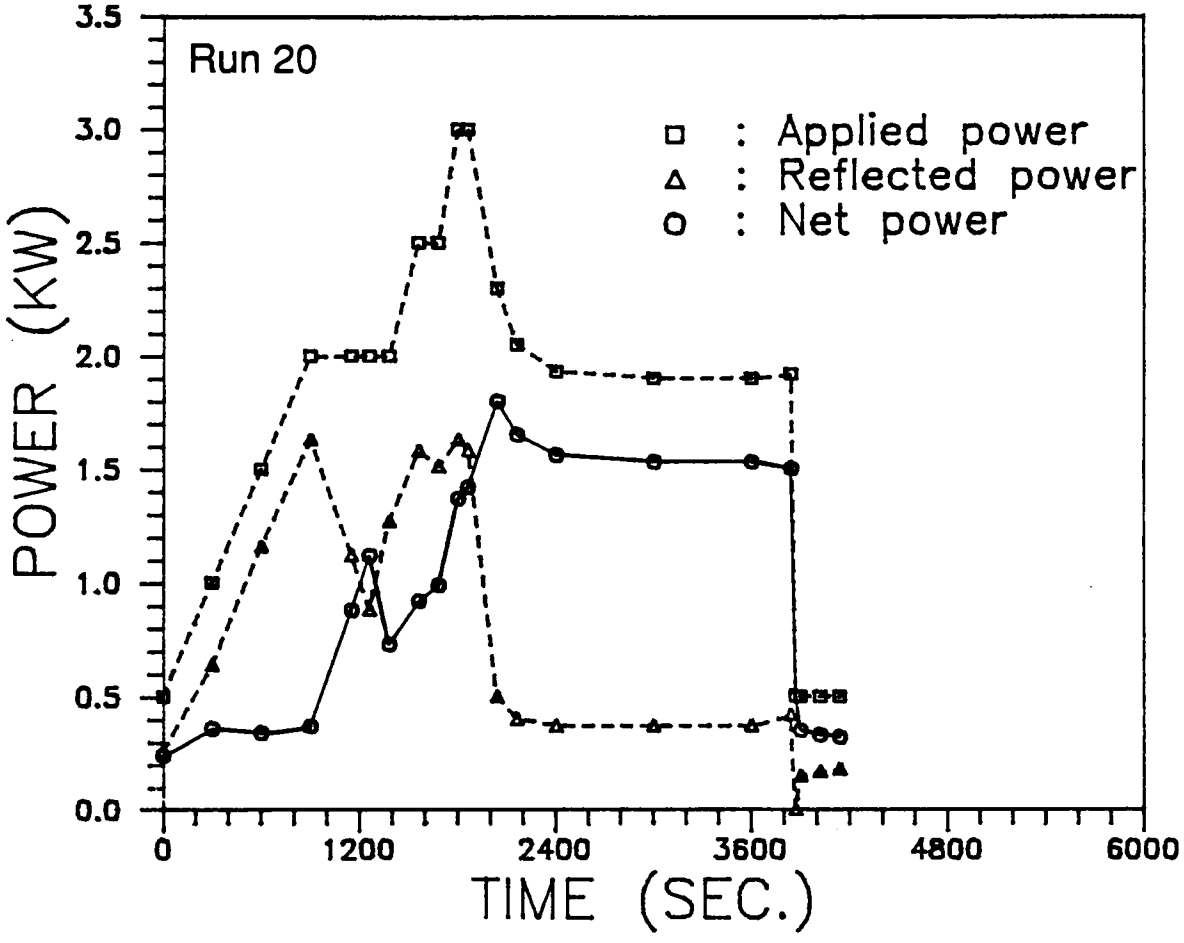


Figure 28. Power distribution in run 20 microwave sintering without susceptor

the sintering temperature, the input power was rapidly decreased approximately 1.0 to 1.5 KW to prevent thermal runaway, and then controlled to reach the sintering temperature. After reaching the sintering temperature, the input power was gradually decreased to maintain the sintering temperature. In the last three runs, coupling time was delayed because three samples were placed at 90 degrees to the electric field. It indicated that samples might be placed parallel to the electric field thus affecting their position relative to the maximum field intensity.

Figure 29 is a plot of sintering time versus surface temperature. Figures 30-33 are plots of sintering time versus power (input power, reflected power, and net power). These results show that the coupling time decreased with an increase in load mass. Also, these showed that samples coupled more easily at lower input power than for the case of no susceptor. This was because of the greater mass of the samples plus susceptor.

When new insulation was used, initially reflected power was low. After usuage reflected power increased, and finally became stable. Between these regions, there is assumed to be an exothermic reaction evidenced by a greatly increased reflected power as reported by Schubring (12). He assumed that exothermic behavior could be due to oxidation of carbon form the organic binders, reaction of the inorganic carbonates and oxidation of free carbonaceous impurities in the insulation. When the input power was increased to over 4.0 KW, the insulation glowed red and then partially melted. Therefore, if the mass of the sample to be heated is

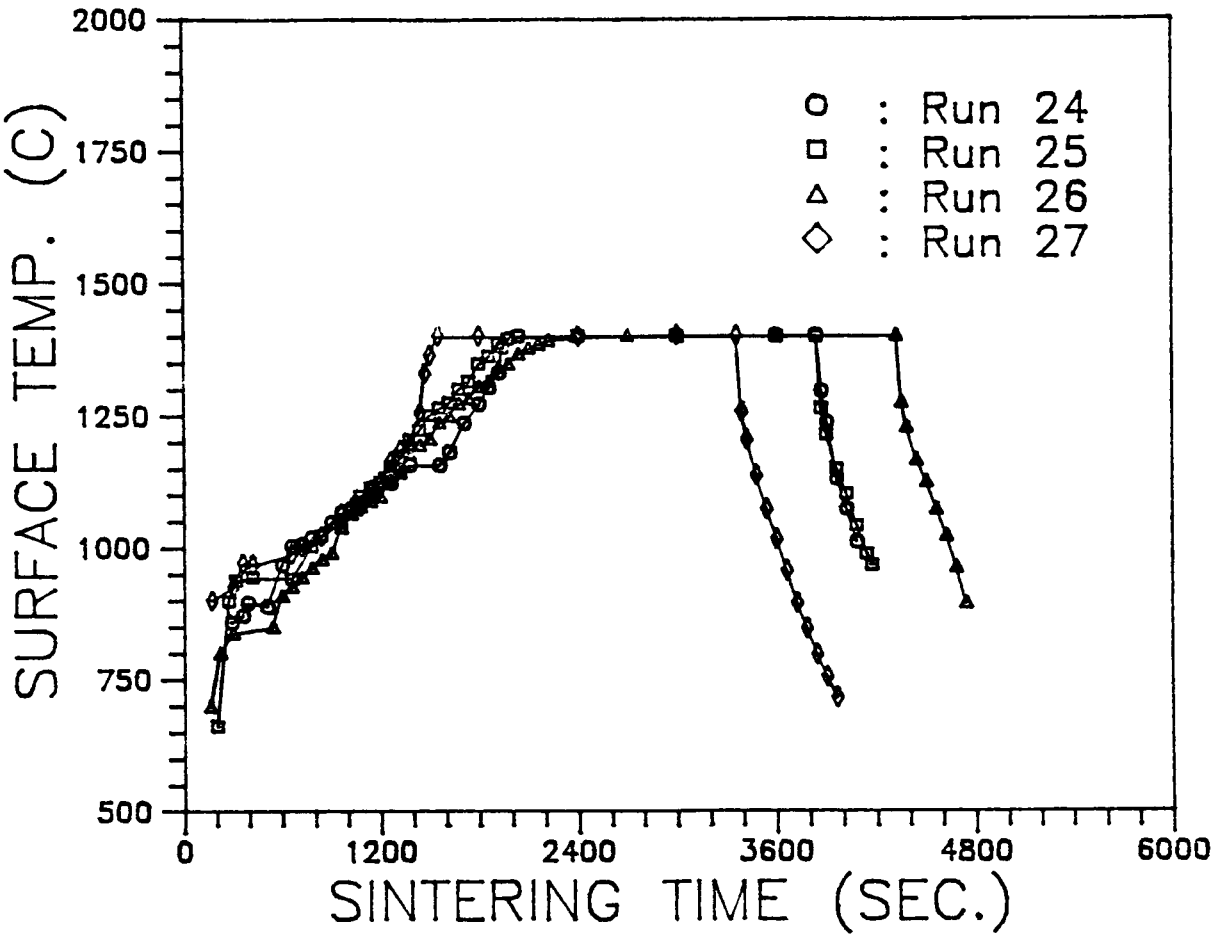


Figure 29. Temperature profile of microwave sintered sample with susceptor.

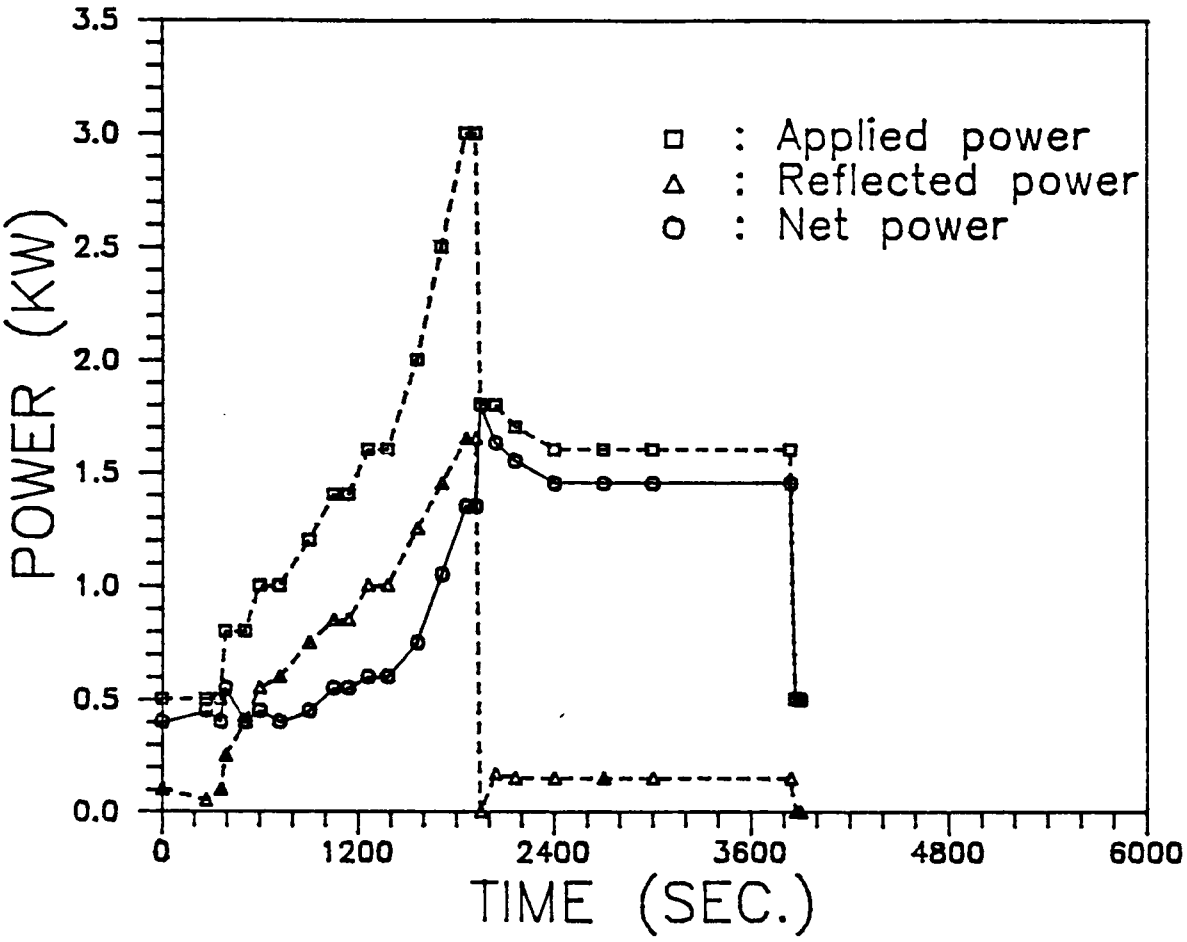


Figure 30. Power distribution in run 24 microwave sintering with susceptor.

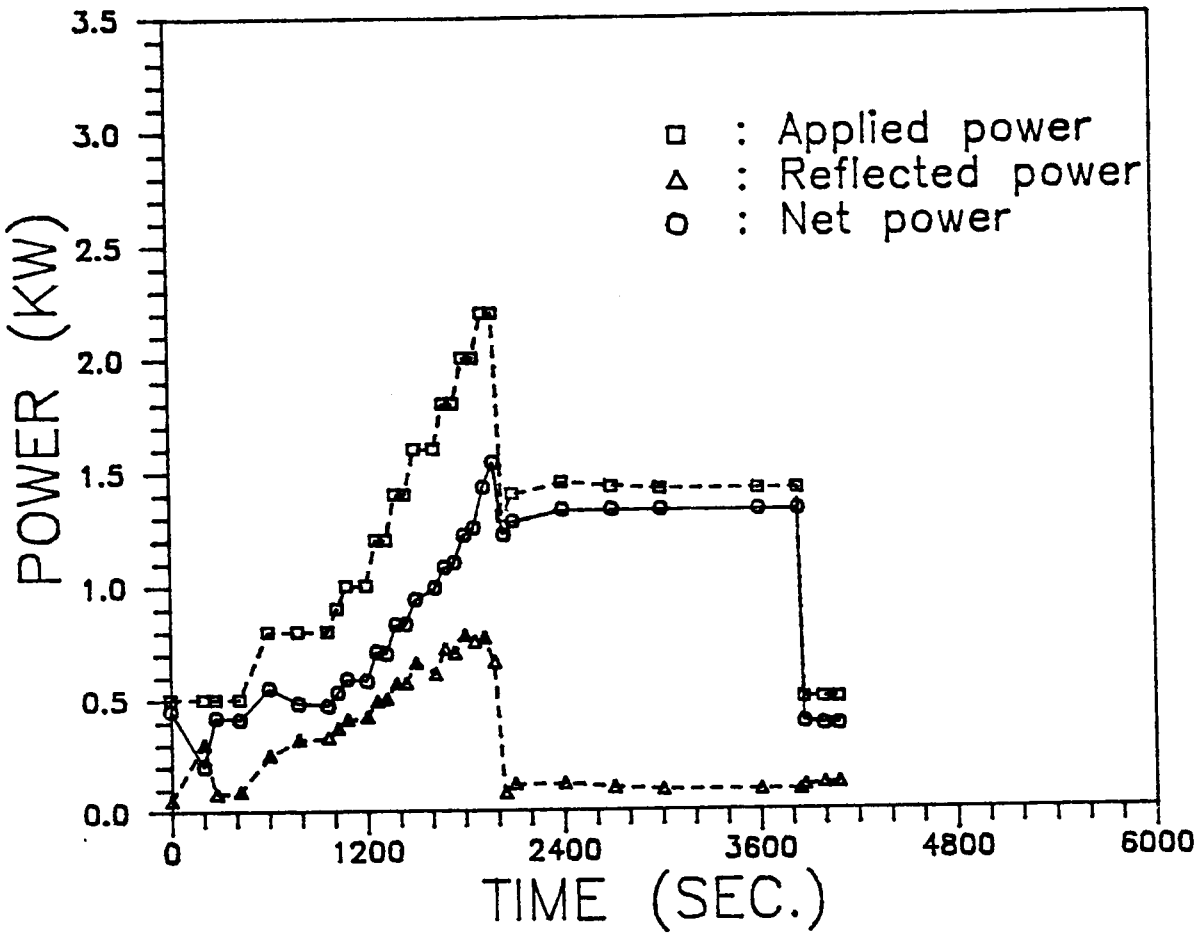


Figure 31. Power distribution in run 25 microwave sintering with susceptor.

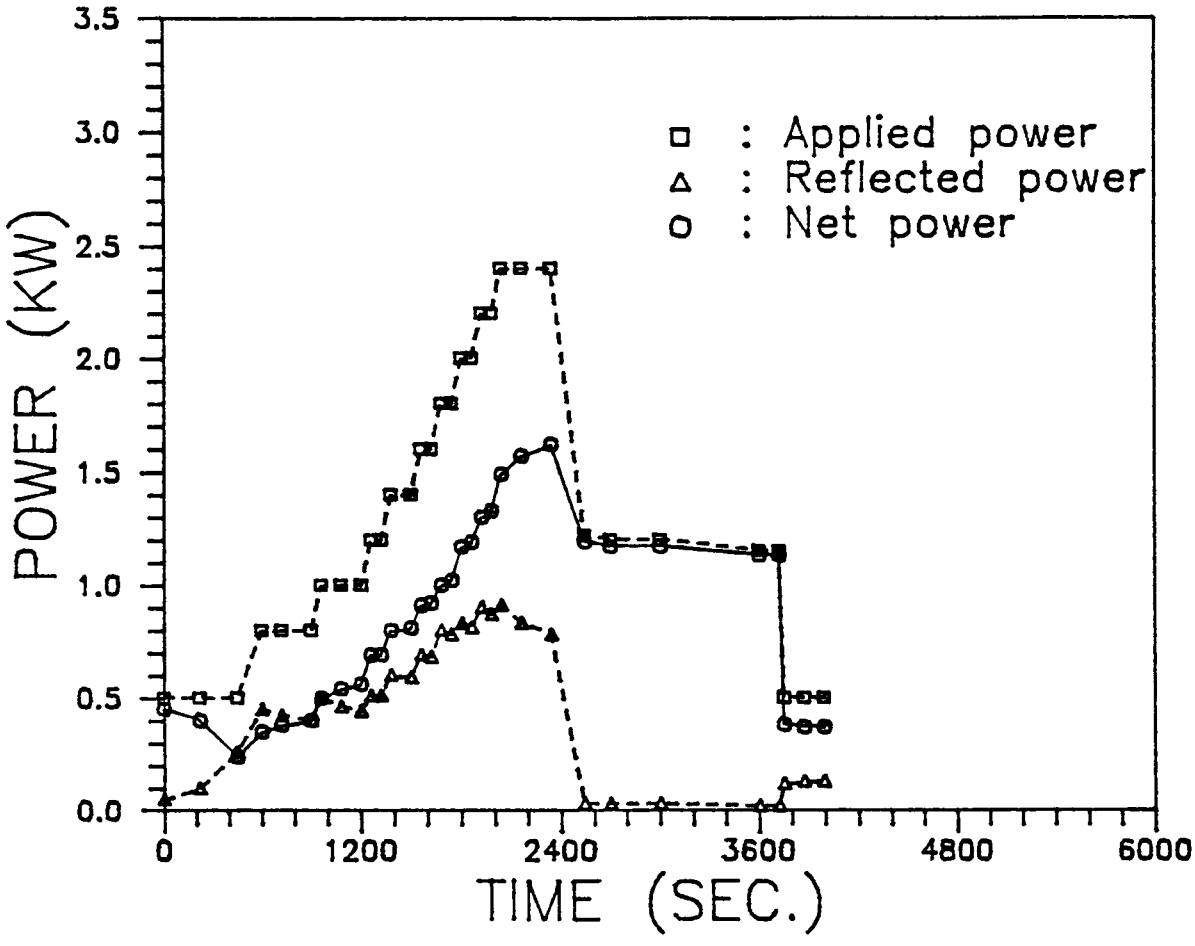


Figure 32. Power distribution in run 26 microwave sintering with susceptor.

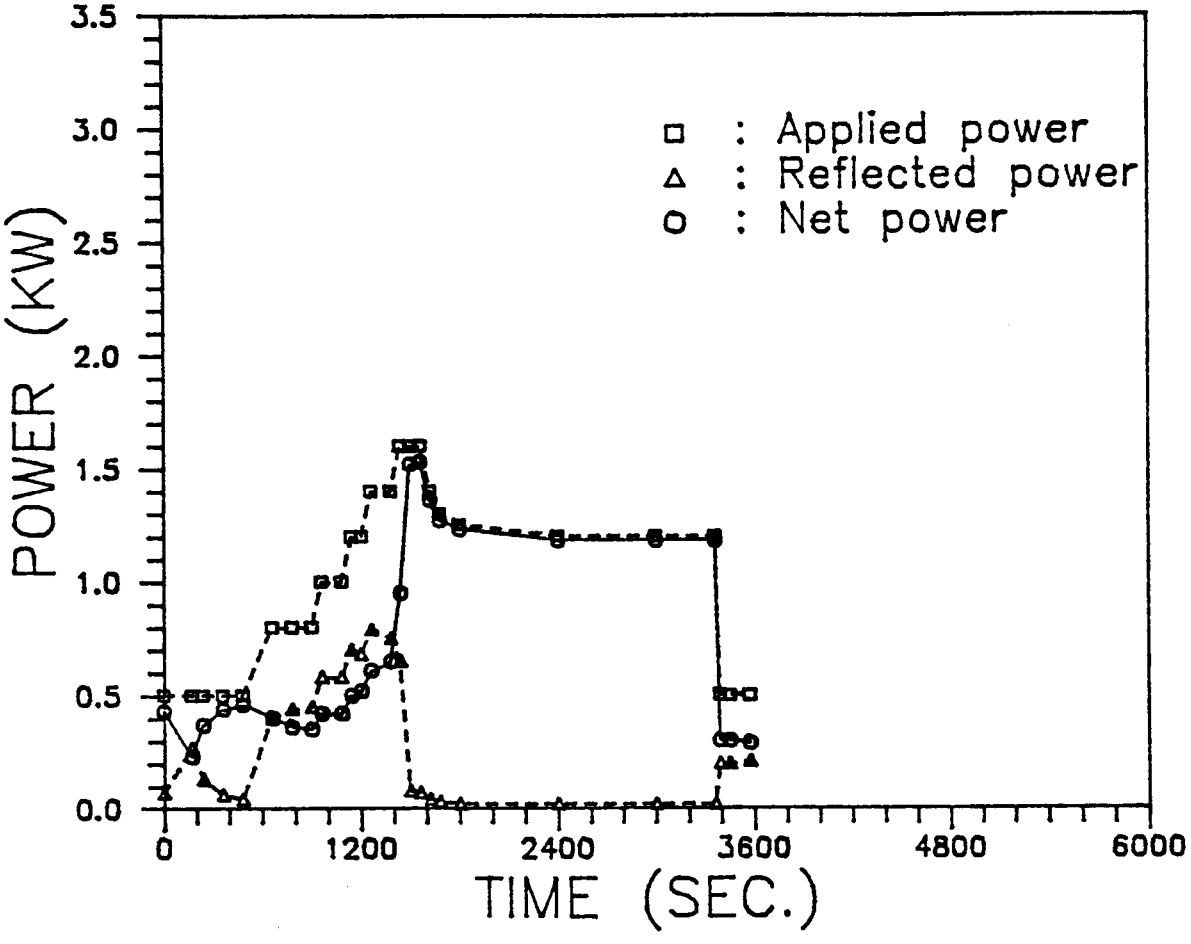


Figure 33. Power distribution in run 27 microwave sintering with susceptor.

very small relative to the mass of the low loss insulation, the electromagnetic field will deposit a large amount of its energy into the insulation rather than the sample thus heating the insulation and not the sample.

At above the critical temperature, the loss tangent rises very rapidly, which causes the material to begin to absorb microwave energy more efficiently. As a result, the loss tangent is increased even faster as the temperature is increased. The net result is an exponential increase in the loss tangent, which causes thermal runaway.

The thermal runaway condition was shown in Figures 24 and 29 on the previous page 99 and 105. In sintering with a susceptor, microwave energy was absorbed efficiently at room temperature, and thermal runaway occurred as soon as the sample was irradiated by microwave energy at a low power level. In sintering with no susceptor, microwave energy was less efficiently absorbed, thermal runaway did not occur at the same power level. However, when power was increased sufficiently, the initial rate of heating was increased to the point where thermal runaway could be triggered. The reason is the filling factor, which is the ratio of the load volume to that of the cavity and the loss tangent of the former was higher than that of latter. Another reason is that the loss factor of the susceptor is much higher than that of insulation.

During microwave heating with no susceptor, a significant fraction of the total heat generated in the cavity is actually generated in the cavity wall. While the samples were able to achieve a high

enough temperature, the external portions of the cavity was hot to the touch. However, during microwave heating with the susceptor, all of the heat generated was generated in the samples. When the temperature of the samples was already up to 1400 °C, the cavity wall was relatively cooler to the touch than in the former case. The coupling mechanism in the preheating step may be explained by the above results. It was assumed that the losses of the cavity walls occurred when very low-loss insulation materials are in the cavity and all of the heat generated is generated in the sample materials that are very high-loss materials.

Thermal runaway is an important aspect of microwave heating. It can cause undesirable hot spots within a material. There are several means to control or prevent thermal runaway, such as by controlling the microwave power level, by designing the microwave system, or by changing composition of material. During heating the dielectric constant and loss tangent change with temperature, and a knowledge of these changes is also important to control thermal runaway. In these experiments, the input power level was controlled.

Zirconia-alumina composites were successfully sintered to densities ranging from 97 to 100% TD not related to the sintering temperatures from 1400 to 1800 °C. The real sintering temperature (that is the intergranular temperature) is thought to be much higher than the measured surface temperature. This assumption will be explained in more detail in the microstructure analysis.

Influence of the microwave field on thermocouple measurement

Under the influence of the electromagnetic field present in the microwave reaction cavity, reaction kinetics may differ from normal thermal convection heating. The temperature difference is presented as a result of the fact that energy is deposited in the interior of the materials and radiated from the surface. A quantitative prediction of the temperature difference within the material requires detailed analysis of the electromagnetic field, combined with heat transfer considerations. Since data are not available concerning the profile of the electromagnetic field, it is not possible to explain in more detail. This may explain the differences in the respective microstructures.

It is realized that since the power output of the generator usually couples with the reflected power from the load, the temperatures of heated materials may fluctuate if the reflected power is not decoupled from the forward power and subsequently diverted as reported by Bhattacharyya (116). Also, the presence of metallic structures concentrates the electric field and produces unwanted hot spots as reported by Johnson (117). Therefore, direct temperature measurement using a thermocouple is extremely difficult in a microwave field due to its interference with the field which induces an extra voltage in the thermocouple wires. A thermocouple could be used by introducing it instantaneously into the cavity after shutting off the power or placing the wires at 90 degrees to the electric field which is difficult in the present case. As a result, the temperature measurements will not all be accurate due to the time taken for its insertion into the cavity.

Temperature measurement of samples was made by using an IR-meter and an R-type thermocouple during microwave heating. A Pt-13% Rh thermocouple was inserted through a two hole alumina tube with a shield wire wrapped around the tube with the pitch of the shield wire being less than a quarter wavelength of the microwave to prevent any interaction with the microwave radiation. The thermocouple was placed near top of the sample. The IR-meter was focussed on the front edge of the sample through a small hole in the front of the cavity wall.

Figure 34 shows the temperature profile data taken using a thermocouple and an IR-meter. There is a large difference between the two sets of data. Also, during heating the thermocouple was melted at 1000 °C. This indicated that a thermocouple will not correctly indicate a local temperature in the vicinity of the thermocouple. Therefore, an IR temperature was used for all experiments because it neither perturbed the electromagnetic field nor caused a hot spot and resulted in more accurate temperature data.

The sample temperature as measured by an IR meter corresponded to the surface temperature which was lower than the sample internal temperature due to radiation and convection losses. That meant that no temperature comparison was possible with conventional heating where the temperature gradient was inverted as suggested by Berteaud (11). It indicated that neither an IR meter nor a thermocouple yielded the important temperature relative to the understanding of important physical phenomena such as

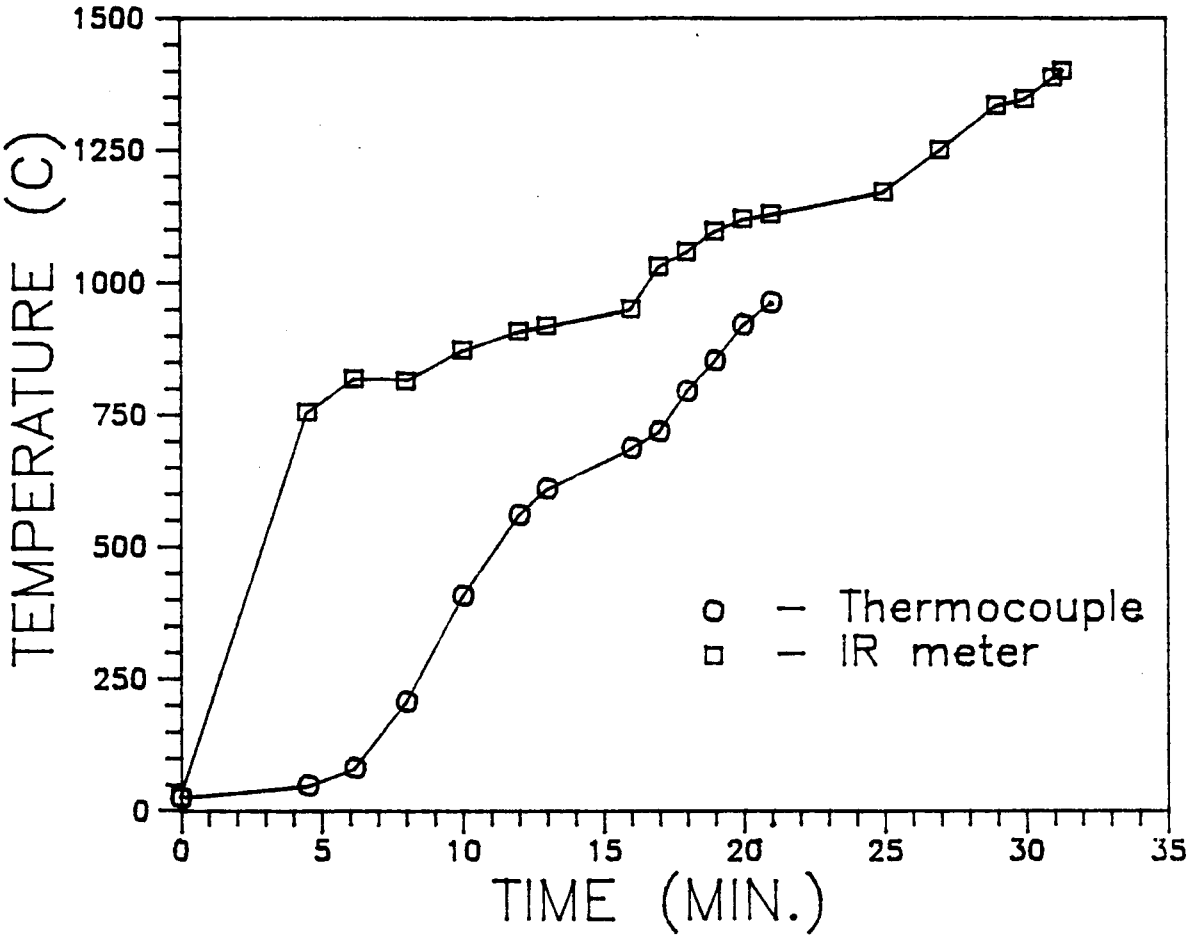


Figure 34. The measured temperature profile of the sample by using IR meter and thermocouple.

sintering activation energy.

Meek (118) proposed that adequate techniques of measuring temperature in the electromagnetic field were the determination of temperature using some non-invasive technique such as the measurement of the reflected impedance of a coil or the dc-resistance of a sample as a function of temperature. The reason is that he believes the important temperature to measure is on the surface of sintering grains, in the grain boundaries between grains, or wherever there was a discontinuous change in local material dielectric properties.

The above only served to present a relative temperature. Therefore, further work needs to be done to measure the accurate temperature by using a non-invasive technique.

IV-3. Densification Behavior in Microwave Field

Bulk density of the sintered samples was measured by the water immersion method. Tables 5 and 6 show the bulk densities of the conventionally sintered and the microwave sintered samples. The bulk densites were plotted as a function of the sintering time and the surface temperature in Figure 35.

As may be seen in Tables 5 and 6, the minimum microwave sintered density observed was over 95% TD at any sintering temperature and time. However, the maximum density of the conventionally sintered sample was 92.59% TD at 1350 °C for 108 hours. Clearly, Densification rates for the microwave sintered samples are much higher than for the conventionally sintered

Table 5. Density of microwave sintered samples.

Sintering Temperature (Degree C)	Sintering Time (Min.)	Initial Density (%)	Final Sintered Density (%)
1200	5	50	94.99
	10	50	95.25
	30	50	95.92
	60	50	98.54
1300	5	50	94.72
	10	50	95.38
	30	50	96.88
	60	50	98.88
1400	2.5	50	98.5
	5	50	98.29
	10	50	98.63
	30	50	99.33
1500	2.5	50	97.94
	5	50	98.35
	10	50	100
	30	50	100

Table 6. Density of conventionally sintered samples.

Sintering Temperature (Degree C)	Sintering Time (Hour)	Initial Density (%)	Final Sintered Density (%)
1350	14	50	80.98
	24	50	86.3
	38	50	88.08
	48	50	90.17
	60	50	90.49
	72	50	91.1
	84	50	92.56
	108	50	92.59

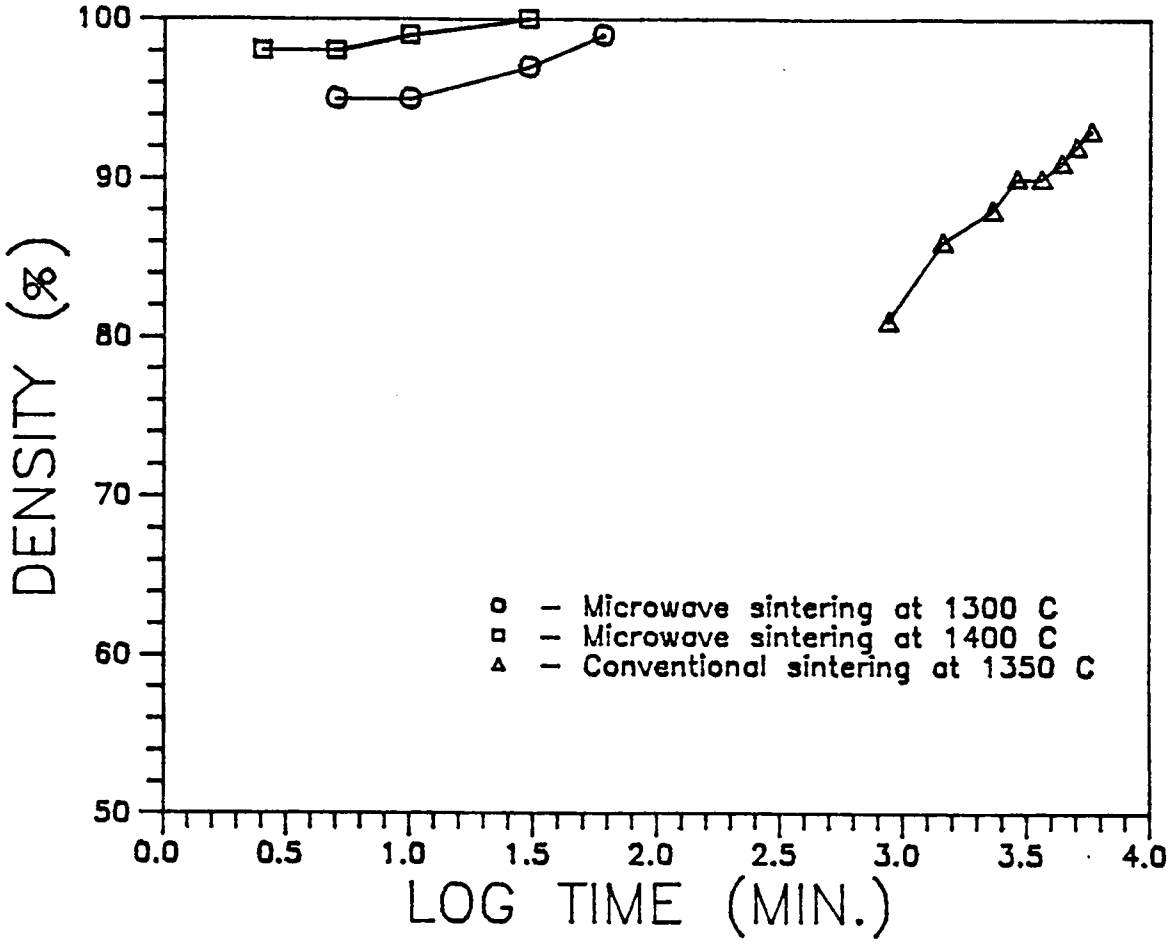


Figure 35. Densification rates for microwave sintered samples and conventionally sintered samples at a comparable temperature.

samples at a comparable temperature; For all samples, the initial density (50%) and the processing pressure (230 MPa) were the same for both processes.

The enhanced sintering characteristics were most likely the result of the extremely fast heating rates achievable by the unique direct heating mechanism. It meant that microwave sintered samples were densified much more rapidly and at much shorter time and lower temperature than the conventionally sintered samples.

As shown in Figure 35, independence of density with the sintering temperature over such a large range for microwave sintering is certainly unusual but could be readily explained by examination of a microstructure as shown by Katz (34).

The total porosity of the conventionally sintered samples was much higher than one of the microwave sintered as shown in Table 7. The reason was that the microwave heated samples exhibit nonconnected porosity located within grains and at grain boundary. Rapid densification resulted in smaller pores at a given grain size. These smaller pores exerted less drag on the grain boundaries which could consequently migrate quickly giving rise to grain growth.

Also, enhanced diffusion appeared to be responsible for the accelerated densification rates in the microwave heating. Previous work (30) on the microwave processing of ceramic and ceramic composite materials suggested that enhanced transport properties occurred in an electromagnetic field. Tian (37) reported that microwave heating (the extremely fast heating) led to the early activation of grain boundary and lattice diffusion before surface

Table 7. Physical characterization of microwave sintered and conventionally sintered samples.

(Theoretical Density = 5.5 g/cm3)

Characterization	Sample Number	Sintering Temp. and Sintering Time	Total Porosity	Real density
Microwave	M - 49	1400 °C x 30 Min.	0.05%	5.473 (g/cm3)
	M - 50	1400 °C x 30 Min.	0.07%	5.463 (g/cm3)
Conventional	C - 63	1350 °C x 108 Hr.	14.35%	4.710 (g/cm3)
	C -82	1350 °C x 108 Hr.	16.96%	4.567 (g/cm3)

diffusion could significantly coarsen the microstructure and reduce the driving force for sintering in alumina.

As shown in Figure 36, the apparent activation energy is calculated by an equation of the form as below (46);

$$\rho = \rho_0 \, EXP \, (- H_d / RT)$$

where H_d is the apparent activation energy associated with densification rate, and ρ is the densification rate.

The calculated activation energy was about 13 Kcal/mol for microwave sintering and 148 Kcal/mol for conventional sintering quoted from Wakai (107). Although the measured temperature was not a relative value, the large difference in the sintering rate was thought to be due to higher diffusion rates induced by the microwave field. An explanation for this reasoning is given earlier in the discussion on how the energy of the electromagnetic field partitions itself in a dielectric material. As a same trend, Janney (33) reported that the apparent activation energy for microwave heating was about one-third that of conventional heating.

It is clear that the electromagnetic radiation is responsible for the observed phenomenon of a tremendous increase in the densification rate. However, the mechanism by which the diffusivity of the material is increased is not at all understood. For the preparation of a ceramic with a high density and small grain size, it is necessary that densification is enhanced and grain growth suppressed. Therefore, microwave sintering has a potential of

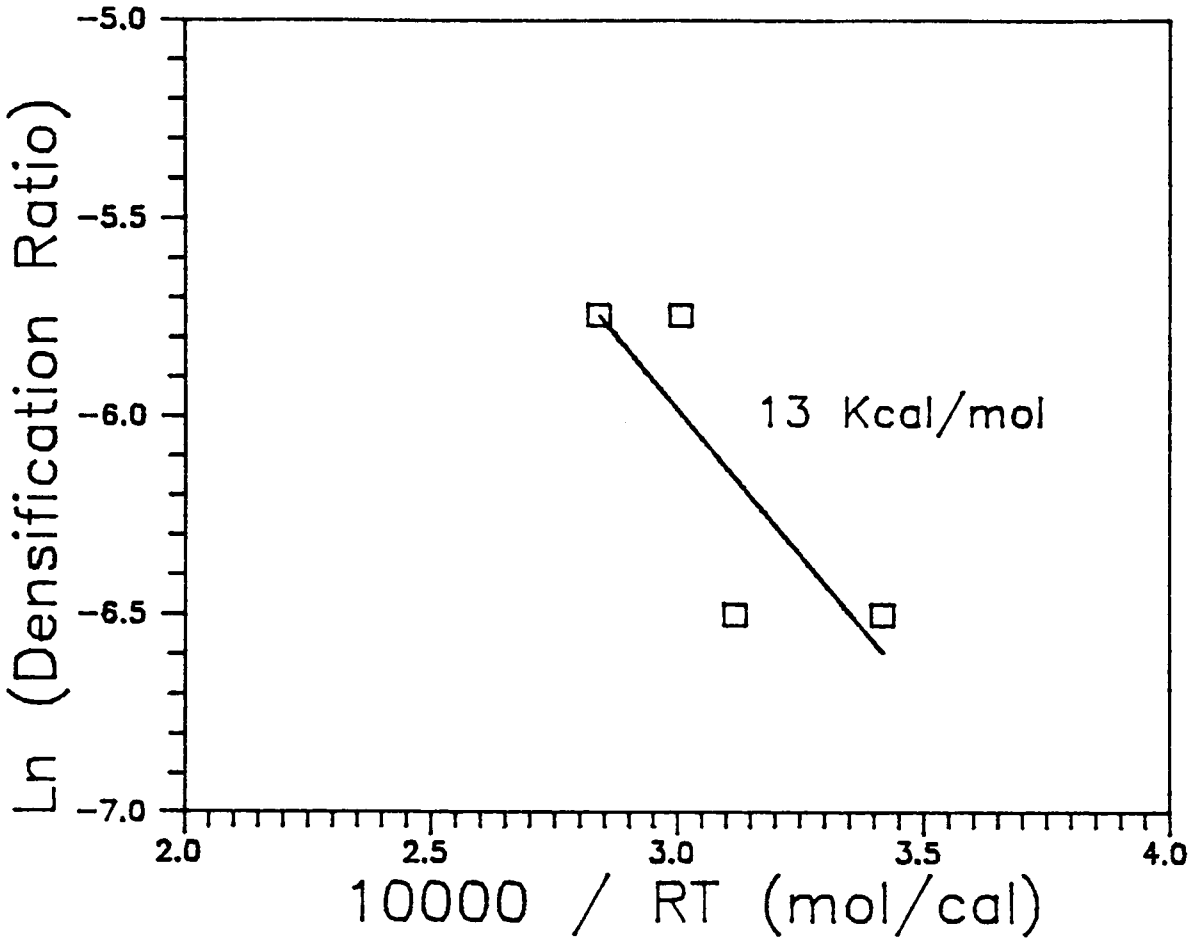


Figure 36. The expected activation enthalpy for microwave sintering.

enhanced densification and suppressed grain growth due to a fast heating rate and an apparent low-temperature firing.

IV-4. Phase Analysis

The observed X-ray diffraction patterns for the center layer in the conventionally sintered and the microwave sintered samples are shown in Figures 37 and 38. While the X-ray diffractometer provided information only from the center layer of the sample, it is known that the surface of the sample which had been carefully polished, was representative of the bulk sample as reported in a previous paper.

In the present case, X-ray diffraction analysis of the polished microwave sintered samples showed the presence of tetragonal-phase zirconia and α-alumina only. The peak patterns for the conventionally sintered samples were similar to the microwave sintered samples except for the traces of the monoclinic phase zirconia. Figure 39 shows a comparison between microwave and conventionally sintered material using a more accurate scan rate.

The fraction of the monoclinic phase zirconia in the sample was determined by the procedure reported. The fraction of the monoclinic-phase zirconia could be determined by measuring the relative intensity of the (111) and ($11\bar{1}$) monoclinic and (111) tetragonal reflections. By using equation III-3, the fraction of the monoclinic-phase zirconia was found to be approximately 28% in the conventionally sintered samples and almost 0% in the microwave sintered samples. Wilson (119) reported that the X-ray diffraction

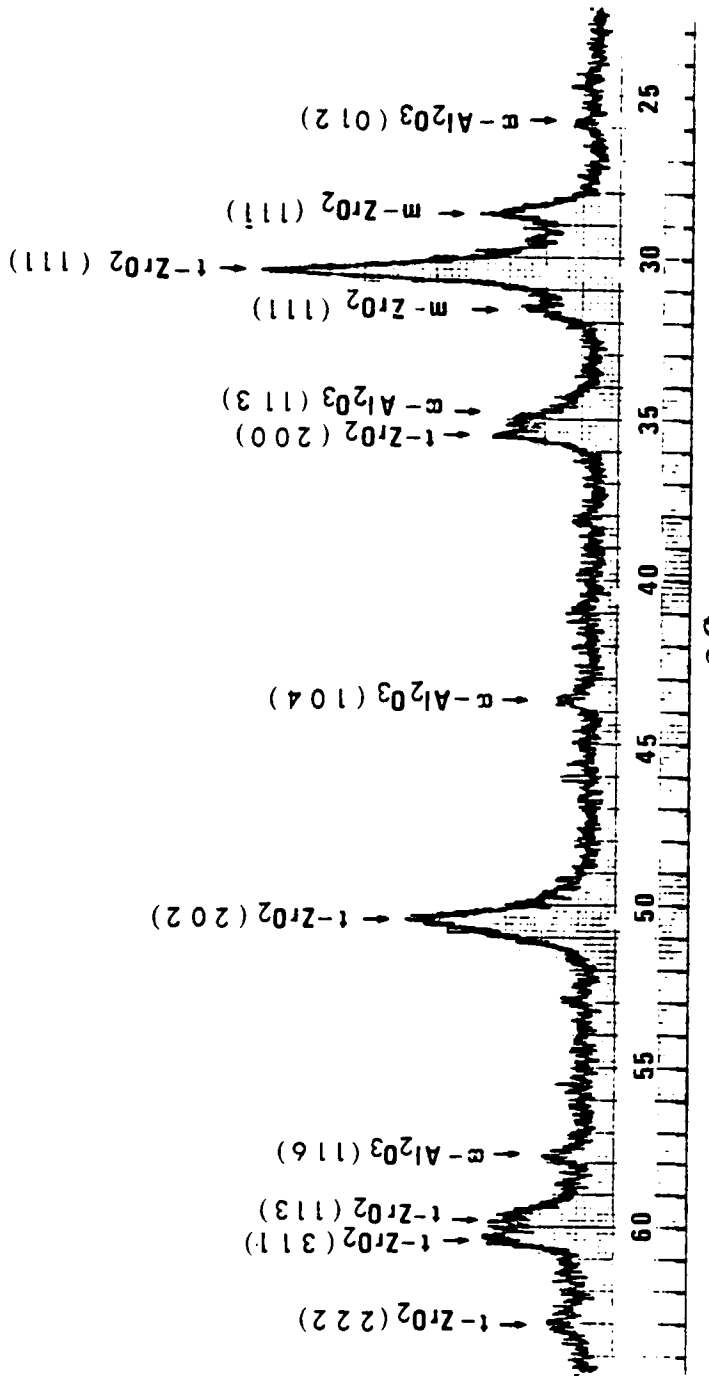


Figure 37. X-ray diffraction patterns of the conventionally sintered zirconia-alumina composte.

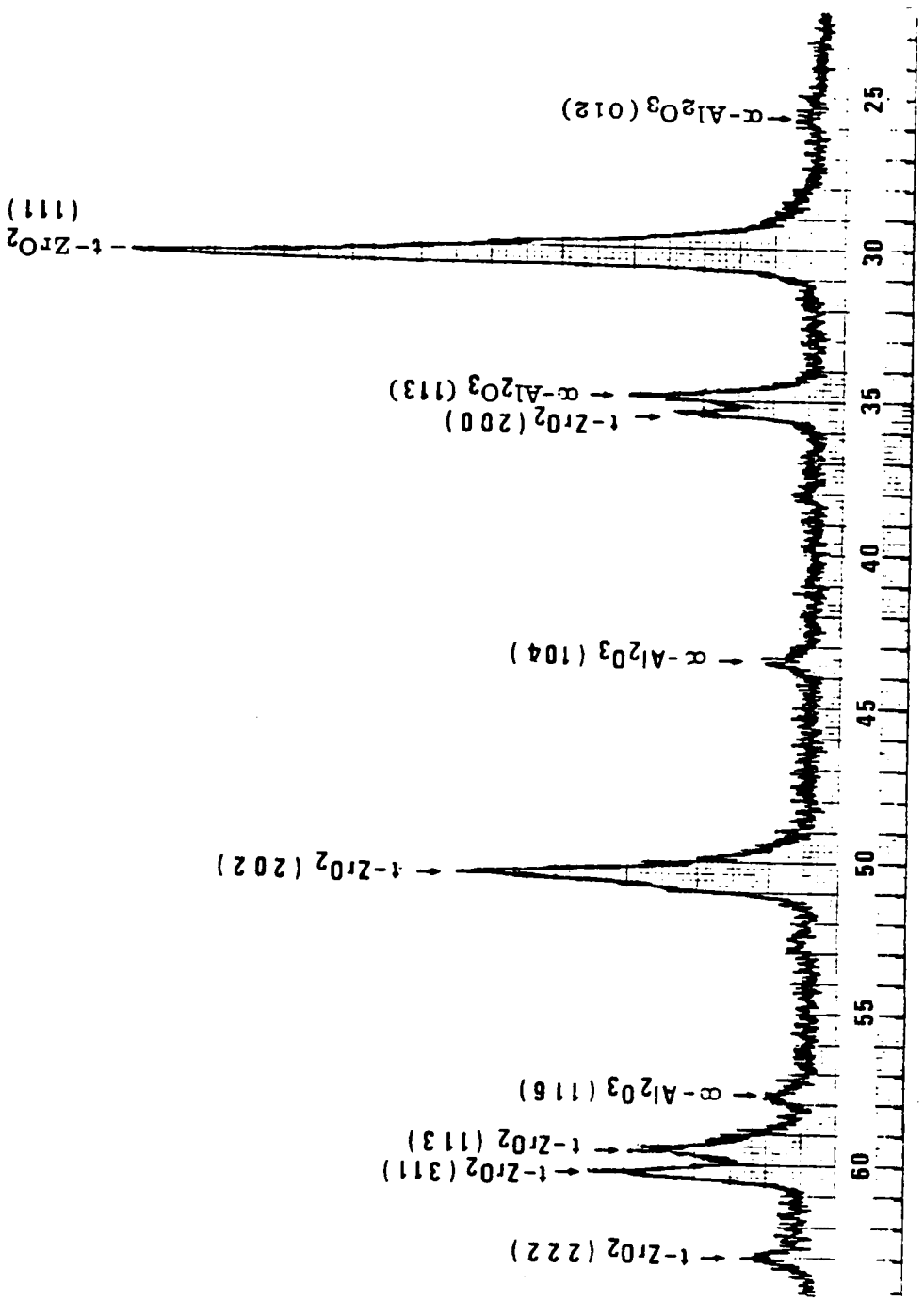


Figure 38. X-ray diffraction patterns of the microwave sintered zirconia-alumina composite.

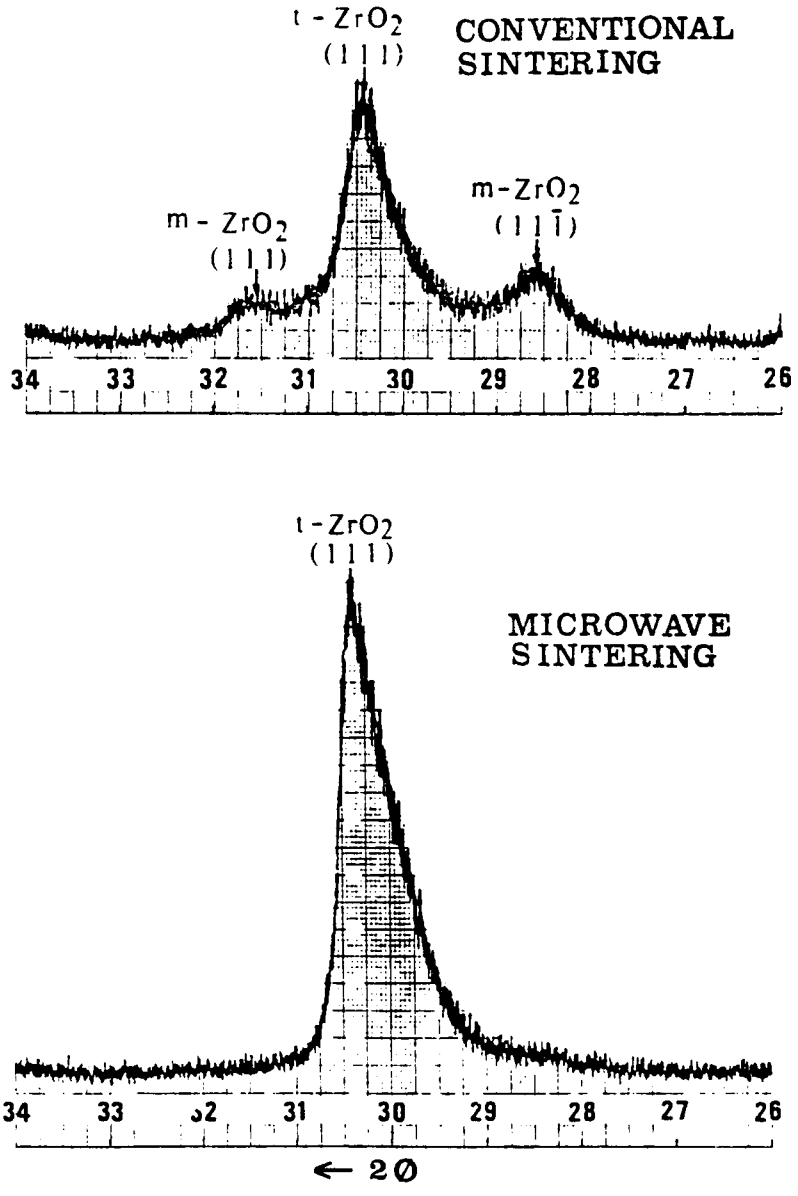


Figure 39. The comparison of the X-ray diffraction patterns in the microwave sintered and the conventionally sintered sample.

scans showed a mixture of tetragonal and cubic phases, but essentially no conversion to the monoclinic phase in the microwave sintered zirconia. Thus, the microwave sintered samples retained the metastable tetragonal grains better than the conventionally sintered samples. This effect was assumed to be responsible for the high degree of retained strength in the microwave sintered sample after the thermal shock as suggested in a previous paper (101).

In radiant or convection heating, energy is absorbed only at the surface of the material and must be transfered into the bulk of the material by thermal conduction. Thermal conduction takes a finite amount of time, gradients in temperature within the material must exist until the material achieves thermal equilibrium. On heating, the maximum stress in the ceramic material is the compressive stress on the surface and the center is in tension as shown in Figure 7 (62). The tetragonal phase converting to the monoclinic phase can occur when thermal stresses reach a critical value either from the center tensile stress or from the surface compressive stress during the conventional sintering. Therefore, thermal tensile stress is absorbed by the volume expansion associated with this trasformation, and then the tensile stress level in the center is reduced. It was assumed that the monoclinic phase existed in the conventionally sintered sample due to thermal stresses.

However, in microwave heating, energy is absorbed throughout the volume of a material because heating occurs within the material volume by the electromagnetic energy causing the molecules throughout the volume to vibrate. It is assumed that material is

heated uniformly without gradients in temperature during microwave heating on a macroscopic scale. Thus, the monoclinic phase did not exist in the microwave sintered sample due to no thermal gradient.

As a result, microwave sintering has the ability to sinter brittle ceramic materials toughened and strengthened by utilizing the phase transformation of zirconia particles dispersed in a ceramic matrix.

IV-5. Thermal-Shock Property

Earlier works by Meek (23) and Holcombe (120) indicated that sintering in a microwave field might affect the thermal-shock properties of ceramics and glasses. For this reason, the thermal-shock properties of the zirconia-alumina composite were investigated. Samples of the conventionally sintered and the microwave sintered materials were subjected to a wide range of thermal shock by quenching them into boiling water at ambient temperature from temperatures up to 900 °C. Thermal-shock damage to the samples was determined by measuring the retained strength after the quench. Optical microscopy was also performed on selected samples to reveal microcrack modifications due to thermal stresses.

Table 8 gives the thermal-shock data on the conventionally sintered and the microwave sintered samples. Figure 40 is a plot of the data shown in Table 8. The general trend of the curve is not similar to that derived from Hasselman's thermal-shock model for brittle materials illustrated in Figure 9. The retained compression

Table 8. Thermal-shock strength of the conventionally and microwave sintered samples.

Microwave Sintering				Conventional Sintering			
Sample Number	Delta T (degree C)	Average Compression Strength Ksi	(MPa)	Sample Number	Delta T (degree C)	Average Compression Strength Ksi	(MPa)
37A, 38A, 18Z	0	116	(80)	1B, 2B, 3B	0	114	(79)
4A, 27A	300	109	(75)	4B, 5B, 6B	300	112	(77)
5A, 31A	400	116	(80)	7B, 8B, 9B	400	104	(72)
21A, 32A, 4Z	500	101	(70)	10B, 11B, 12B	500	106	(73)
23A, 33A, 5Z	600	100	(69)	13B, 14B, 15B	600	107	(74)
24A, 6Z	700	99	(68)	16B, 17B, 18D	700	102	(70)
25A, 35A, 7Z	800	100	(69)	19B, 21B, 18D	800	98	(68)
26A, 36A, 8Z	900	94	(65)	22B, 23B, 24B	900	111	(76)

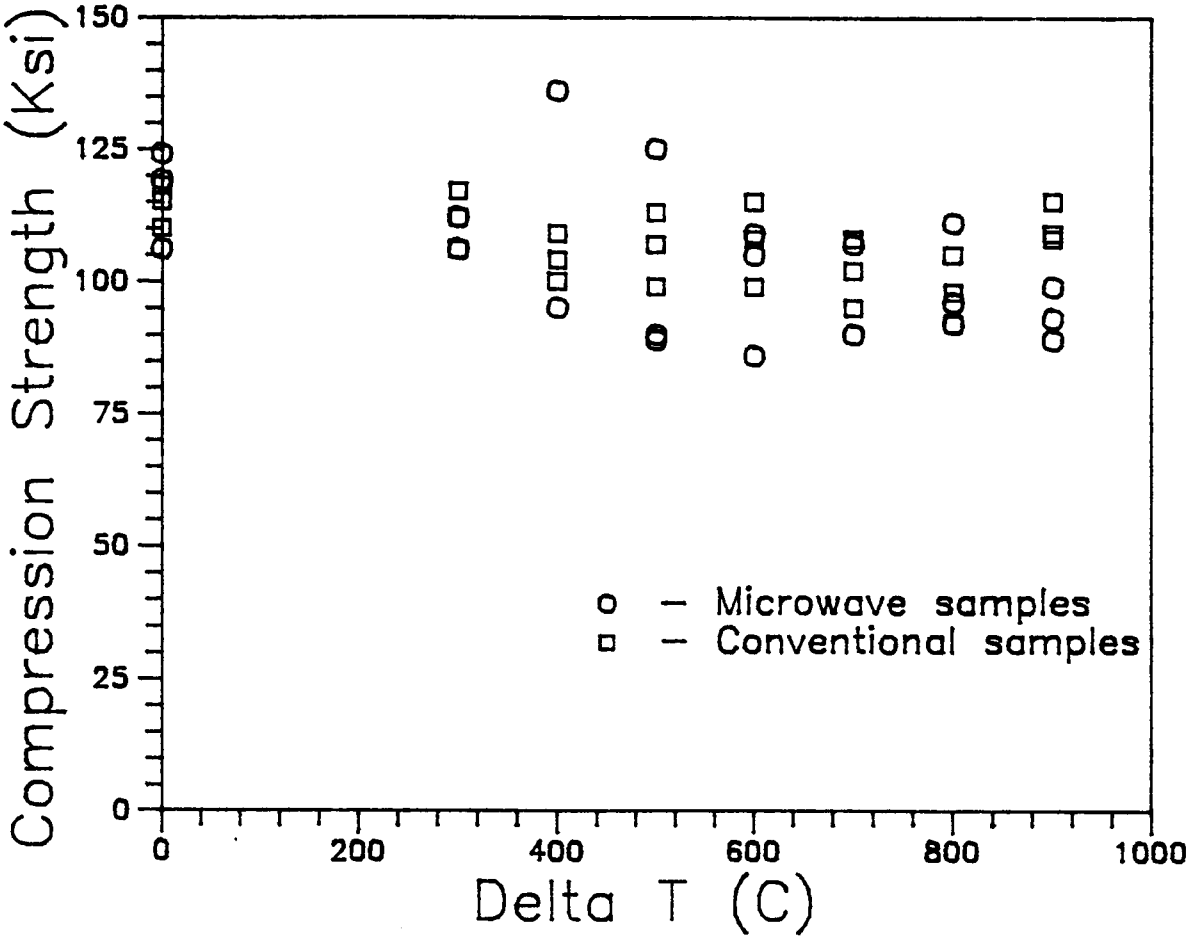


Figure 40. The compressive strength of microwave and conventionally sintered samples after thermal shock at various temperature.

strength of both cases gradually decreased to a low level with increasing temperature difference, so there was no rapid strength degradation for both cases. It was expected that the decrease of the compressive strength was due to the reduction in the contribution of phase transformation thoughening. According to the transformation toughening theory, the energy absorbed by a phase transformation decreased with increasing temperature because of the reduction of the differential free energy between the tetragonal and monoclinic phases.

The thermal-shock resistance of the conventionally sintered and the microwave sintered samples was approximately the same unlike data for another ceramic discussed in a previous paper. Also, the wide variation in the microwave sintered samples was unusual as compared to the conventionally sintered samples. One reason must be that some microcracks as shown in Figures 58 and 59 on page 159-160 were observed in the microwave sintered samples, because the heating and cooling rates in microwave sintering was more severe than that for conventional sintering. It is assumed that these microcracks degraded the compressive strength of the microwave sintered samples. Also, Figures 41 and 42 show that the polished surface of the conventionally sintered samples were more severely cracked than the microwave sintered samples after thermal shock. From microstructural data it is assumed that the thermal-shock resistance of the microwave sintered samples may be better than that of the conventionally sintered samples.

The factors that contribute to the enhanced thermal-shock of the

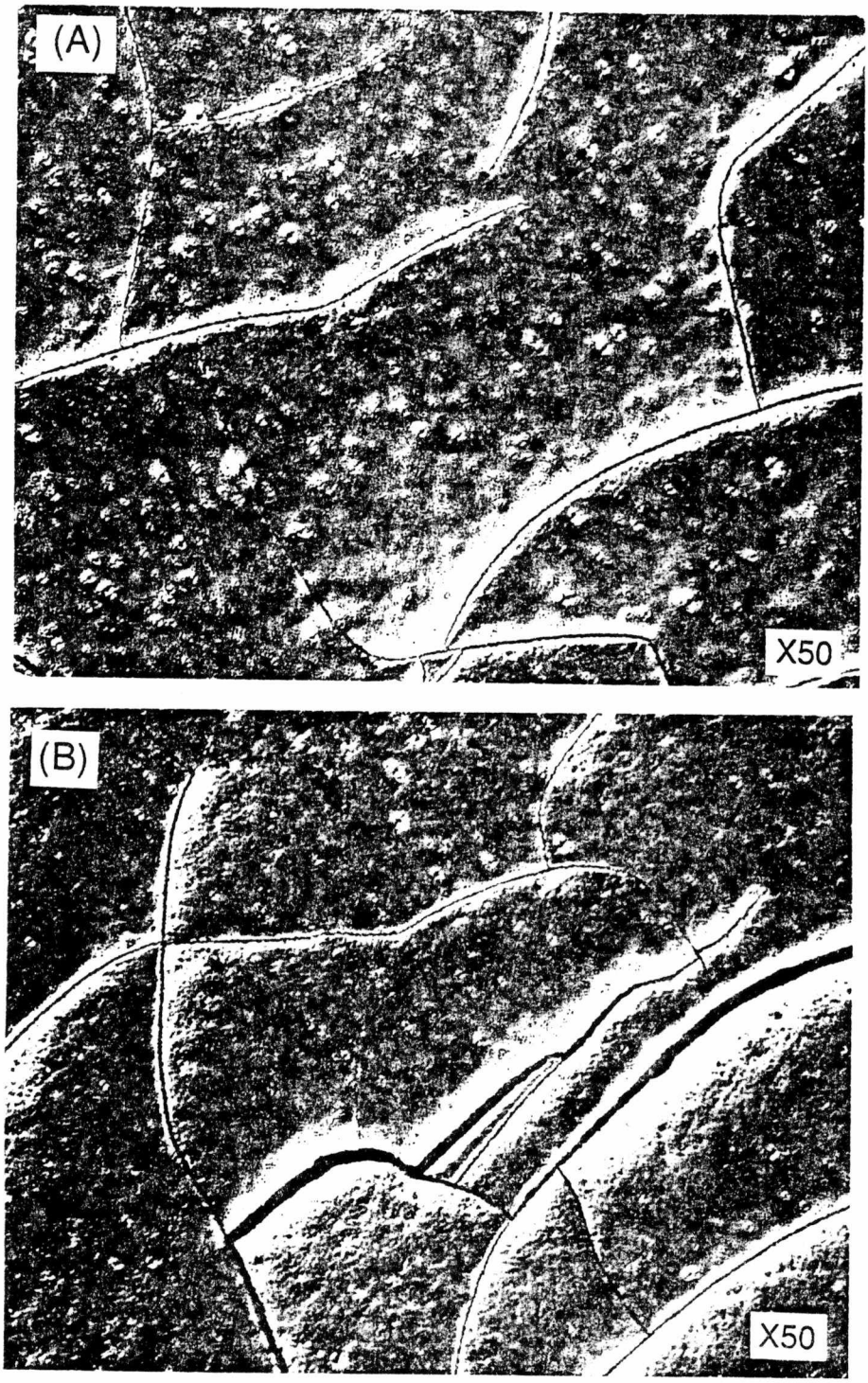


Figure 41. Optical micrographs of the conventionally sintered composite after (a) thermal shock 1 time at 900 °C and (b) thermal shock 5 times at 800 °C.

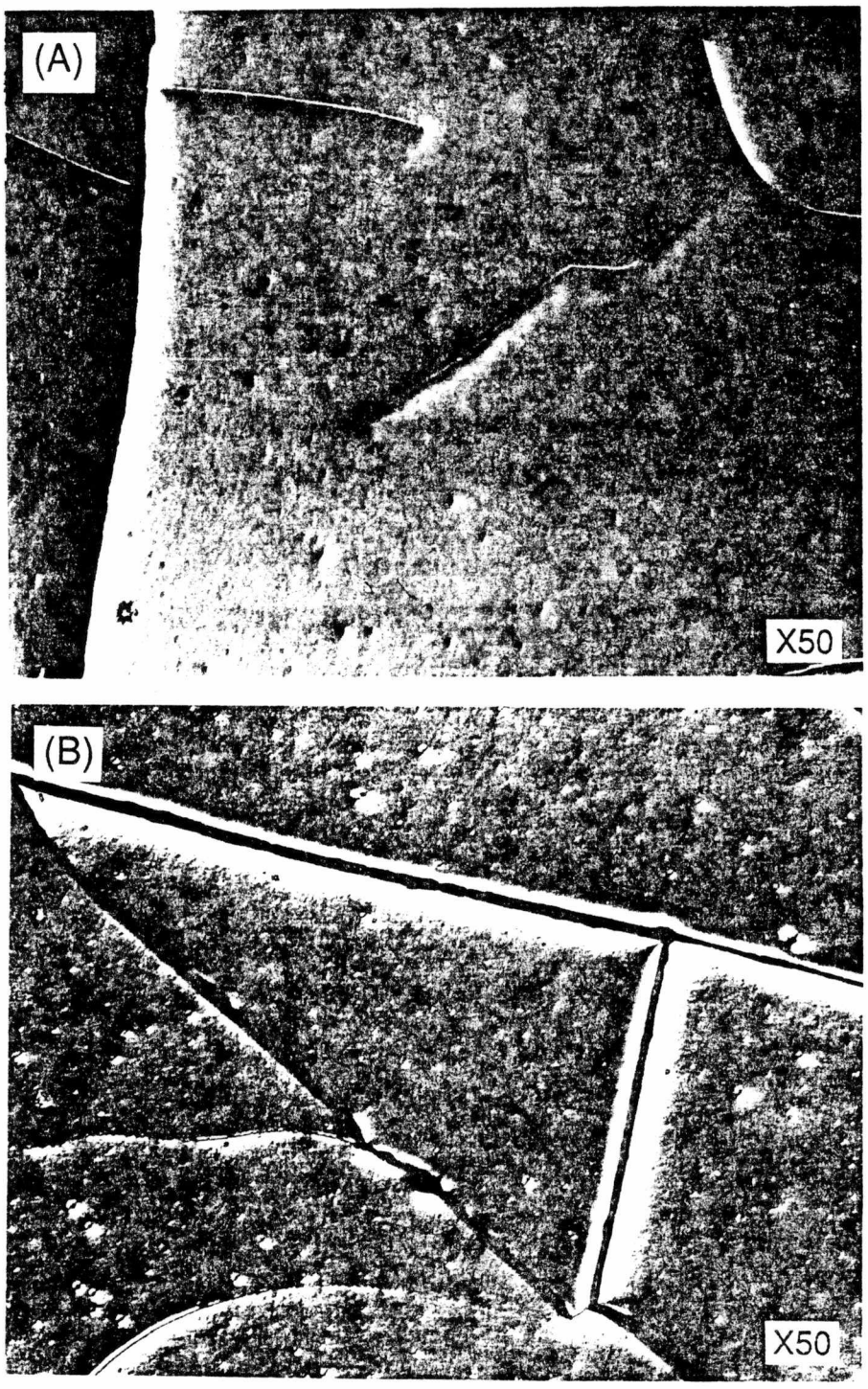


Figure 42. Optical micrographs of the microwave sintered composite after (a) thermal shock 1 time at 900 °C and (b) thermal shock 5 times at 800 °C.

zirconia-alumina composite are unclear; however, if sintering in an electromagnetic field occurs as described in an earlier paper by Meek (22), then the following explanation may describe the observed data.

If the magnitude of the electric field intensity is greater in the lower dielectric constant region and less in the higher dielectric constant region, the electric field intensity becomes greatest in the pores between grains in the green samples. Therefore, the lower dielectric constant region between the grains will be initially non-uniformly heated more rapidly than the interior of the grains. This means that the surface of each grain will heat faster than the interior of the grains. With further densification, this energy partitioning would cease, since the microstructure will become uniform.

As the green sample sinters and pores become closed and spherical, the surface of each pore (the lower dielectric constant region) will heat faster than the surrounding region. As a result, the pore surface may be melted as shown in the micrographs in Figures 56 (d) and 59 on page 154 and 160, and then each pore will act as a crack inhibitor upon the thermal shock. The thermal-shock properties may be improved because the region arround each pore is compressed.

When a microwave sintered sample was fractured, transgranular fracture was usually observed rather than intergranular fracture which was the way fracture occurred in the conventionally sintered samples. It indicated that grain boundaries were more strongly bonded than the grains themselves. Therefore, the compressive strength of the microwave sintered samples was assumed to be

increased. It is suggested that further work be done in this area using the hardness indentation technique or 3 point bend test to verify if this property is affected or not by microwave processing.

IV-6. Microstructure Analysis

Polished samples as shown in Figure 43 were cut from the microwave sintered and the conventionally sintered samples and thermally etched in air to reveal the microstructure. Scanning electron micrographs of samples thermally etched at 1050 °C for 5 hours are given in Figure 44 and that thermally etched at 1050 °C for 8 hours are given in Figures 45 and 46. Preliminary density analyses indicated that the microwave sintered samples had a smaller pore volume than the conventionally sintered samples as shown in Figure 43. It is due to better sintering and improved microstructure.

In the conventionally sintered sample, little densification occurred even after a relatively long processing time. As a result, the conventionally sintered samples retained the morphology of the initial powder particles as shown in Figure 45. Also, some zirconia particles had grown and exhibital rounded features. It was confirmed by Energy Dispersive X-ray Analysis (EDXA) in Figure 47 that the large grains were zirconia and small grains were zirconia and alumina in both processes.

The average grain size was determined by measuring an average linear intercept distance on the scanning electron micrograph of Figures 48 and 49, and then multiplying this by 1.558. The average

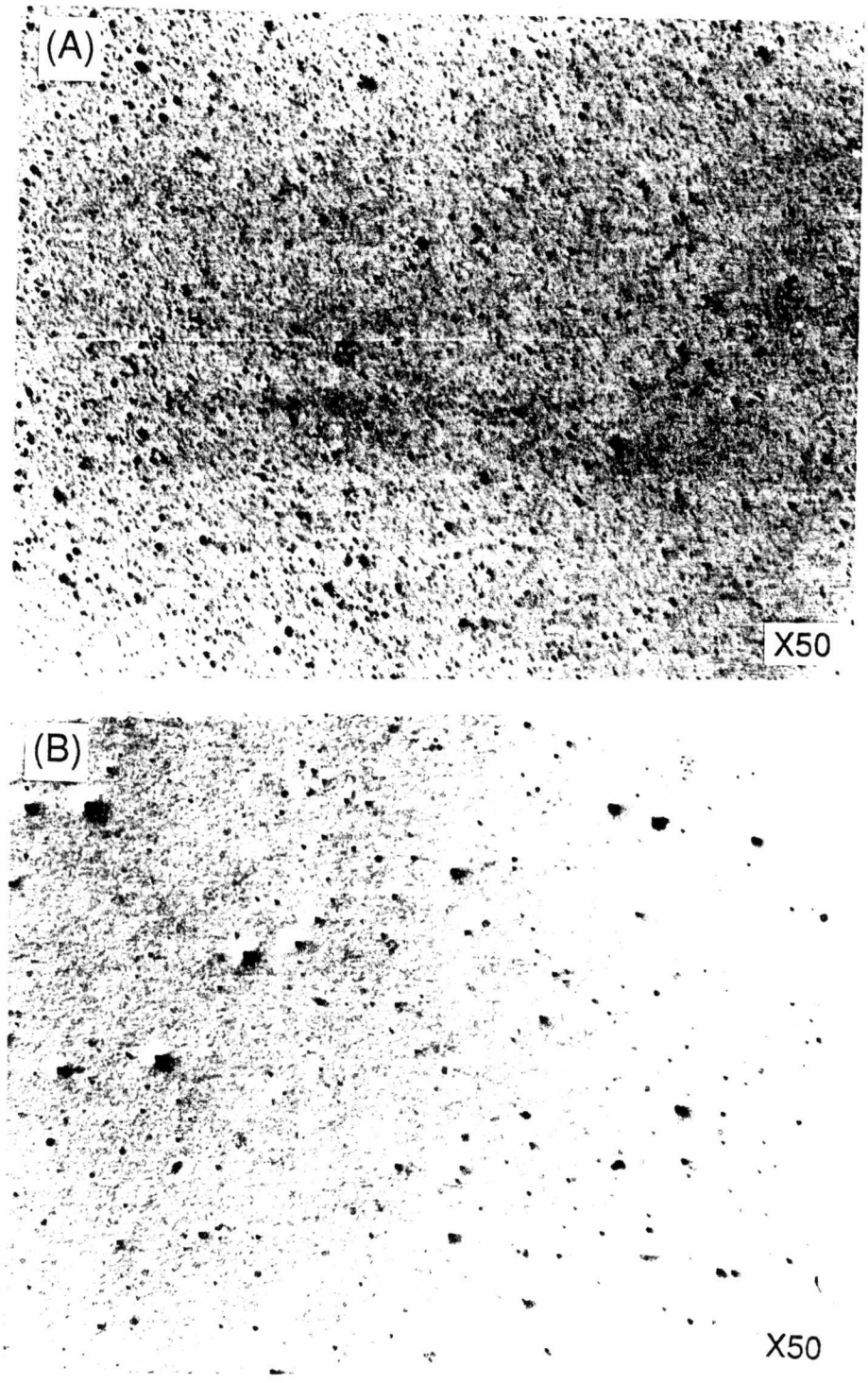


Figure 43. Polished surface of a zirconia-alumina composite; (a) conventionally sintered to 1350 °C in 108 hours and (b) microwave sintered to 1400 °C in 30 minutes.

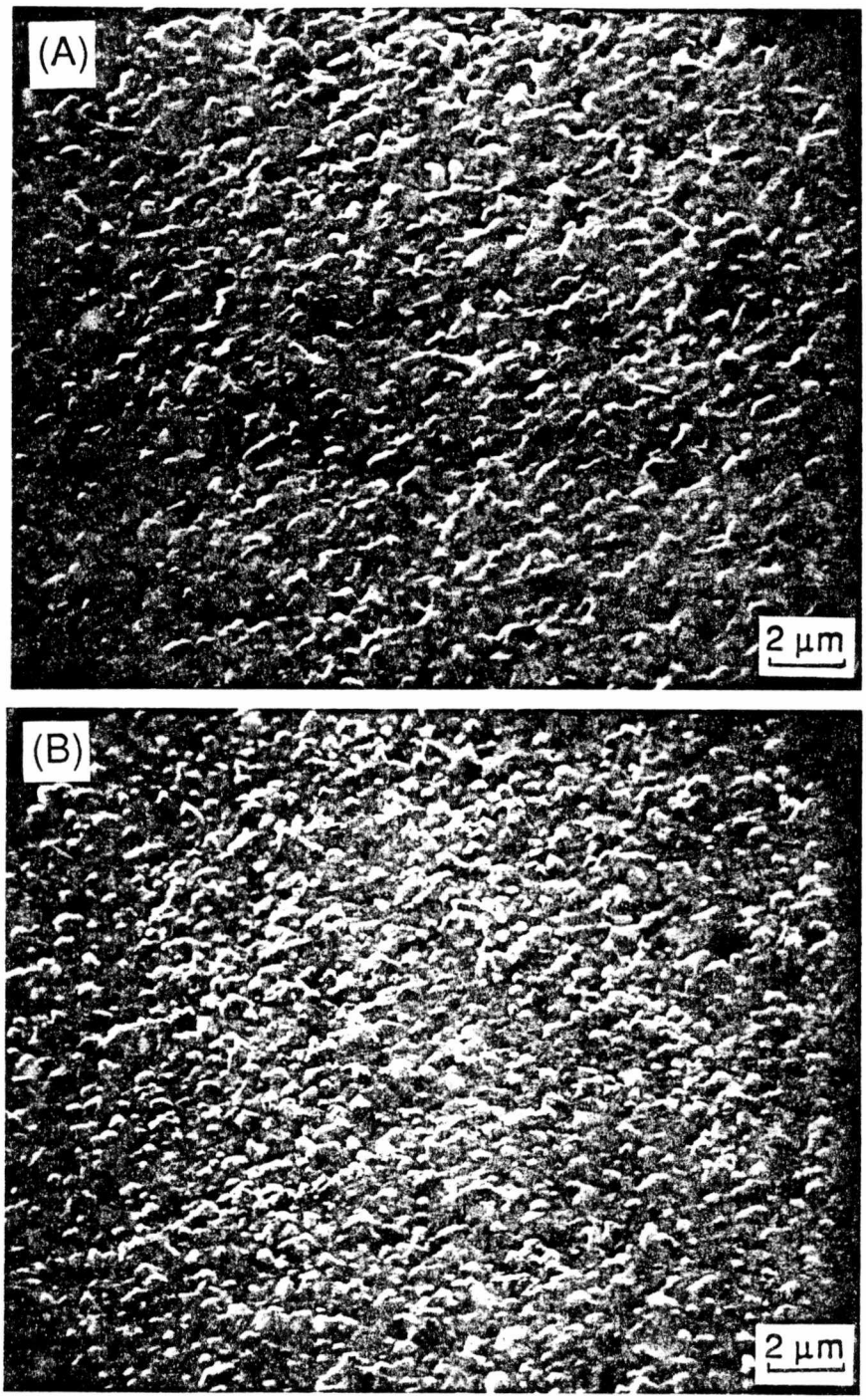


Figure 44. Scanning electron micrographs of polished and thermally etched surface of a zirconia-alumina composite at 1050 °C for 5 hours; (a) conventionally sintered to 1350 °C in 108 hours and (b) microwave sintered to 1400 °C in 30 minutes.

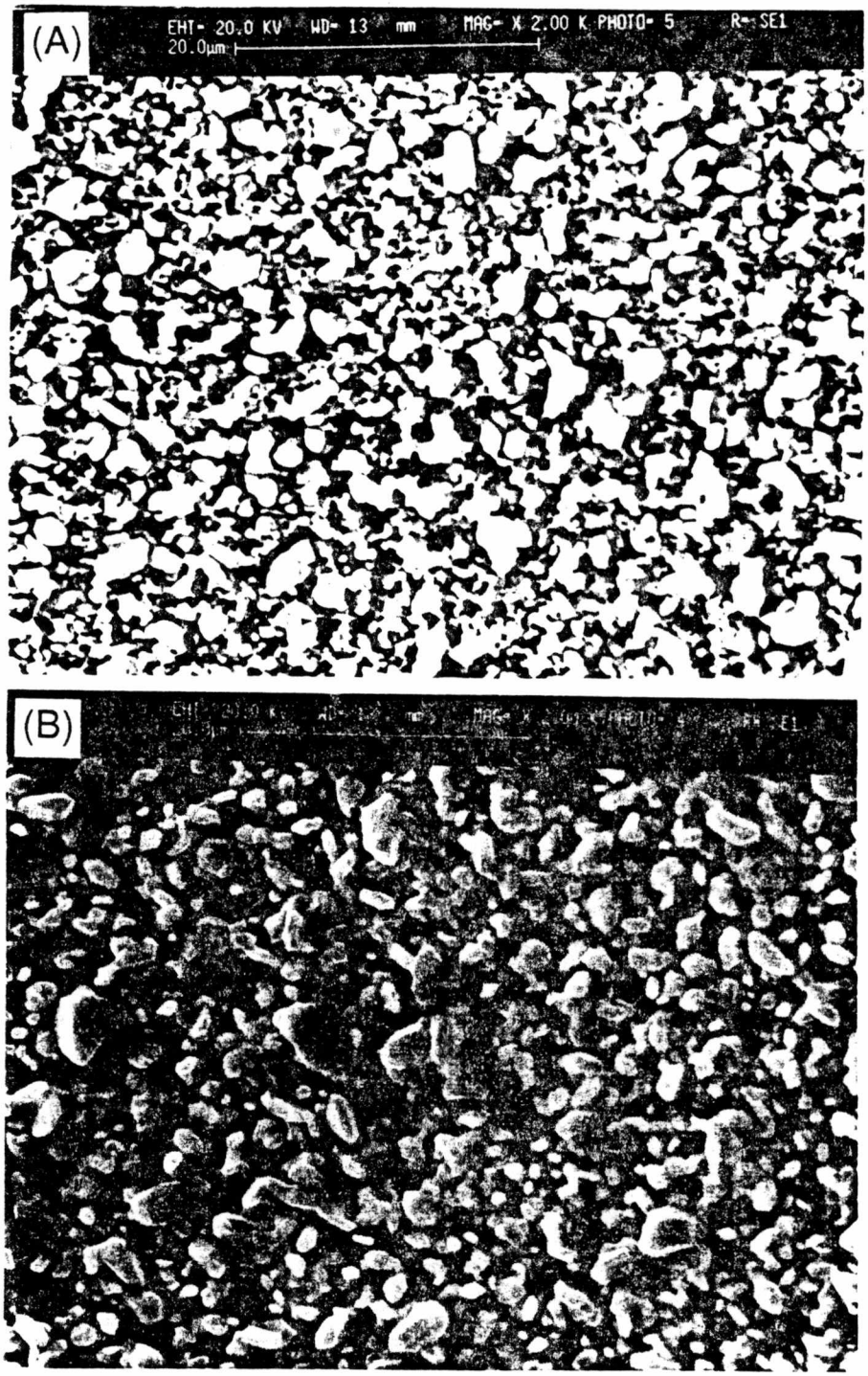


Figure 45. Scanning electron micrographs of polished and thermally etched surface of conventionally sintered samples at 1050 °C for 8 hours; (a) densification is 81.42% (x2,000), (b) densification is 84.44% (x2,000), (c) densification is 81.87% (x5,000), and (d) densification is 81.87% (x10,000).

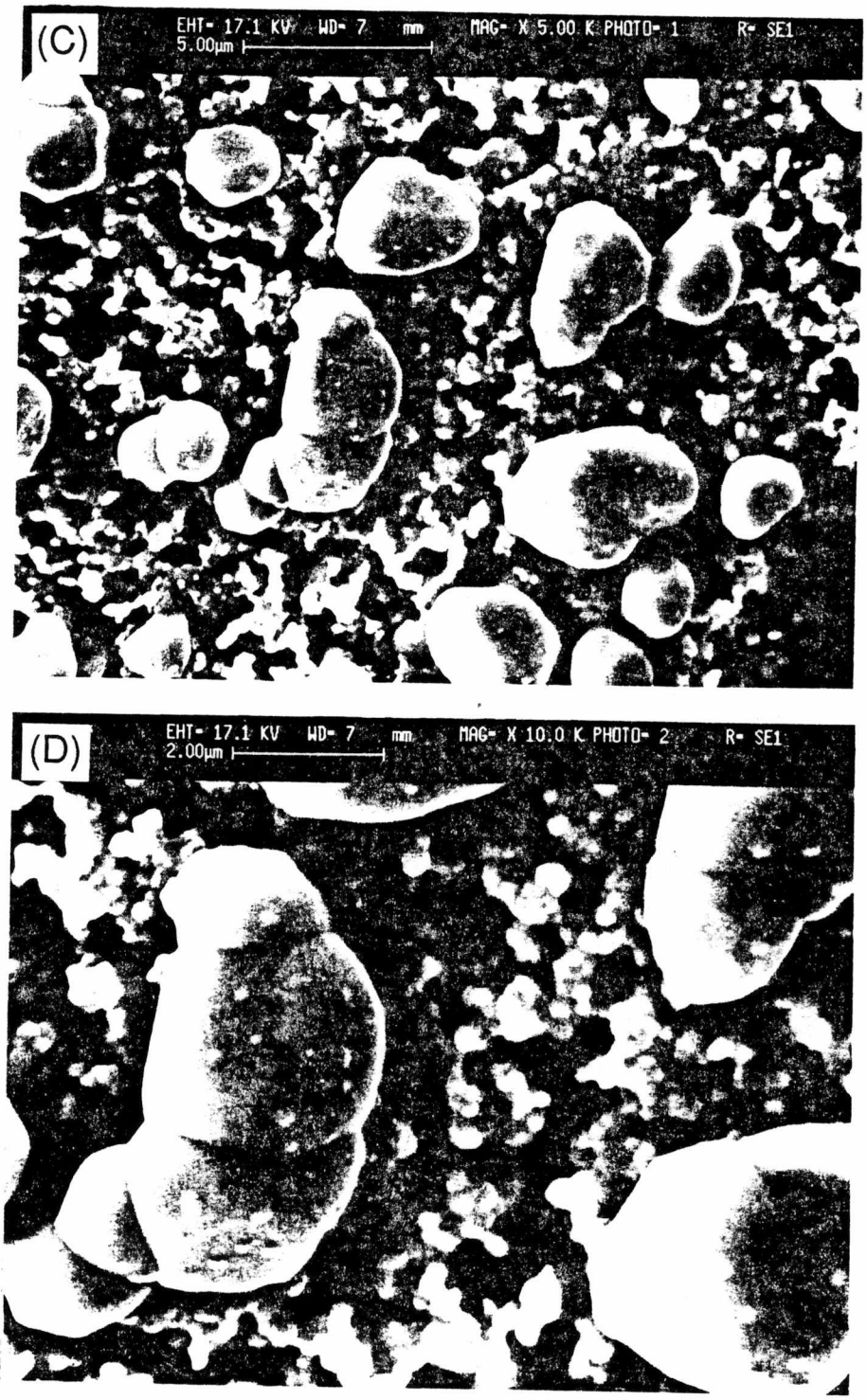


Figure 45. (Continued)

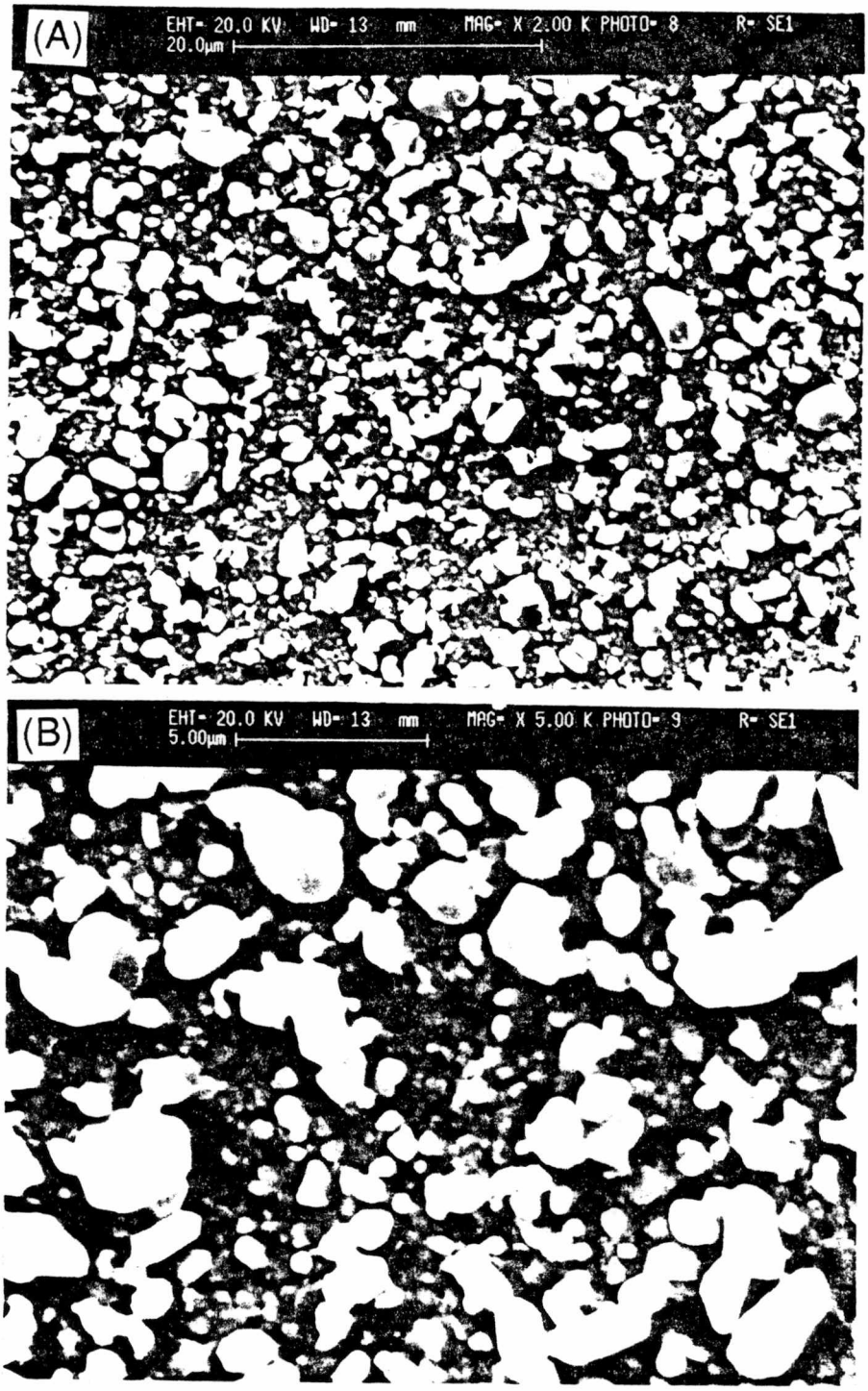


Figure 46. Scanning electron micrographs of polished and thermally etched surface of microwave sintered samples at 1050 °C for 8 hours; (a) densification is 99% (x2,000), (b) densification is 99% (x5,000), and (c) densification is 99% (x10,000).

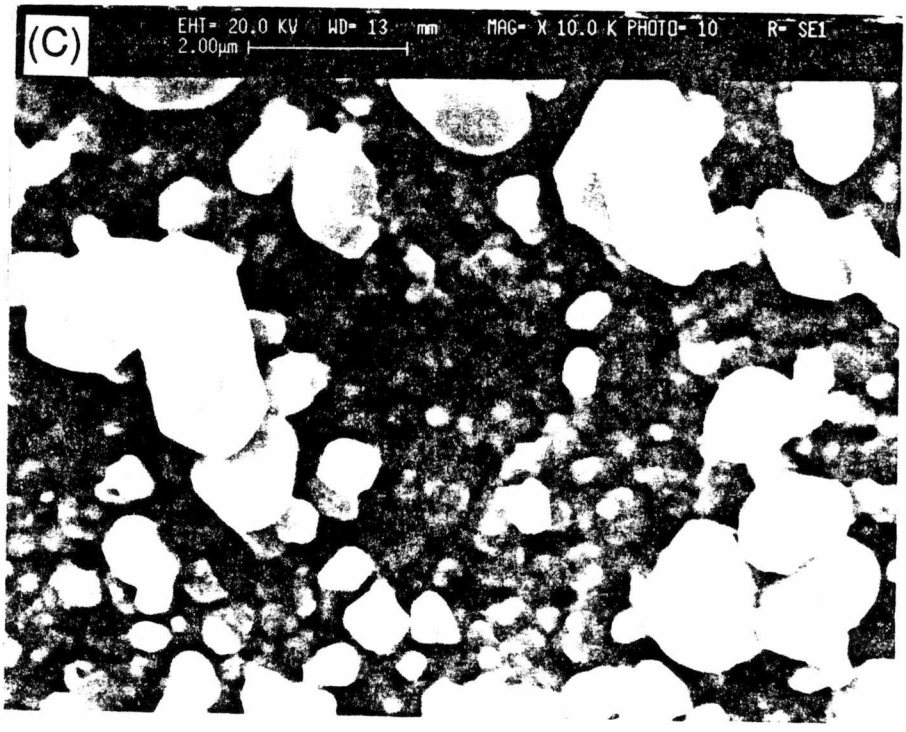


Figure 46. (Continued)

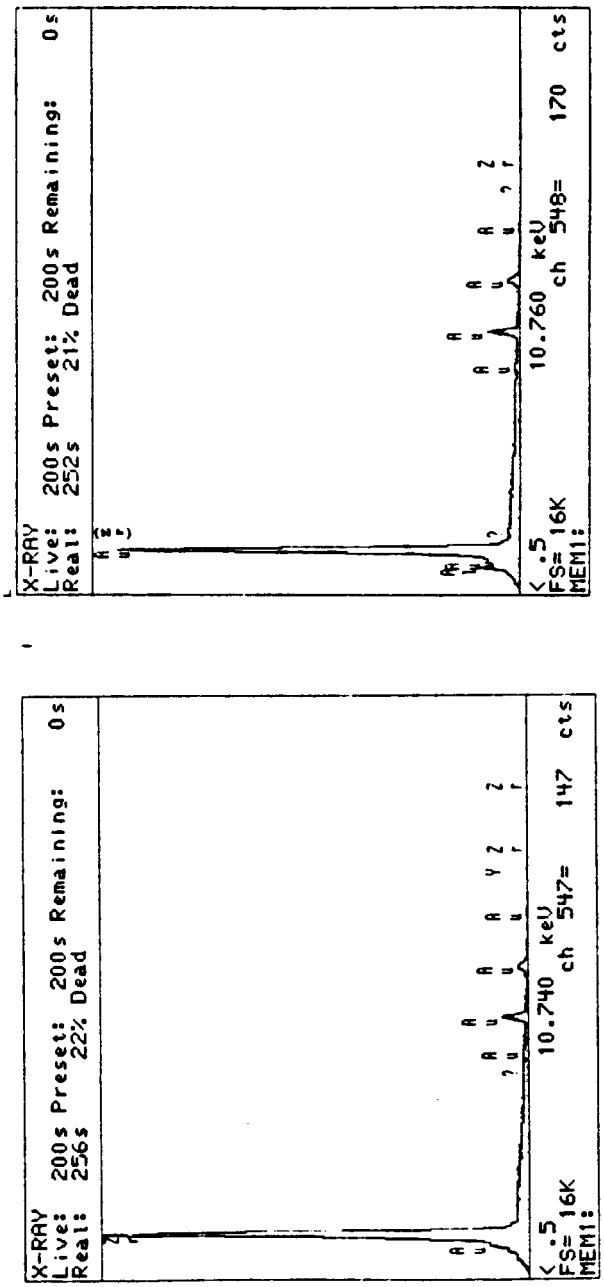


Figure 47. EDXA shows (a) large grains are zirconia and (b) small grains are zirconia and alumina.

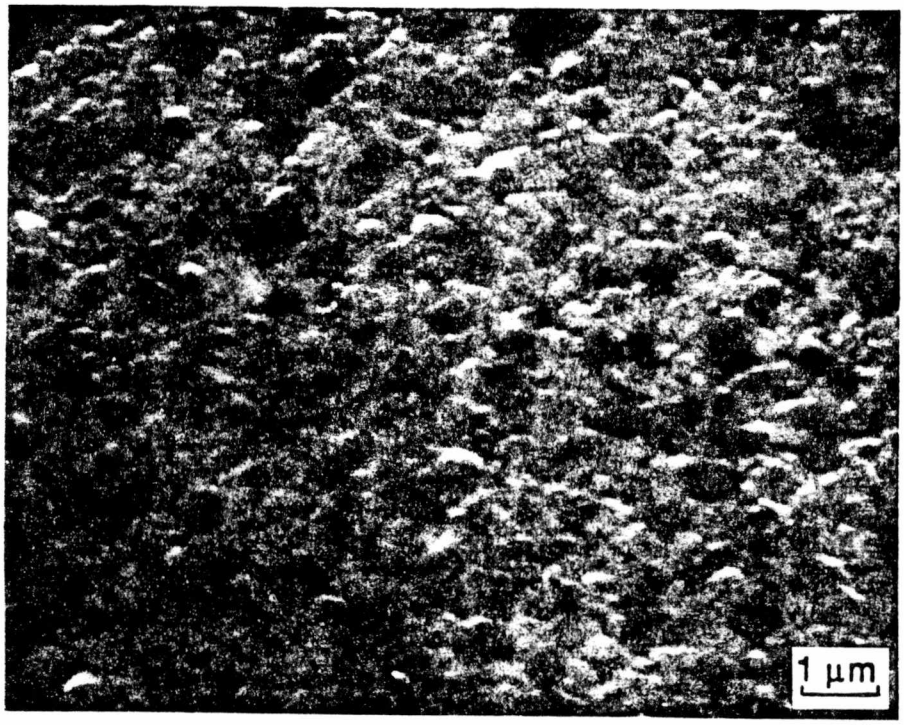


Figure 48. Scanning electron micrograph of polished and thermally etched surface of microwave sintered sample at 1050 °C for 5 hours.

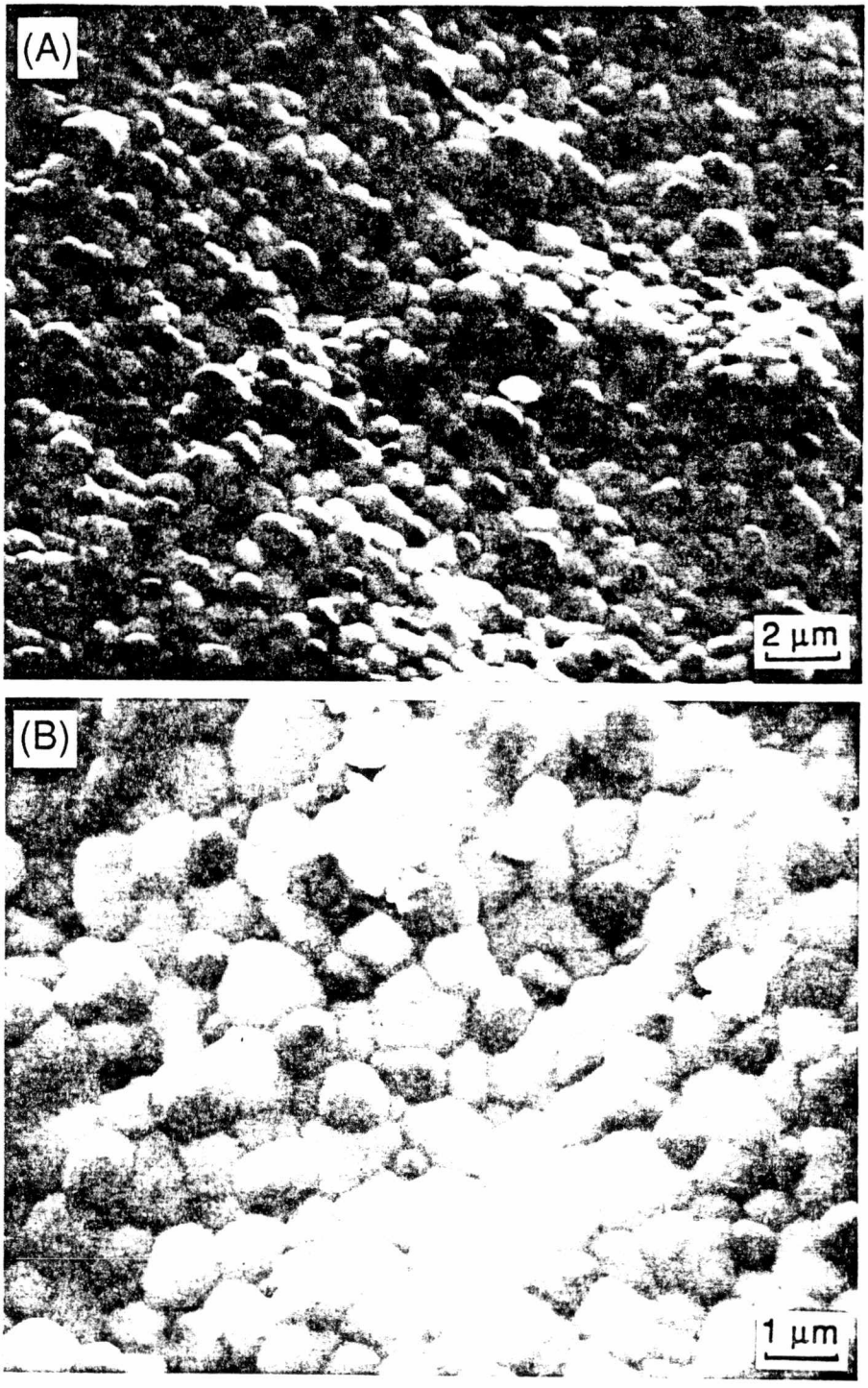


Figure 49. Scanning electron micrographs of fracture surface of microwave sintered sample; (a) x5,000 and (b) x10,000.

grain size in the polished and thermally etched microwave sintered sample was 0.41 μm and that in the fracture surface of the microwave sintered sample was 0.86 μm. In Figure 49 the white grains were zirconia and the gray ones were alumina as reported by Fukuhara (108). In conventional sintering, Rajendran (106) reported that average grain size of HIPed samples was 0.6 μm at 1450 °C, 0.65 μm at 1500 °C, 1.09 μm at 1600 °C, and 2.60 μm at 1700 °C in the sintering temperature. Wakai (106) reported that the as-HIPed sample showed equiaxed Al_2O_3 grains (about 0.8 μm) dispersed uniformly among the ZrO_2 grains (about 0.9 μm).

Therefore, the grain size of the microwave sintered sample was smaller than of the conventionally sintered sample because the penetration action of the microwave energy into the material resulted in the internal heating of large cross sections uniformly in a relative short period of time. As a result, microwave heating is assumed to have the shortest sintering time and fastest heating rate. It was resonable to adopt Brook's theory to give a general explanation for the results of the smaller grain size for the microwave sintering. Because the heating rate was higher than conventional processing, the sample passed more rapidly through the low temperature regime where surface diffusion was relatively more important, and the small grained microstructure was raised to a high temperature where grain boundary and lattice diffusion predominate over surface diffusion. The ability for fast firing to produce high quality microstructures has been demonstrated (37,45,46,47). Also, there was no evidence of exaggerated grain growth, probably

because of the short time duration of the high temperature sintering.

In order to understand different fracture behavior between the microwave sintered and the conventionally sintered samples, fracture microstructures of samples were analyzed. Figures 50-56 show scanning electron micrographs of fracture surface of samples processed by conventional and microwave heating.

Figure 50 shows a conventionally sintered sample, little densification occurred even after a relatively long processing time. The fracture was intergranular fracture, indicating grain-to-grain separation. Intergranular fracture is typical of the highly monoclinic materials, suggesting that the crack path follows the intergranular microcracks produced during fabrication as a result of the phase transformation. This material is quite friable (113).

A typical fracture piece of the microwave sintered sample is shown at x50 magnifications in Figure 51. According to the different fracture area, scanning electron micrographs are shown in Figures 52-56. The fracture behavior was unusual in that very little intergranular fracture was seen. Transgranular (with obvious cleavage steps) regions are common, indicating grain-to-grain bonding. The irregular fracture topography of individual grains might be a result of the crack interacting with the complex internal structure of the twinned monoclinic grains which transformed ahead of the propagating crack as reported by Lange (121), or it may be the result of the crack being inhibited by the melted pore surface, and of the wetting of melted alumina.

In Figures 53, 54, and, 56, transgranular fracture was observed

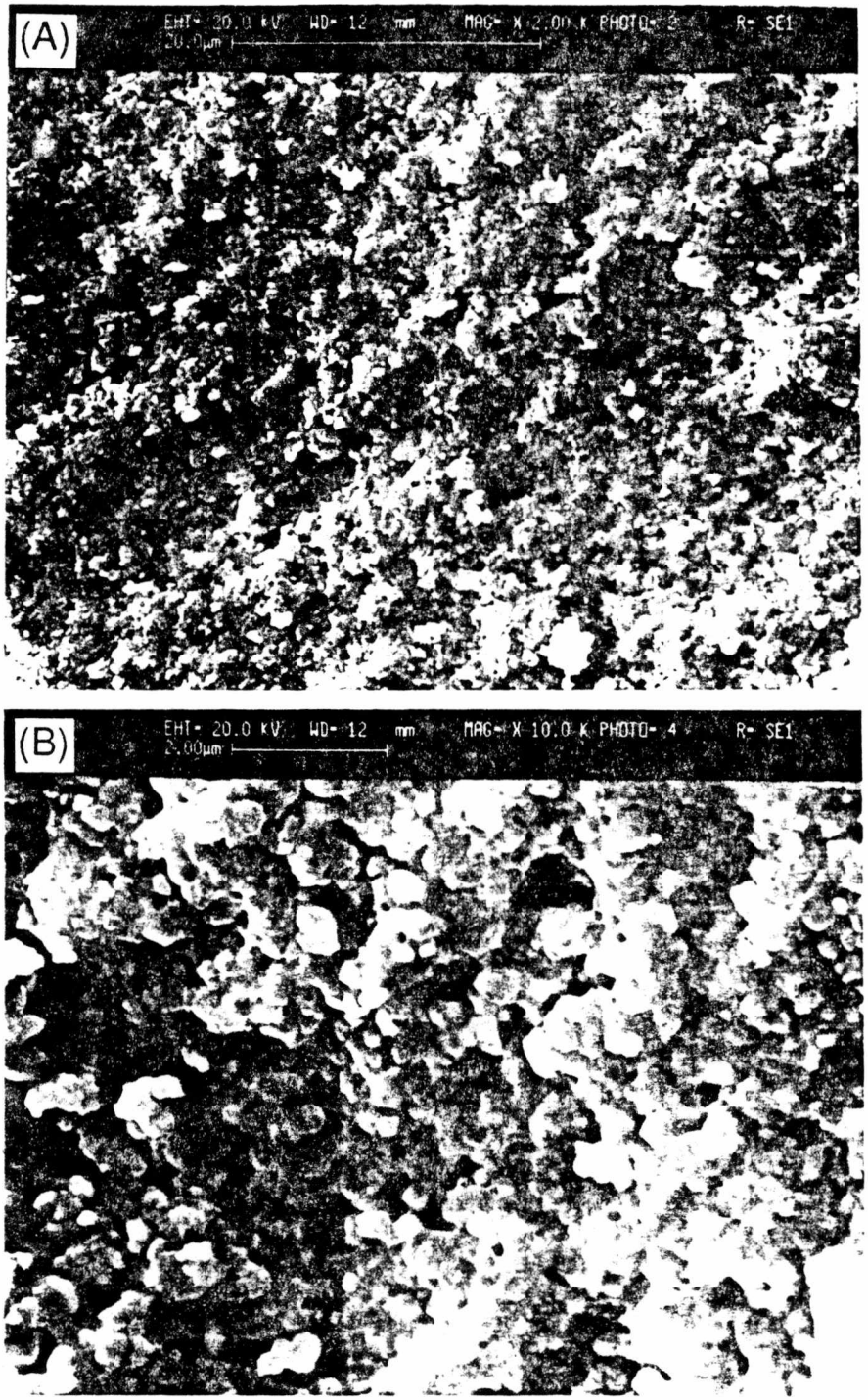


Figure 50. Scanning electron micrographs of fracture surface of conventionally sintered sample at 1350 °C for 108 hours; (a) x2,000 and (b) x10,000.

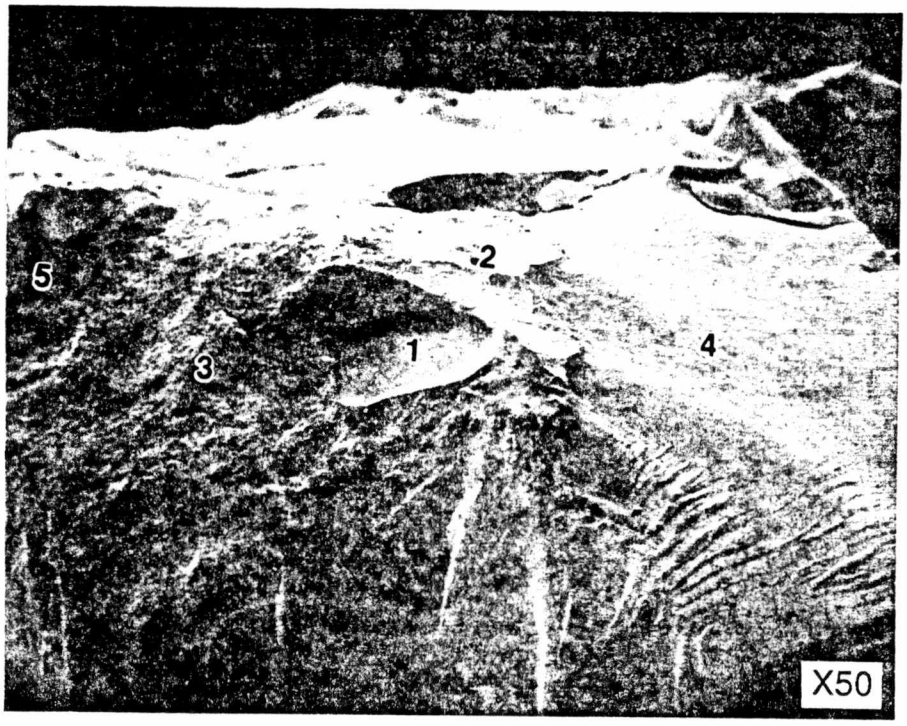


Figure 51. Scanning electron micrograph of fracture surface of microwave sintered sample at 1400 °C for 30 minutes.

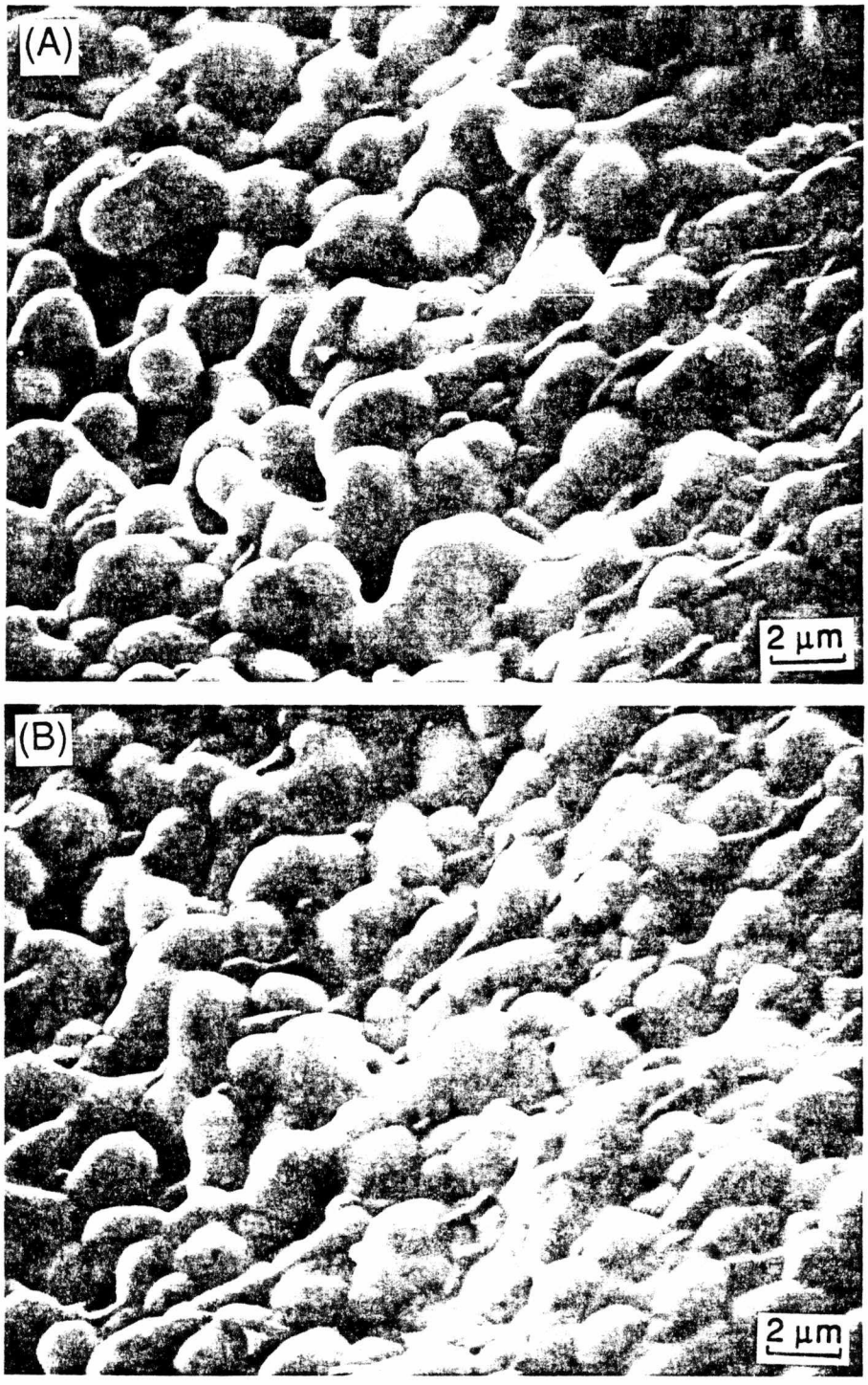


Figure 52. Scanning electron micrographs of fracture surface of microwave sintered sample at area 1; (a) x5,000 and (b) x5,000.

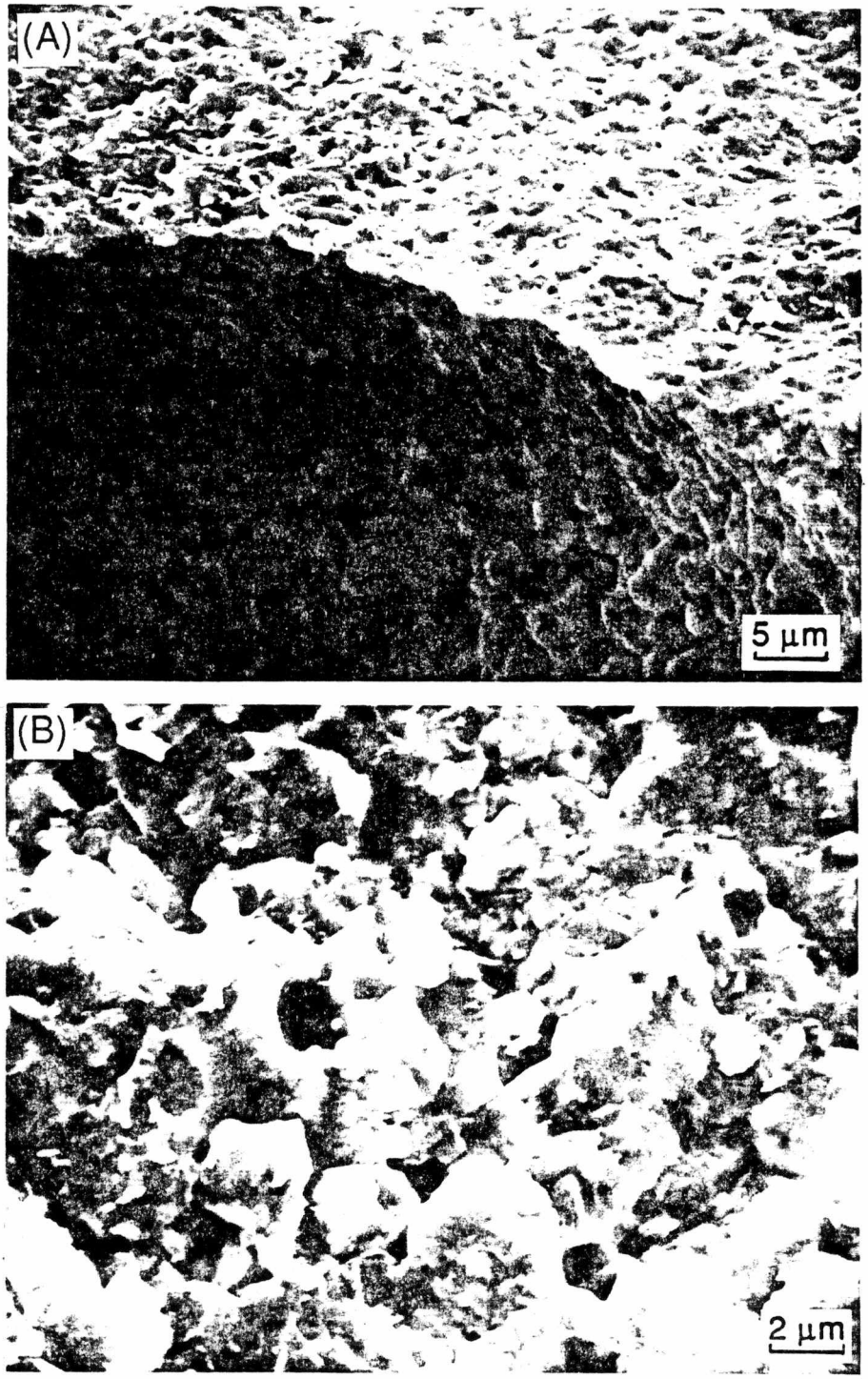


Figure 53. Scanning electron micrographs of fracture surface of microwave sintered sample at area 2; (a) x2,000 and (b) x5,000.

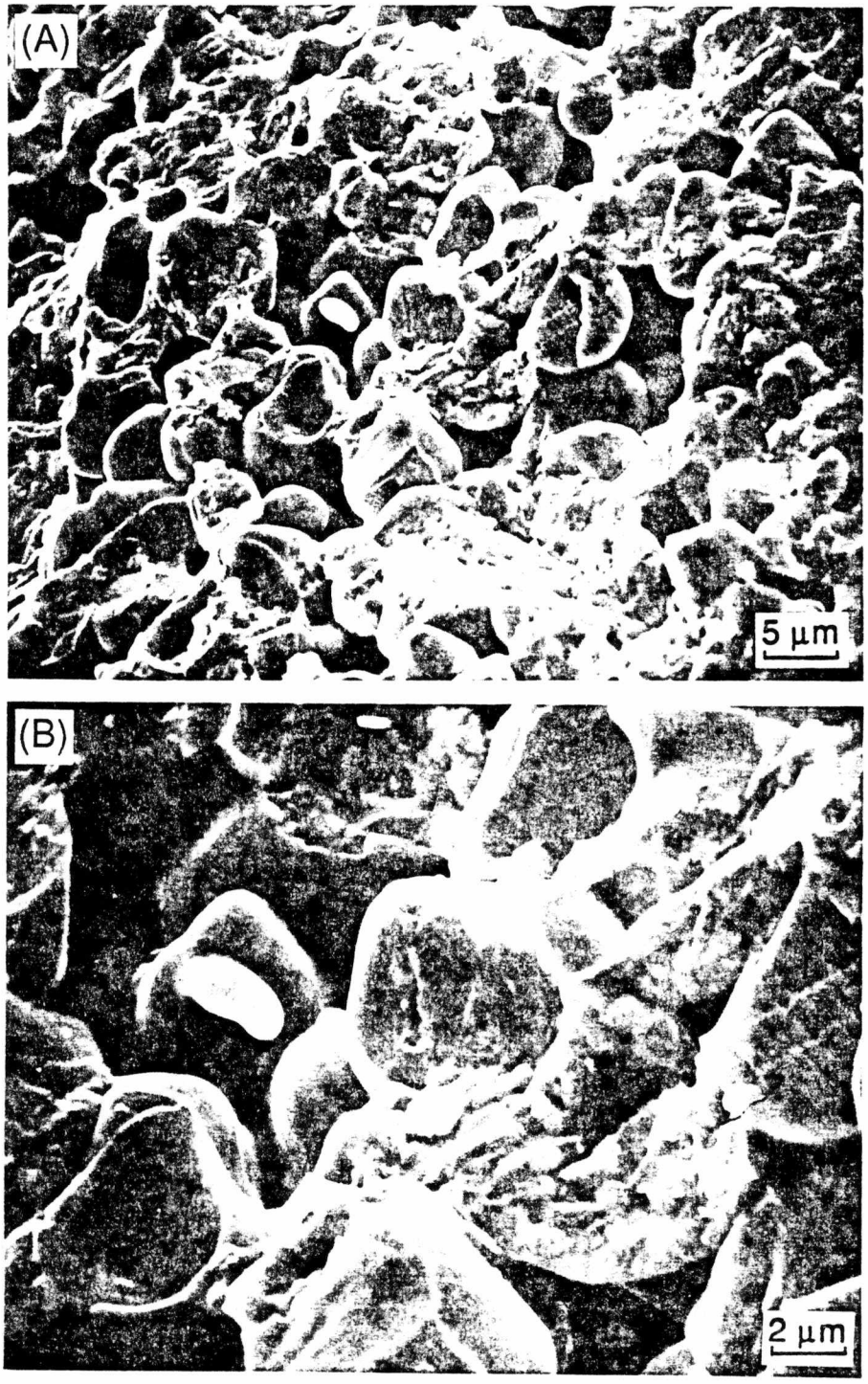


Figure 54. Scanning electron micrographs of fracture surface of microwave sintered sample at area 3; (a) x2,000 and (b) x5,000.

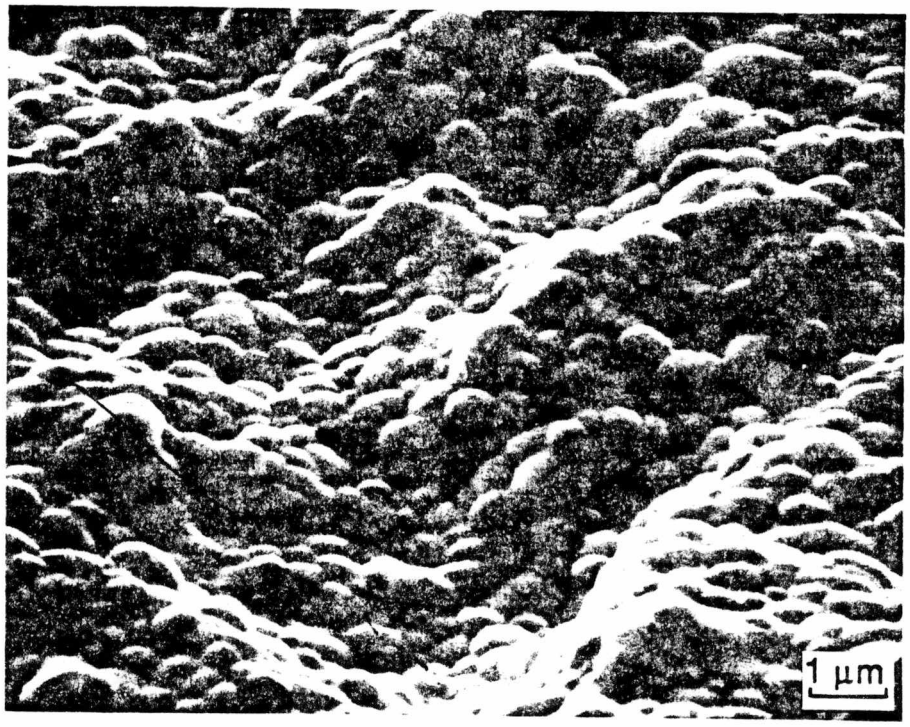


Figure 55. Scanning electron micrographs of fracture surface of microwave sintered sample at area 4; x10,000.

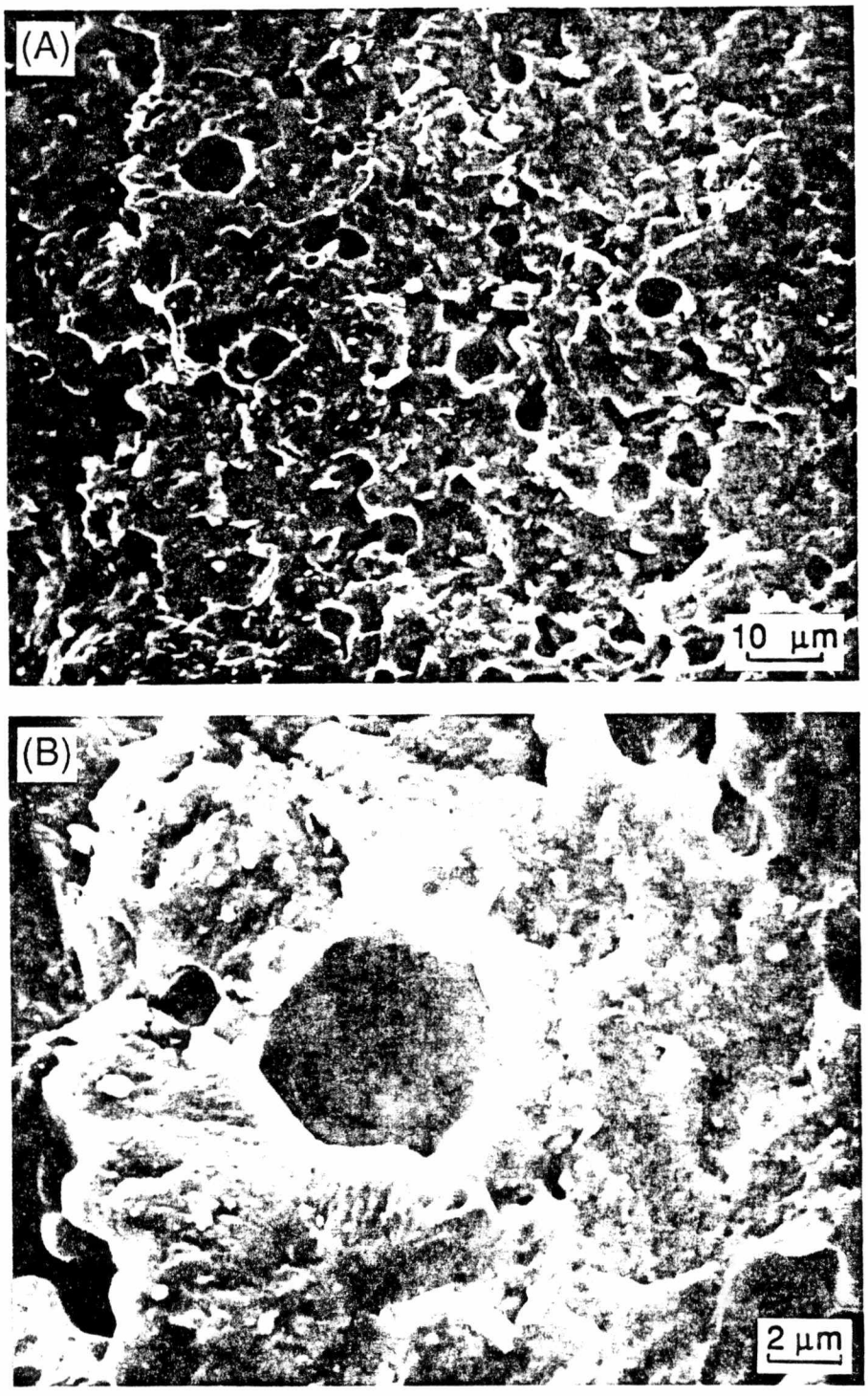


Figure 56. Scanning electron micrographs of fracture surface of microwave sintered sample at area 5; (a) x1,000, (b) x5,000, (c) x5,000, and (d) x1,000.

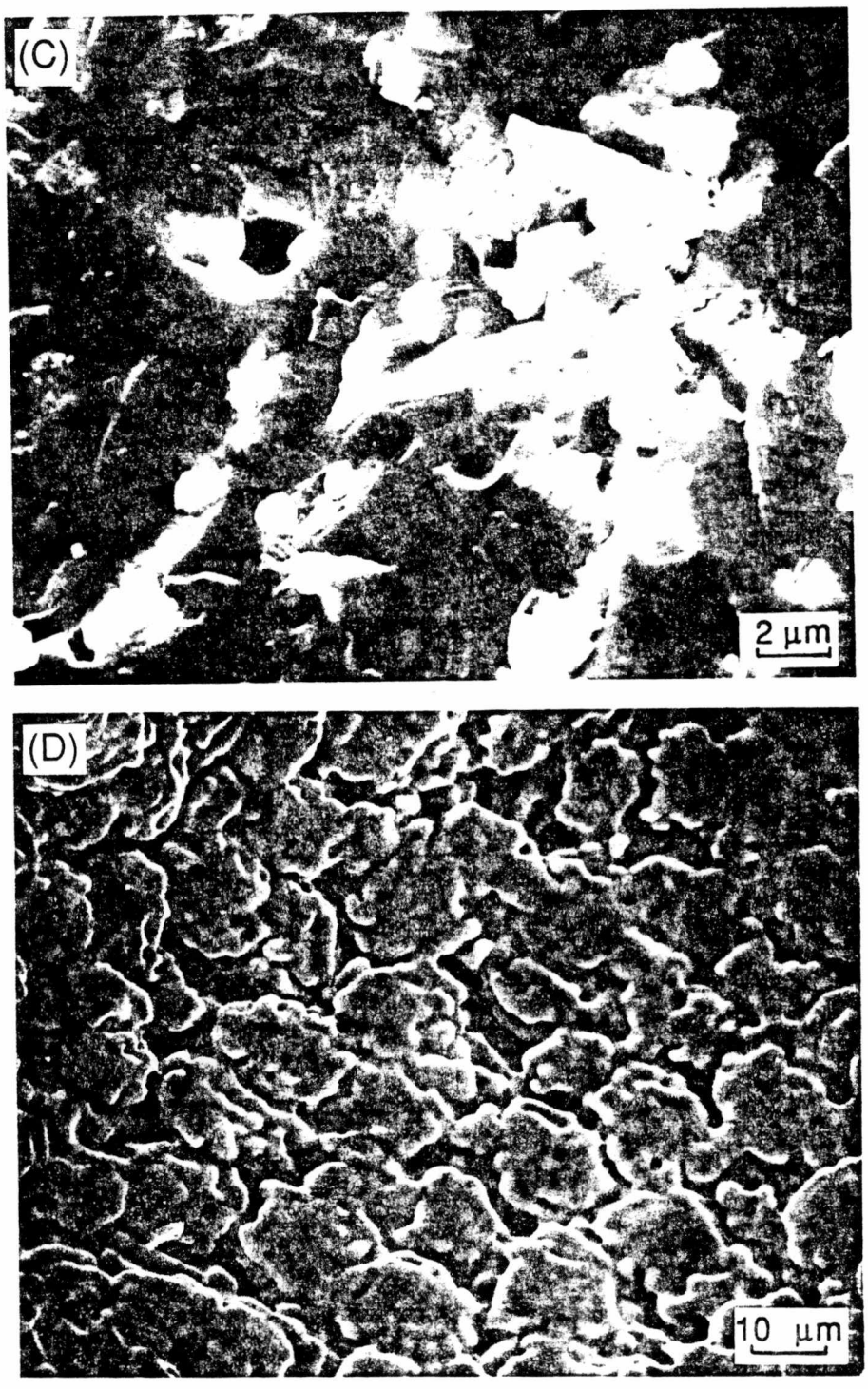


Figure 56. (Continued)

rather than fracture along grain boundaries indicating that the grain boundaries were more strongly bonded than the grains themselves. In Figures 52, 55, and 56 (d), zirconia-alumina wetting was a predominant bonding mechanism, more strongly bonded than the grains themselves. Wetting was believed to be caused by the formation of a liquid phase alumina when the real temperature exceeded the melting temperature of an alumina due to thermal runaway. Butler (97) and Rajendran (98) reported that the electrical conductivity of the zirconia-alumina composite was improved as a consequence of the grain boundary glass phase accumulated at the Y-PSZ/Al_2O_3 interfaces. It is assumed that the electrical conductivity of the microwave processed samples may be higher than for the conventionally processed samples due to a wetting mechanism along grain boundaries in microwave heating.

Also, the melted pore surface could act as a crack inhibitor during the fracture thus causing the transgranular fracture observed rather than intergranular fracture. This type of fracture behavior has been observed in microwave sintered Al_2O_3 and in ZrO_2 sintered at 2.45 and 60 GHz (24,120). The fracture surface in Figures 54 and 57 is more smooth than that in Figures 53 and 56. The reason may be that microcracks are present in the sample due to the high heating rate as reported by Lange (121).

Of interest is a better understanding of how the grain-to-grain bonding may be effected by the concentration of the electric field intensity between the grains. If sintering in an electromagnetic field occurs as described in an earlier paper by Meek (22), then the

following explanation may describe the bonding mechanism and wetting along grain boundaries. If the initial electric field intensity is greater in the lower dielectric constant regions, the electric field intensity and power density between zirconia and alumina grains will be greater than in the grains themselves, and thus heating will concentrate at grain boundaries. Once dense regions begin to form, the microwave field will couple more strongly to the other low density regions. With further densification, this energy partitioning will cease, since the microstructure will become uniform.

It was evident that the grains are equiaxed and uniform in Figures 54 and 55. In addition, it was observed that a significant gradient in grain size did not occur from the outer surfaces to the interiors of the samples. It might be suspected that such a radial variation would exist since the extremely rapid heating rates would cause the temperature of the sample interiors to lag significantly behind those of the surfaces. However, the absence of a grain size gradient was taken as evidence that the microwave heating was uniform heating due to volumetric heating.

The grain size of the microwave sintered sample at 1400 °C for 30 minutes was larger than that of the microwave sintered sample at 1800 °C for 45 minutes even though the former had a lower sintering temperature and shorter time as shown in Figure 57. The reason was that the latter apparently was sintered at a higher heating rate, 50 °C/min., while the former was at 22 °C/min.

Brook (45-47) has shown that rapid heating led to improved microstructures with finer and more uniform grain size. Therefore,

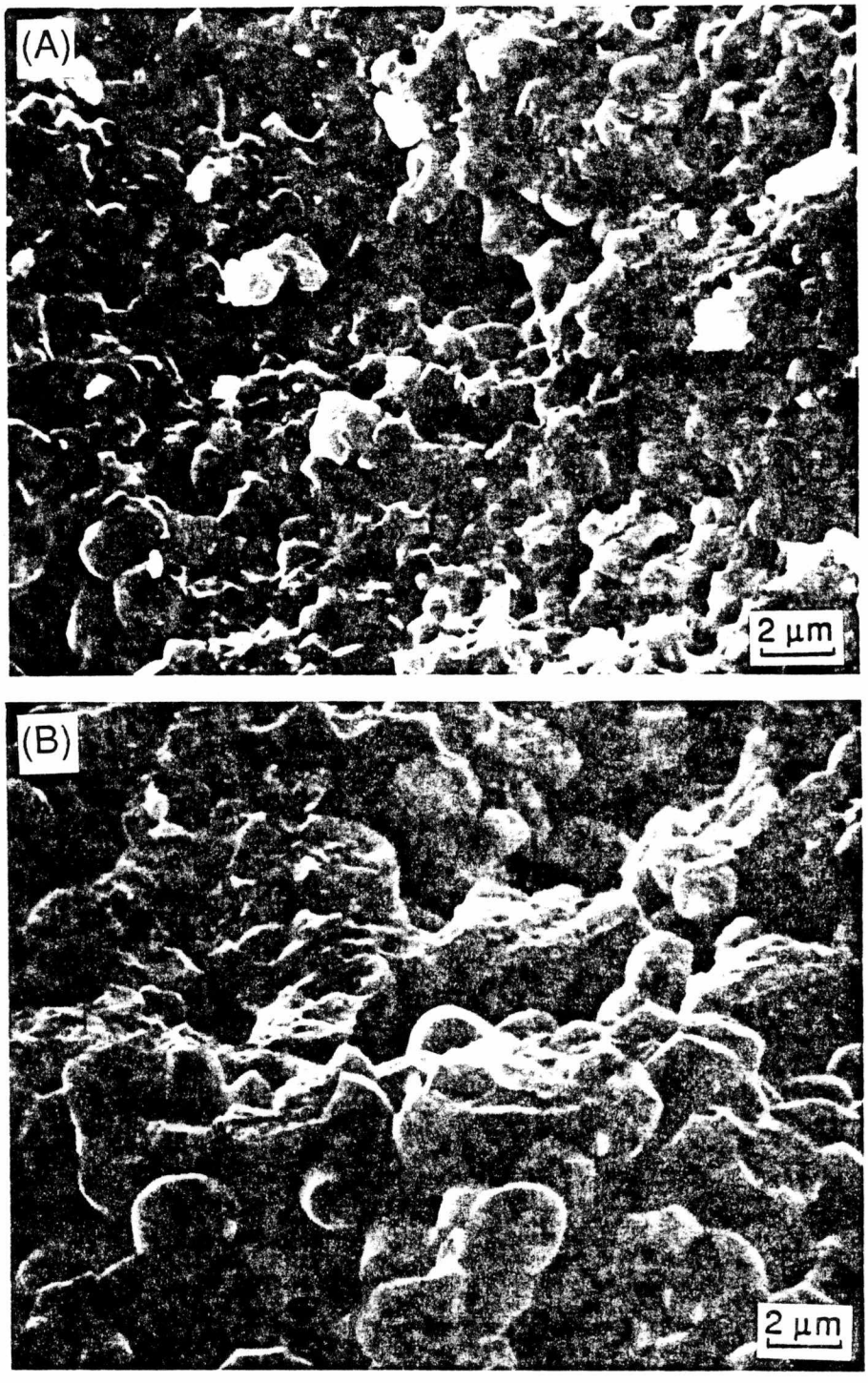


Figure 57. Scanning electron micrographs of fracture surface of microwave sintered sample; (a) at 1800 °C for 45 minutes and (b) at 1400 °C for 30 minutes.

similar results are expected because of the different heating rates seen for microwave processing. It means that rapid heating to high temperature could activate grain boundary and lattice diffusion before surface diffusion has a chance to substantially coarsen the microstructure and therefore lower the driving force for densification. Apparently, grain size may be a stronger function of heating rate than temperature.

Figures 58 and 59 show the microcracking in the fracture surface of the microwave sintered sample. Especially, Figure 59 shows the serious microcrackings in the melted pore surface of the microwave sintered sample. It is assumed that the observed microcracks were due to the rapid heating and cooling rate and that these degrade the materials' mechanical properties. Therefore, to prevent microcracks during heating, the rapid heating rate may be decreased moderately or low thermal conductivity materials changed to high thermal conductivity materials. The temperature gradient inside a low thermal conductivity material is always raised to the surface temperature due to heat transfer and internal heat conduction during the microwave sintering process. Reduction of this temperature gradient is important for microwave heating of low thermal conductivity materials. Increased thermal conductivity may be achieved by reducing the degree of initial porosity of the material. Equation II-10 indicates that the heating rate is directly proportional to the square of the electric field. The heating rate may be decreased by decreasing input power as soon as the material begins to couple.

In Figure 59, some grains were melted along grain boundaries as

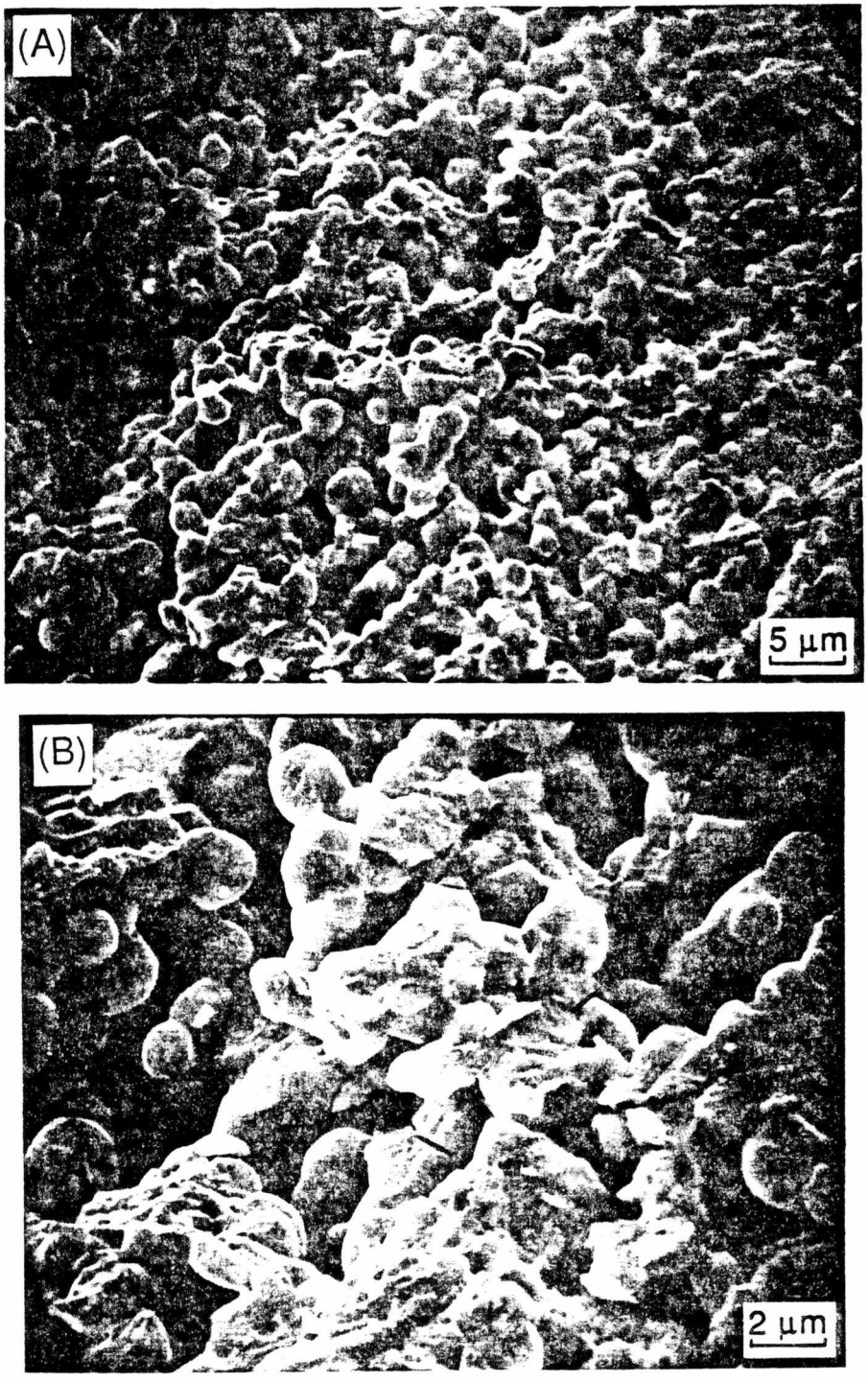


Figure 58. Scanning electron micrographs of fracture surface of microwave sintered sample; (a) x2,000 and (b) x5,000.

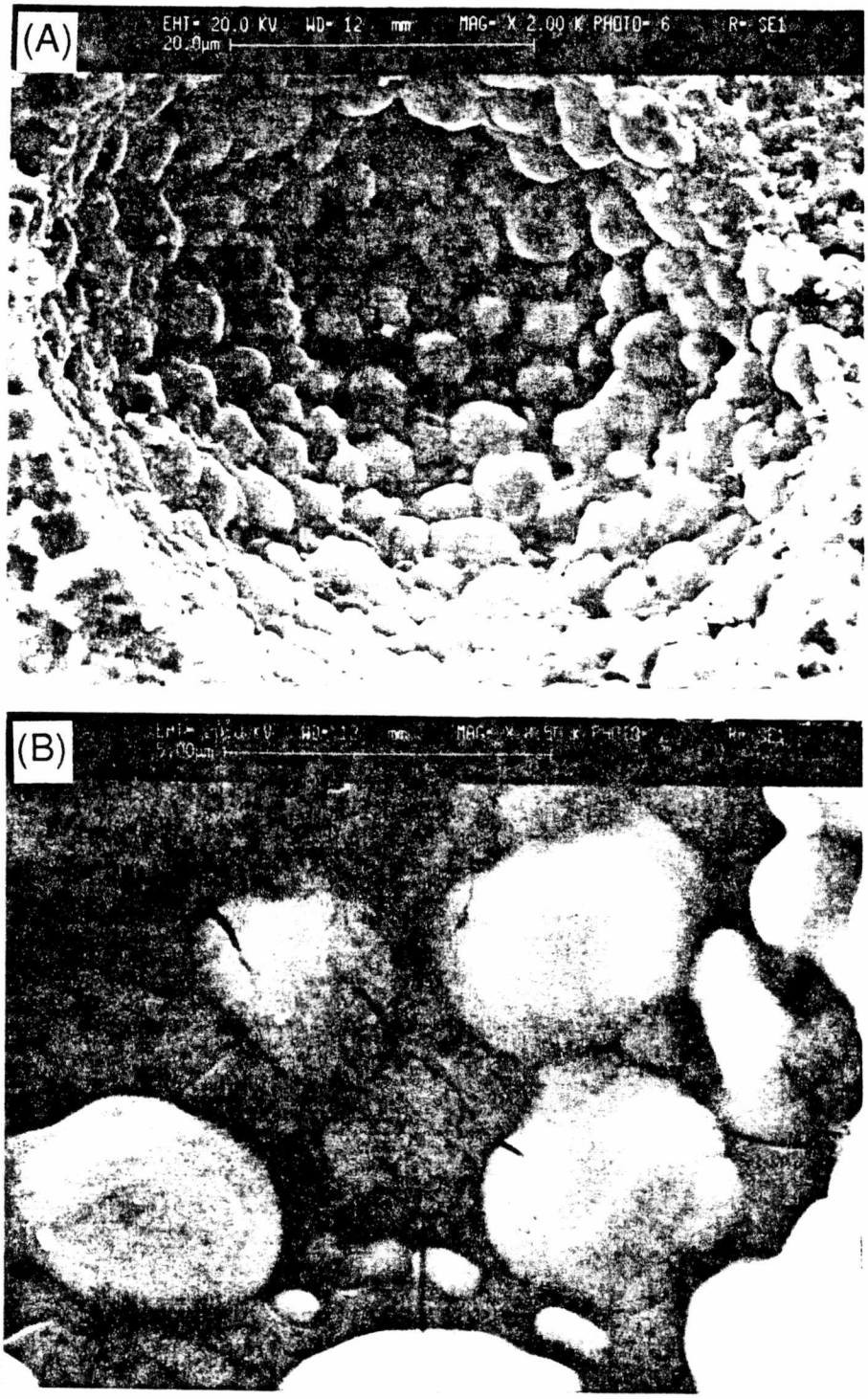


Figure 59. Scanning electron micrographs of fracture surface of microwave sintered sample; (a) x2,000 and (b) x8,500.

shown in Figures 52 and 55, which resulted in zirconia-alumina wetting. Its composition was determined by Energy Dispersive X-ray Analysis (EDXA) as shown in Figure 60. The wetted regions were alumina and the grains were zirconia. These results indicated that the real microwave sintering temperature was higher than the measured surface temperature because the melting point of alumina is 2045 °C and the measured sintering temperature was 1400 °C. Thus, the measured temperature by an IR meter corresponded to the surface temperature which was lower than the internal temperature in microwave heating. It indicated that the optical pyrometer could not correctly measure a local temperature within the material. To measure the temperature in microwave heating, it is necessary to measure the accurate temperature by using a non-invasive technique as proposed by Meek (118).

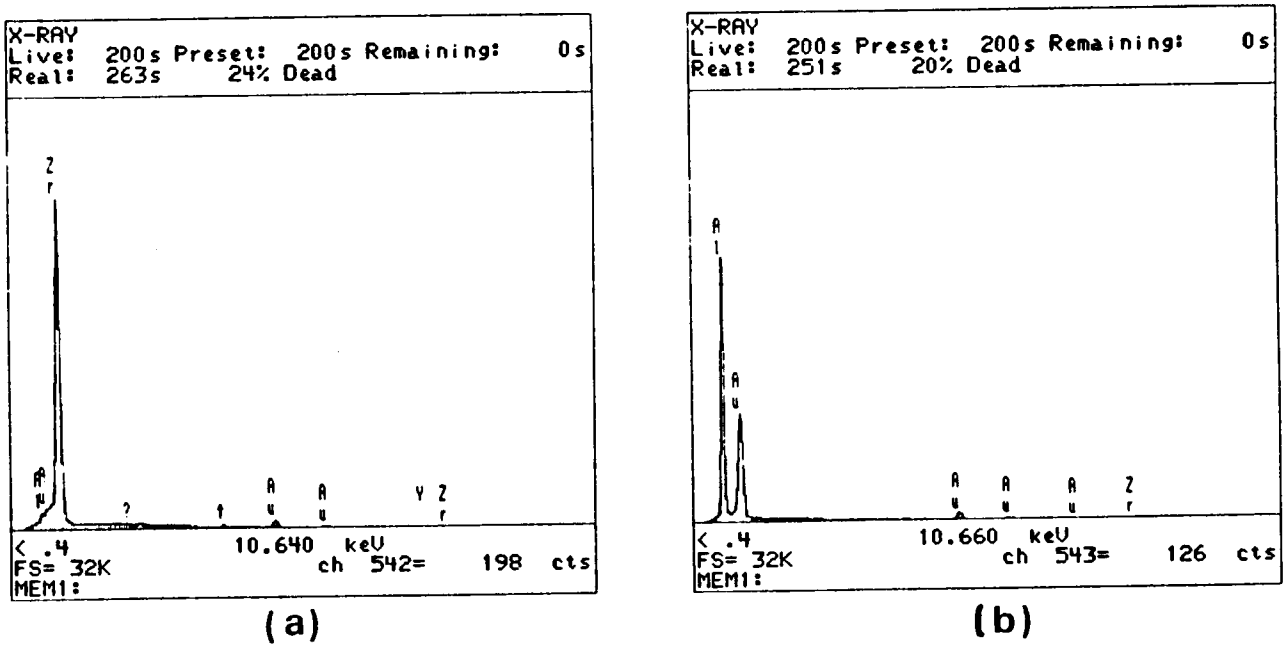


Figure 60. EDXA shows (a) grains are zirconia and (b) wetted regions are alumina.

CHAPTER V
CONCLUSIONS

Based on experiments characterizing a zirconia-alumina composite sintered using 2.45 GHz microwave radiation, the following conclusions have been reached.

For a given temperature, the required input power from the microwave generator could be minimized by adjustment of the single-stub tuner to minimize the reflected power. Microwave heating under optimum heating conditions maximized the temperature range that could be achieved with a given microwave system.

Microwave heating may be described as a three-step process, namely 1) preheating, 2) transition, and 3) stable sintering. Microwave radiation initially coupled with insulation or a susceptor until the samples reached a temperature between 700 and 1100 °C because of the sample low-dielectric loss in these temperature ranges. After the samples heated to between 700 and 1100 °C, they began to couple efficiently and then the temperature of the samples began to increase rapidly. Thermal runaway was prevented by careful control of input power. After a few minutes uniformly heated samples were formed. As a result, it was postulated that the critical temperature in the samples was about 700 to 1100 °C and the degree of microwave coupling was dependent on the temperature of the samples if they had been heated although they were considered to be microwave transparent at ambient temperature. Therefore, it

was extremely difficult to control the heating without a knowledge of the distribution of microwave energy in the cavity under load conditions and also the coupling effects of the power source with the loss factor of the load.

The total field within the sample was related to the position of the peak of the exciting field relative to the sample because the field excited was a standing wave. Since the amount of heating in the sample depended upon the total field, the efficiency of energy conversion depended upon the position of the peak of the exciting field. It is thought that the surface temperature of the sample was lower than the center due to internal heat generation and thermal losses at the surface. Radiation, conduction, and convection losses from the surface of the sample were the principle thermal losses.

The density of the microwave processed samples was over 95 %TD at any sintering temperature and time, but the maximum density of the conventionally processed samples was 92.59 %TD at 1350 °C for 108 hours. The enhanced densification was most likely the result of the extremely fast heating rate achievable by microwave heating. Also, enhanced diffusion appeared to be responsible for the accelerated densification rates. In other words, the activation of grain boundary and lattice diffusion occurred before surface diffusion could significantly coarsen the microstructure.

The fraction of the monoclinic-phase zirconia was found to be approximately 28 % in the conventionally sintered samples and almost 0 % in the microwave sintered samples. It was concluded that the material was heated uniformly without temperature gradients on

a macroscopic scale during microwave heating and that the bulk regions of each grain maintained a temperature low enough to avoid the tetragonal to monoclinic phase change.

The thermal-shock resistance of the conventionally sintered and the microwave sintered samples was approximately the same. This is not the same conclusion reached in an earlier paper and may be due to processing of the green samples. In the present work samples were prepared by cold pressing while in the work reported by Holcombe (120) samples were prepared by isostatic pressing. The isostatically pressed samples sintered much more uniformly than the cold pressed samples. However, the thermal-shock property of the microwave sintered samples may be improved because each pore melted as shown in SEM micrographs and this may act as a crack inhibitor enhancing the thermal shock. Further work needs to be done to complete the observed thermal-shock property by using the hardness indentation technique or 3 point bend test and making samples having no microcracks by utilizing a rapid heating rates.

The average grain size of the microwave sintered sample was smaller than of the conventionally sintered sample because of the penetration action of the microwave energy into the material. This resulted in the internal heating of the material in a relatively short period of time due to a very rapid heating rate.

The grain boundaries were more strongly bonded than the grains themselves in the microwave sintered samples due to a wetting mechanism. As a result, transgranular fracture was usually observed rather than fracture along grain boundaries. Of interest

was a better understanding of how the grain-to-grain bonding would be effected by the concentration of the electric field intensity between the grains.

If sintering in an electromagnetic field occurred as described in Meek's microwave heating theory (22), a wetting mechanism along grain boundaries and melted pore surface may be described as follows: If the initial electric field intensity is greater in the lower dielectric constant regions, the electric field intensity and the power density between zirconia and alumina grains are greater than in the grain boundaries. Once dense regions began to form, the microwave field couples more strongly to the other low density regions. With further densification, this energy partitioning ceases, since the microstructure has become uniform.

For future research, the following thoughts are presented;

1) Incorporate a programmable temperature controller in the microwave unit, since manual control is inadequate.
2) Investigate the power density gradients in the reaction cavity for more uniform heating.
3) Measure the dielectric constant and loss tangent of the material as a function of temperature.
4) Apply some non-invasive technique to measure accurate temperature between grains in the microwave field.
5) Solve heat transfer and thermal stresses solutions which result from sample geometry and from the type of thermal history.
6) Use an isostatic press to fabricate all ceramic samples that are to be either conventionally processed or microwave processed.

LIST OF REFERENCES

LIST OF REFERENCES

1. A. R. Von Hipple, Dielectric Materials and Applications, Technology Press of MIT and Wiley, New York, (1954).

2. G. E. Feiker and N. C. Gittinger, "Rapid Heating of Dielectric Materials at 915 Mc," Electrical Engineering, Vol. 78, No. 11, p. 1089, (1959).

3. J. D. Ford, "High Temperature Chemical Processing via Microwave Absorption," J. Microwave power, Vol. 2-2, p. 61-64, (1967).

4. D. K. Wong, "Microwave Dielectric Constants of Metal Oxides at High Temperatures," M. S. Thesis, Department of Electrical Engineering, The Univ. of Alberta, Edmonton, Canada, (1975).

5. E. A. Maguire and D. W. Readey, "Microwave-Absorbing Ferrite Composites," J. Am. Ceram. Soc., Vol. 59, No. 9-10, p. 434-37, (1976).

6. M. K. Krage, "Microwave Sintering of Ferrites," Ceramic Bulletin, Vol. 60, No. 11, p. 1232-34, (1981).

7. W. R. Tinga and S. O. Nelson, "Dielectric Properties of Materials for Microwave Processing-Tabulated," J. Micrawave Power, Vol. 8, No. 1, p. 23-66, (1973).

8. W. R. Tinga and E. M. Edwards, "Dielectric Measurement Using Swept Frequency Techniques," J. Microwave Power, Vol. 3, No. 3, p. 144-75, (1968).

9. W. R. Tinga and W. A. G. Voss, Microwave Power Engineering, p. 189-94, Vol. 2, Academic Press, New York, (1968).

10. W. R. Tinga, "Interaction of Microwaves with Materials," p. 19-29, in Proc. of IMPI, Short Course for Users of Microwave Power, (1970).

11. A. J. Berteaud and J. C. Badot, "High Temperature Microwave Heating in Refractory Materials," J. Microwave Power, Vol. 11, No. 4, p. 315-20, (1976).

12. N. W. Schubring, "Microwave Sintering of Alumina Spark Plug Insulators," Tech. Rept. GMR-4471, General Motors Research Laboratory, p. 1-27, (1983).

13. P. A. Hass, "Heating of Uranium Oxides in a Microwave Oven," J. Am. Ceram. Soc., Vol. 58, No. 9, p. 873, (1979).

14. R. Roy, S. Komarneni, and L. J. Yang, "Controlled Microwave Heating and Melting of Gels," J. Am. Ceram. Soc., Vol. 68, No. 7, p. 392-95, (1985).

15. S. Komarneni and R. Roy, "Anomalous Microwave Melting of Zeolites," J. Mat. Sci. Lett., Vol. 4, No. 2, p. 107-10, (1986).

16. C. E. Holcombe, "New Microwave Coupler Material," Ceramic Bulletin, Vol. 62, No. 12, p. 1388, (1983).

17. C. E. Holcombe, "Microwave Coupler and Method," United States Patent, No. 455942, (1985).

18. T. T. Meek, R. D. Blake, and T. G. Gregory, "Low Density Foams Fabricated Using Microwaves," Ceram. Eng. Sci. Proc., Vol. 6, p. 1161-70, (1985).

19. T. T. Meek and R. D. Blake, "Ceramic-Ceramic Seals by Microwave Heating," J. Mat. Sci. Lett., Vol. 5, No. 3, p. 270-74, (1986).

20. T. T. Meek, M. H. Brooks, R. D. Blake, J. J. Petrovic, H. Jory, and J. V. Milewski, "Microwave Processing of Ceramics," J. Microwave Power, Vol. 21, No. 3, p. 193-94, (1986).

21. T. T. Meek, F. H. Cocks, D. T. Vaniman, and R. A. Wright, "Microwave Processing of Lunar Materials," in Potential Applications, Lunar Bases and Space Activities of the 21st Century, Edited by W. Mendell, Lunar Planetary Institute, Publication Office, Huston, Texas, (1986).

22. T. T. Meek, "Proposed Model for the Sintering of a Dielectric in a Microwave Field," J. Mat. Sci. Letters, Vol. 6, p. 638-40, (1987).

23. T. T. Meek, C. E. Holcombe, and N. Dykes, "Microwave Sintering of Some Oxide Materials Using Sintering Aids," J. Mat. Sci. Lett., Vol. 6, No. 9, p.1060-62, (1987).

24. T. T. Meek, R. D. Blake, and J. J. Petrovic, "Microwave Sintering of Al_2O_3 and Al_2O_3-SiC Whisker Composites," Ceram. Eng. Sci. Proc., Vol. 8, No. 7-8, p. 861-71, (1987).

25. T. T. Meek, D. T. Vaniman, R. D. Blake, and M. J. Godbole, "Sintering of Lunar Soil Simulants Using 2.45 GHz Microwave Radiation," p. 23-27 in Proceedings of the 18th Lunar and Planetary Science Conference, Huston, Texas, (1987).

26. T. T. Meek, R. D. Blake, J. D. Katz, J. R. Bradberry, and M. H. Brooks, "Cation Diffusion in Glass Heated Using 2.45 GHz Radiation," J. Mat. Sci. Lett., Vol. 7, No. 1, p. 28-31, (1988).

27. R. D. Blake and T. T. Meek, "Microwave Processed Composite Materials," J. Mat. Sci. Lett., Vol. 5, No. 11, p. 1097-98, (1986).

28. Record of Invention, "Seletive Sintering of Ceramics Using Microwave Energy," T. T. Meek, M. Brooks, and J. V. Milewski, DOE Case Number S 58942, Date Submitted 5 Oct., (1982).

29. H. D. Kimrey, T. L. White, T. S. Bigelow, and P. F. Becher, "Initial Results of a High Power Microwave Sintering Experiment at ORNL," J. Microwave Power, Vol. 21, No. 3, p. 81-82, (1986).

30. H. D. Kimrey and M. A. Janney, "Design Principles for High Frequency Microwave Cavities"; p. 367-72 in Microwave Processing of Materials, Vol. 124, Edited by W. H. Sutton, M. H. Brooks, and I. J. Chabinsky, Materials Research Society, Pittsburgh, PA, (1988).

31. B. Swain, "Microwave Sintering of Ceramics," Advanced Materials and Process, Vol. 134, No. 3, p. 76-82, (1988).

32. M. A. Janney and M. D. Kimrey, "Microwave Sintering of Alumina at 28 GHz" p. 914-24 in Cramic Transactions, Ceramic Powder Science, II, B, Edited by G. L. Messing, E. R. Fuller, Jr., and H. Hausner, American Ceramic Society, Westerville, OH, (1988).

33. M. A. Janney and H. D. Kimrey, "Microstructure Evolution in Microwave Sintered Alumina"; to be published in Advance -ments in Sintering, American Ceramic Society, OH, (1988).

34. J. D. Katz, R. D. Blake, and J. J. Petrovic, "Microwave Sintering of Alumina-Silicon Carbide Composites at 2.45 and 60 GHz," Ceram. Eng. Sci. Proc., Vol. 9, No. 7-8, p. 725-34, (1988).

35. J. D. Katz, R. D. Blake, J. J. Petrovic and H. Scheinberg, "Microwave Sintering of Boron Carbide"; p. 219-26 in Microwave Processing of Materials, Vol. 124, Edited by W. H. Sutton, M. H. Brooks, and I. J. Chabinsky, Materials Research Society, Pittsburgh, PA, (1988).

36. Y. L. Tian, M. E. Brodwin, and D. L. Johnson, "Microwave Sintering of Ceramics Under High Gas Pressure"; p. 213-18 in Microwave Processing of Materials, Vol. 124, Edited by W. H. Sutton, M. H. Brooks, and I. J. Chabinsky, Materials Research Society, Pittsburgh, PA, (1988).

37. Y. L. Tian and D. L. Johnson, "ultrafine Microstructure of Al_2O_3 Produced by Microwave Sintering"; p. 925-32 , in Cramic Transactions, Ceramic Powder Science, II, B, Edited by G. L. Messing, E. R. Fuller, Jr., and H. Hausner, American Ceramic Society, Westerville, OH, (1988).

38. W. H. Sutton, "Microwave Firing of High Alumina Ceramics"; p. 287-95, in Microwave Processing of Materials, Vol. 124, Edited by W. H. Sutton, M. H. Brooks, and I. J. Chabinsky, Materials Research Society, Pittsburgh, PA, (1988).

39. I. Ahmad, G. J. Chandler, and D. E. Clark, "Processing of Superconducting Ceramics Using Microwave Energy"; p. 239-46, in Microwave Processing of Materials, Vol. 124, Edited by W. H. Sutton, M. H. Brooks, and I. J. Chabinsky, Materials Research Society, Pittsburgh, PA, (1988).

40. W.B. Harrison, M. R. B. Hanson, and B. G. Koepke, "Microwave Processing and Sintering of PZT and PLZT Ceramics"; p. 279-86, in Microwave Processing of Materials, Vol. 124, Edited by W. H. Sutton, M. H. Brooks, and I. J. Chabinsky, Materials Research Society, Pittsburgh, PA, (1988).

41. D. Palaith, R. Silberglitt, C. C. M. Wu, R. Kleiner, and E. L. Libelo, "Microwave Joining of Ceramics"; p. 255-66, in Microwave Processing of Materials, Vol. 124, Edited by W. H. Sutton, M. H. Brooks, and I. J. Chabinsky, Materials Research Society, Pittsburgh, PA, (1988).

42. H. Fukushima, T. Yamanka, and M. Matsui, "Microwave Heating of Ceramics and Its Application to Joining"; p. 267-72, in Microwave Processing of Materials, Vol. 124, Edited by W. H. Sutton, M. H. Brooks, and I. J. Chabinsky, Materials Research Society, Pittsburgh, PA, (1988).

43. W. R. Tinga, "Fundamentals of Microwave-Material Interactions and Sintering"; p.33-44, in Microwave Processing of Materials, Vol. 124, Edited by W. H. Sutton, M. H. Brooks, and I. J. Chabinsky, Materials Research Society, Pittsburgh, PA, (1988).

44. V. K. Varadar, Y. Ma, A. Lakhtakia, and V. V. Varadan, "Microwave Sintering of Ceramics"; p. 45-57, in Microwave Processing of Materials, Vol. 124, Edited by W. H. Sutton, M. H. Brooks, and I. J. Chabinsky, Materials Research Society, Pittsburgh, PA, (1988).

45. M. P. Harmer, E. W. Roberts, and R. J. Brook, "Rapid Sintering of Pure and Doped α-Al_2O_3," Trans. J. Brit. Ceram. Soc., Vol. 78, No. 1, p. 22-25, (1979).

46. M. P. Harmer and R. J. Brook, "Fast Firing-Microstructural Benefits," Trans. J. Brit. Ceram. Soc., Vol. 80, p. 147-48, (1981).

47. H. Mostaghaci and R. J. Brook, "Production of Dense and Fine Grain Size $BaTiO_3$ by Fast Firing," Trans. J. Brit. Ceram. Soc., Vol. 82, No. 5, p. 167-69, (1983).

48. S. Das and T. R. Curlee, "Microwave Sintering of Ceramics: Can We Save Energy?," Ceramic Bulletin, Vol. 66, No. 7, p. 1093-94, (1987).

49. I. J. Chabinsky and E. E. Eves III, "The Application of Microwave Energy in Drying, Calcining, and Firing of Ceramics," Inter Ceram, Vol. 6 (Dec.), p. 30-35, (1986).

50. L. M. Sheppard, "Manufacturing Ceramics with Microwaves: The Potential for Economical Production," Ceramic Bulletin, Vol. 67, No. 10, p. 1656-61, (1988).

51. W. W. Ho, "High Temperature Dielectric Properties of Polycrystalline Ceramics"; p. 137-48 in Microwave Processing of Materials, Vol. 124, Edited by W. H. Sutton, M. H. Brooks, and I. J. Chabinsky, Materials Research Society, Pittsburgh, PA, (1988).

52. D. Couderc, M. Giroux, and R. G. Bosisio, "Dynamic High Temperature Microwave Complex Permittivity Measurements on Samples Heated Via Microwave Absorption," J. Microwave Power, Vol. 8, No. 1, (1973).

53. W. B. Westphal and A. Sils, Dielectric Constant and Loss Data, Technical AFML-TR-72-39, Air Force Materials Laboratory, Wright-Patterson AFB, April, (1972).

54. W. H. Sutton, "Microwave Processing of Ceramic Materials," Ceramic Bulletin, Vol. 68, No. 2, p. 376-86, (1989).

55. W. D. Kingery, H. K. Bowen, and D. R. Uhlmann, Introduction to Ceramics, 2nd ed., John Wiley and Sons, Inc., (1976).

56. K. D. Humphrey, "Microwave Sintering of $BiTiO_3$ Ceramics," M. S. Thesis, Department of Ceramic Engineering, Univ. of Missouri-Rolla, (1980).

57. W. H. Hayt Jr., Engineering Electromagnetics, p. 123-28, McGraw-Hill Book Co., Inc., New York, (1958).

58. M. N. Ozisik, Heat Conduction, p. 1-24, John Wiley and Sons, New York, (1980).

59. J. C. Araneta, "High Temperature Microwave Heating and Characterization of Dielectric Rods," Ph. D. Dissertation, Department of Electrical Engineering, Northwestern University, (1984).

60. F. Kreith and J. F. Kreidf, Principles of Solar Engineering, Hemisphere Pub. Corp., Washington, (1978).

61. R. Siegal and J. R. Howell, Thermal Radiation Heat Transfer, p. 374-401, 2nd ed., Hemisphere Pub. Corp., Washington, (1981).

62. S. Timoshenko, Theory of Elasticity, p. 415, 3rd ed., McGraw Hill Book Co., Inc., New York, (1970).

63. D. P. H. Hasselman, "Unified Theory of Thermal Shock Fracture Initiation and Crack Propagation in Brittle Ceramics," J. Am. Ceram. Soc., Vol. 52, No. 11, p. 600-04, (1969).

64. J. H. Ainsworth and R. E. Moore, "Fracture Behavior of Thermally Shocked Alumium Oxide," J. Am. Ceram. Soc., Vol. 52, No. 11, p. 628-29, (1969).

65. T. K. Gupta, "Strength Degradation and Crack Propagation in Thermally Shocked Al_2O_3," J. Am. Ceram. Soc., Vol. 55, No. 5, p. 249-53, (1972).

66. T. K. Gupta, "Resistance to Crack Propagation in Cramics Subjected to Thermal Shock," J. Mat. Sci., Vol. 8, No. 9, p. 1283-86, (1973).

67. J. A. Coppola, "Investigation of the Fracture Surface Energy, Fracture Strength and Thermal Shock Behavior of Polycrystalline Materials," M. S. Thesis, Department of Ceramic Science, Pennsylvania State Univ., (1971).

68. P. F. Becher, "Transient Thermal Stress Behavior in ZrO_2 Toughened Al_2O_3," J. Am. Ceram. Soc., Vol. 64, No. 1, p. 37-39, (1981).

69. J. Nakayama, "Thermal Shock Resistance of Ceramic Materials," p. 759-78, in Fracture Mechanics of Ceramics Vol. 2,

Edited by R. C. Bradt, D. P. H. Hasselman, and F. F. Lange, Plenum Press, New York, (1973).

70. T. N. Tiegs and P.F. Becher, "Thermal Shock Behavior of an Alumina-SiC Whisker Composites," J. Am. Ceram. Soc., Vol. 70, No. 5, p. c-109-c-111, (1987).

71. B. A. Boley and J. Weiner, Theory of Thermal Stresses, John Wiley and Sons, Inc., New York, (1960).

72. D. P. H. Hasselman, "Thermal Stress Resistance Parameters For Brittle Refractory Ceramics: A Compendium," J. Am. Ceram. Soc., Vol. 49, No. 12, p. 1033-37, (1970).

73. N. Claussen and D. P. H. Hasselman, "Improvement of Thermal Shock Resistance of Brittle Structure Ceramics by a Dispersed Phase of ZrO_2," p. 51-86, in Thermal Stresses in Severe Environments, Edited by D. P. H. Hasselman and R. A. Heller, Plenum Press, New York., (1980).

74. N. Claussen, "Fracture Toughness of Al_2O_3 with an Unstabilized ZrO_2 Dispersed Phase," J. Am. Ceram. Soc., Vol. 59, No. 1-2, p. 49-51, (1976).

75. N. Claussen and J. Jahn, "Mechanical Properties of Sintered and Hot Pressed Si_3N_4-ZrO_2 Composites," J. Am. Ceram. Soc., Vol. 61, No. 1-2, p. 94-95, (1978).

76. C. E. Curtis, "Development of Zirconia Resistance to Thermal Shock," J. Am. Ceram. Soc., Vol. 30, No. 6, p. 180-96, (1947).

77. J. D. McCullough and K. N. Trueblood, "The Crystal Structure of Baddeleyite (Monoclinic ZrO_2)," Acta Cryst., Vol. 12, p. 507-11, (1959).

78. G. Teufer, "The Crystal Structure of Tetragonal ZrO_2," Acta Cryst., Vol. 15, p. 1187, (1962).

79. R. N. Patial and E. C. Subbarao, "Axial Thermal Expansion of ZrO_2 and HfO_2 in the Range Room Temperature to 1400 °C", J. Appl. Cryst., Vol. 2, p. 281, (1969).

80. G. M. Wolten, "Diffusionless Phase Transformations in Zirconia and Halfonia," J. Am. Ceram. Soc., Vol. 46, No. 9, p. 418-22, (1963).

81. A. H. Heuer, N. Claussen, W. M. Kriven, and M. Ruhle, "Stability of Tetragonal ZrO_2 Particles in Ceramic Matrics," J. Am. Ceram. Soc., Vol. 62, No. 12, p. 643-50, (1982).

82. N. Claussen, J. Steeb, and R. F. Pabst, "Effect of Induced Microcracking on the Fracture Toughness of Ceramics," Ceramic Bulletin, Vol. 56, No. 6, p. 559-62, (1977).

83. D. J. Green, "Critical Microstructures for Microcracking in Al_2O_3-ZrO_2 Composites," J. Am. Ceram. Soc., Vol. 65, No. 12, p. 610-14, (1982).

84. D. L. Porter, A. G. Evans, and A. H. Heuer, "Transformation-Toughening in Partially-Stabilized Zirconia (PSZ)," Acta Met., Vol 27, p. 1649, (1979).

85. R. Stevens and P. A. Evans, "Transformation Toughening by Dispersed Polycrystalline Zirconia," Trans. J. Brit. Ceram. Soc., Vol. 83, No. 1, p. 28-31, (1984).

86. A. G. Evans and A. H. Heuer, "Transformation Toughening in Ceramics: Martensitic Transformation in Crack-Tip Stress Fields," J. Am. Ceram. Soc., Vol. 63, No. 5-6, p. 241-48, (1980).

87. R. M. McMeeking and A. G. Evans, "Mechanics of Trasformation -Toughening in Brittle Materials," J. Am. Ceram. Soc., Vol. 65, No. 5, p. 242-46, (1982).

88. N. Claussen and R. Wagner, "Influence of Surface Condition on Strength of Al_2O_3 Containing Tetragonal ZrO_2," Ceramic Bulletin, Vol. 58, No. 9, p. 883, (1978).

89. F. F. Lange, "Transformation Toughening: Part 1, Size Effects Associated with the Thermodynamics of Constrained Transformations," J. Mat. Sci., Vol. 17, No. 1, p. 225-34, (1982).

90. D. J. Green, F. F. Lange, and M. R. James, "Residual Surface Stresses in Al_2O_3-ZrO_2 Composites," p. 240-50, in Advances in Ceramics, Vol 12, Edited by N. Claussen, American Ceramic Society, Columbus, OH.

91. T. K. Gupta, "Strengthening by Surface Damage in Metastable Tetragonal Zirconia," J. Am. Ceram. Soc., Vol. 63, No. 1-2, p. 117, (1980).

92. F. F. Lange, "Transformation Toughening: Part 2, Contribution to Fracture Toughness," J. Mat. Sci., Vol. 17, p. 235-39, (1982).

93. N. Claussen, "Transformation-Toughened Ceramics (TTC)," p. 51-86, in Ceramics in Advanced Energy Technologies, Edited by H. Krockel, M. Merz, and O. Van der Biest, D. Reidel Pub. Co., (1982).

94. T. K. Gupta, F. F. Lange, and J. H. Bechtold, "Effect of Stress-Induced Phase Transformation on the Properties of Polycrystalline Zirconia Containing Metastable Tetragonal Phase," J. Mat. Sci., Vol. 13, No. 7, p. 1464-70, (1978).

95. T. K. Gupta, J. H. Bechtold, R. C. Kuznichi, L. H. Cadoff, and B. R. Rossing, "Stabilization of Tetragonal Phase in Polycrystalline Zirconia," J. Mat. Sci., Vol. 12, No. 12, p. 2421-26, (1977).

96. H. Abe, "Mechanical Properties of Engineering Ceramics," Ceramic Bulletin, Vol. 64, No. 12, p. 1594-96, (1985).

97. E. P. Butler and J. Drennan, "Microstructural Analysis of Sintered High-Conductivity Zirconia with Al_2O_3 Additions," J. Am. Ceram. Soc., Vol. 65, No. 10, p. 474-78, (1982).

98. S. Rajendran, J. Drennan, and S. P. S. Badwal, "Effect of Alumina Additions on the Grain Boundary and Volume Resistivity of Tetragonal Zirconia Polycrystals," J. Mat. Sci. Lett., Vol. 6, No. 12, p. 1431-34, (1987).

99. T. Kosmac, "The Role of Tetragonal and Monoclinic ZrO_2 Particles in the Fracture Toughness of Al_2O_3-ZrO_2 Composites," Mat. Sci. and Eng., Vol. 71, No. 5, p. 57-64, (1985).

100. R. Majumdar, E. Gilbart, and R. J. Brook, "Kinetics of Densification of Alumina-Zirconia," Trans. J. Brit. Ceram. Soc., Vol. 85, No. 5, p. 156-60, (1986).

101. P. F. Becher, C. Cm. Wu, and B. A. MacFarlane, "Thermal Shock Behavior in Toughened Al_2O_3-ZrO_2 Composites," Ceramic Bulletin, Vol. 59, No. 3, p. 357, (1980).

102. F. F. Lange, "Processing-Related Fracture Origines: I, Observations in Sintered and Isostatically Hot-Pressed Al_2O_3/ZrO_2 Composites," J. Am. Ceram. Soc., Vol. 66, No. 6, p. 396-98, (1983).

103. T. Sato and M. Shimada, "Control of the Tetragonal-To-Monoclinic Phase Transformation of Yittria Partially Stabilized Zirconia in Hot Water," J. Mat. Sci., Vol. 20. No. 11, p. 3988-92, (1985).

104. M. I. Osendi and J. S. Moya, "Role of Titania on the Sintering Microstructure and Fracture Toughness of Al_2O_3/ZrO_2 Composites," J. Mat. Sci. Lett., Vol. 7, No. 1, p. 15-18, (1988).

105. K. Tsukuma, K. Ueda, K. Matsushita, and M. Shimada, "High Temperature Strength and Fracture Toughness of Y_2O_3-Partially Stabilized Al_2O_3/ZrO_2 Composites," J. Am. Ceram. Soc., Vol. 68, No. 2, p. c-56-c-58, (1985).

106. S. Rajendran, M. V. Swain, and H. J. Rossell, "Mechanical Properties and Microstructures of Co-Precipitation Derived Tetragonal Y_2O_3-ZrO_2-Al_2O_3 Composites," J. Mat. Sci., Vol. 23, No. 5, p. 1805-12, (1988).

107. F. Wakai, H. Kato, S. Sakaguchi, and N. Murayama, "Compressive Deformation of Y_2O_3-Stabilized ZrO_2/Al_2O_3 Composite," Yogyo-Kyokai-Shi, Vol. 94, No. 9, p. 1017-20, (1986).

108. M. Fukuhara, "Properties of (Y) Y_2O_3-ZrO_2-(Ti or Si)C Composites," J. Am. Ceram. Soc., Vol. 72, No. 2, p. 236-42, (1989).

109. ASTM C 693-84, "Standard Test Method for Density of Glass by Buoyancy," p. 287-89, (1984).

110. P. E. Becher, "Effect of Water Bath Temperature on the Thermal Shock of Al_2O_3," J. Am. Ceram. Soc., Vol. 64, No. 3, p. c-17-c-18, (1981).

111. R. F. M. Thornley and L. Cartz, "Direct Examination of Ceramic Surfaces with the Scanning Electron Microscope," J. Am. Ceram. Soc., Vol. 45, No. 9, p. 425-28, (1962).

112. M. I. Mendeson, "Average Grain Size in Polycrystalline Ceramics," J. Am. Ceram. Soc., Vol. 52, No. 8, p. 443-46, (1969).

113. R. C. Garvie, R. H. J. Hannick, and M. V. Swain, "X-ray Analysis of the Transformed Zone in Partially Stabilized Zirconia (PSZ)," J. Mat. Sci. Lett., Vol. 1, No. 10, p. 437-40, (1982).

114. S. L. McGill, J. W. Walkiewacz, and G. A. Smyres, "The Effects of Power Level on the Microwave Heating of Selected Chemicals and Minerals"; p. 247-52 in Microwave Processing of Materials, Vol. 124, Edited by W. H. Sutton, M. H. Brooks, and I. J. Chabinsky, Materials Research Society, Pittsburgh, PA, (1988).

115. G. Roussy, A. Mercier, and J. P. Vaubourg, "Temperature Runaway of Microwave Heated Materials: Study and Control," J. Microwave Power, Vol 20, No. 1, p. 47-51, (1985).

116. D. Bhattacharyya and D. C. T. Pei, "Application of Microwave Power in Heat Transfer Studies," J. Microwave Power, Vol. 8, No. 3-4, p. 287-94, (1973).

117. C. C. Johnson and A. W. Guy, "Non-ionizing Electromagnetic Wave Effects in Biological Materials and Systems," Proc. of the IEEE, Vol. 60, No. 6, p. 692, (1972).

118. T. T. Meek, S. S. Park, M. A. Neils, and C. W. Kim, "Temperature Measurement for Microwave Processing of Advanced Ceramics, " to be published in Microwave Processing of Materials, Vol. 125, Materials Research Society, Pittsburgh, PA, (1989).

119. J. Wilson and S. M. Kunz, "Microwave Sintering of Partially Stabilized Zirconia," J. Am. Ceram. Soc., Vol. 71, No. 1, p. c-40-c-41, (1988).

120. C. E. Holcombe, T. T. Meek, and N. L. Dykes, "Enhanced Thermal Shock Properties of Y_2O_3-2wt% ZrO_2 Heated Using 2.45 GHz Radiation"; p. 227-34 in Microwave Processing of Materials, Vol. 124, Edited by W. H. Sutton, M. H. Brooks, and I. J. Chabinsky, Materials Research Society, Pittsburgh, PA, (1988).

121. F. F. Lange, "Transformation Toughening; part 3. Experimental Observations in the ZrO_2-Y_2O_3 System," J. Mat. Sci., Vol. 17, No.1, p. 240-46, (1982).

VITA

Seong-Soo Park was born in Pusan, Korea on January 21, 1956. He attended high school in Pusan, Korea and graduated from Dong Rae High School in Feburary 1974. The following March he entered the Pusan National University in Pusan. He received a B. S. degree in Material Engineering in Feburary 1978. The following March he entered Chemical Engineering in the Graduate School of the Pusan National University. After graduating his Graduate School in Feburary 1980, he joined military service. He entered the Beik-San Paint Corporation in May 1982 after completion of two and a quarter years military service. He also worked at R&D department of the Kuk-Jae Corporation for three years. Study toward a M. S. in Materials Science and Engineering at the University of Tennessee began in the Fall of 1986. This degree was awarded in August 1989. He plans on continuing his education toward a Ph. D. at the University of Tennessee. His ultimate goal is a career in applied research and teaching.

He resides at 1611 Laurel Ave. 1115 with his wife, Bong-Eun Kim, and son, Min-Shik Park.

The auther is a student member of the American Society for Metals and Society for the Advancement of Material and Process Engineering.